Spectroscopy and control of ultrafast energy dynamics in natural light–harvesting complexes

by

Huzifa Mohammed Ahamed Mohammed Elnour

Submitted in partial fulfilment of the requirements for the degree

Doctor of Philosophy (PhD) in Physics

in the Department of Physics

in the Faculty of Natural and Agricultural Sciences

University of Pretoria

Pretoria

September 2018

Supervisor: Prof. Tjaart PJ Krüger

Co-Supervisor: Prof. Rienk van Grondelle

Declaration

I, Huzifa Mohammed Ahamed Mohammed Elnour declare that the thesis, which I hereby submit for the degree Philosophiae Doctor at the University of Pretoria, is my own work and has not previously been submitted by me for a degree at this or any other tertiary institution.

SIGNATURE:

DATE:

Spectroscopy and control of ultrafast energy dynamics in natural light–harvesting complexes

by

Huzifa Mohammed Ahamed Mohammed Elnour

Keywords: Energy dissipation, energy transfer, laser coherent control, light-harvesting complex, pulse shaping, quenching, transient absorption spectroscopy.

Abstract

Coherent control and transient absorption spectroscopy techniques have been used widely in biophysics to manipulate and study ultrafast molecular dynamics such as excitation energy transfer, internal conversion and photoprotection mechanisms. In this thesis, we investigate how excitation energy transfer pathways originating from the S_2 state of carotenoids in the light-harvesting complex of plants and green algae can be manipulated through coherent control; moreover, we investigate energy dissipation mechanisms in the nonameric fucoxanthin-chlorophyll-a,c-binding protein of the centric *diatom Cyclotella meneghiniana*, using the transient absorption spectroscopy technique.

By manipulating the temporal amplitude and phase of the excitation pulse (through the use of blind phase functions on a spatial light modulator) we were able to optimize the energy transfer channel over the internal conversion channel by a factor of 24% compared to the initial pulse. The optimized pulse exhibited a shape that consists of 7 sub-pulses with a separation time of 178 fs between every two consecutive sub-pulses, and a FWHM of 92 fs for each sub-pulse. We propose that the main mechanism responsible for the optimization is the enhancement of specific vibrational modes via impulsive stimulated Raman scattering in order to facilitate energy transfer.

In order to investigate the energy dissipation mechanisms in the nonameric fucoxanthin-chlorophyll-a,c-binding protein FCPb of the centric *diatom Cyclotella meneghiniana*, we performed transient absorption (pump-probe) spectroscopy on this complex. FCPb complexes in their unquenched state were compared with those in two types of quenching environments, namely aggregation induced quenching by detergent removal, and clustering via incorporation into liposomes. Through the application of global and target analysis, in combination with a fluorescence lifetime study and annihilation calculations, we were able to resolve two quenching channels for FCPb in both quenching environments. Both quenching channels involve chlorophyll-a pigments. The faster quenching channel operates on a timescale of tens of picoseconds and exhibits similar spectral signatures as the unquenched state. The slower quenching channel operates on a timescale of tens to hundreds of picoseconds, depending on the degree of quenching, and is characterized by enhanced population of low-energy states between 680

and 710 nm. These results indicate that FCPb is, in principle, able to function as a dissipater of excess energy and can do this *in vitro* even more efficiently than the homologous FCPa complex, which is the only complex involved in fast photoprotection in these organisms. This indicates that when a complex displays photoprotection-related spectral signatures *in vitro* it does not imply that the complex participates in photoprotection *in vivo*. We suggest that FCPa is favored over FCPb as the sole energy-regulating complex in diatoms because its composition can more easily establish the balance between light-harvesting and quenching required for efficient photoprotection.

Acknowledgements

It is my great pleasure to thank and acknowledge the following people and organizations for their contributions to this work:

- My academic advisors Prof. Tjaart Krüger (University of Pretoria) and Prof. Rienk van Grondelle (VU University Amsterdam) for their support and encouragement.
- Dr. Charusheela Ramanan and Dr. Nicoletta Liguori from VU University Amsterdam for their invaluable assistance during my visits to the Netherlands.
- Prof. Claudia Büchel and Dr. Lars Dietzel from Goethe University Frankfurt, and Dr. Erica Belgio from the Czech Academy of Sciences for their help with preparing my samples and invaluable assistance.
- Dr. Adriaan Jacobus Hendriks from CSIR-NLC for his invaluable assistance with coding at CSIR– NLC.
- Bart Sasbrink and Henny van Roon for their assistance at LaserLaB Amsterdam.
- Henk van Wyk and Bafana Moya for the technical assistance with the laser in the lab at CSIR-NLC.
- University of Pretoria, VU university, and The National Laser Center (NLC) of the Council of Scientific and Industrial Research (CSIR) for the use of their facilities and the support they offered during my study
- National Research Foundation (NRF), South Africa VU University Amsterdam Strategic Alliances (SAVUSA) and Biophysics Initiative of the South African Institute of Physics (SAIP) for financial support.
- My friends in the department of physics and special thanks to my colleagues in the Biophysics research group, especially Towan Nothling, Alexander Paradzah, Asmita Singh, Justin Arthur Harrison, Farooq Kyeyune, and Joshua Botha.
- My parents, brothers, sisters, nephews, nieces and family members, who supported me during my studies.

Dedication

I dedicate this thesis to my parents Zainab Abuzaid and Mohammed Elnour

Abbreviations

ATP	adenosine triphosphate
BBO	beta Barium Borate crystal
Cyt b_6f	cytochrome b_6f
Chl	chlorophyll
ESA	excited state absorption
ET	energy transfer
FCP	fucoxanthin-chlorophyll-a,c-binding protein
FROG	Frequency Resolved Optical Gating
FWHM	full-width at half maximum
GSB	ground state bleaching
IC	internal conversion
ICT	intramolecular charge transfer
ISC	inter-system crossing
LHCII	light harvesting complex II
NPQ	non-photochemical quenching
OD	optical density
PSI	photosystem I
PSII	photosystem II
RC	reaction centre
SE	stimulated emission

Contents

Chapter 1

Introduction

1.1 Photosynthesis

Photosynthesis is a complex biological process whereby plants, algae and other photosynthetic organisms use solar photons to produce organic compounds. The process is divided into two types: oxygenic photosynthesis in which water is required and oxygen is released, and anoxygenic photosynthesis where water is not required and no oxygen is produced. Green plants, algae and cyanobacteria perform oxygenic photosynthesis and the overall process can be described by the following chemical equation

$$6CO_2 + 12H_2O \xrightarrow{\text{light}} C_6H_{12}O_6 + 6O_2 + 6H_2O \tag{1.1}$$

where the terms on the left side of the equation represent the two reactants carbon dioxide (CO_2) and water (H_2O). The water on the reactants side is used as an electron donor for redox reactions involved in the primary light energy stabilization. In the presence of light energy, the products of this reaction are glucose ($C_6H_{12}O_6$), water (H_2O) and oxygen (O_2). This resultant oxygen originates from water and not from the carbon dioxide (CO_2). Photosynthesis has been divided into two phases: the light dependent reactions, occurring in the thylakoid membrane; and light independent reactions such as the Calvin cycle that occurs in the chloroplast stroma [1]. The light dependent reactions for the oxygenic photosynthesis are carried out by four different multi-protein complexes known as photosystem I (PSI), photosystem II (PSII), cytochrome b_6f (Cyt b_6f), and the adenosine triphosphate (ATP) synthase enzyme. In plants and green algae, all of these protein complexes are situated in the thylakoid membrane (the membrane that surrounds the thylakoid). The thylakoids in turn are found as stacked or elongated unstacked membranous sacks in an organelle called the chloroplast [2]. The shape of the chloroplast is similar to the shape of a convex lens and has a diameter of a few micrometers, with about ten chloroplasts inside each cell of the photosynthetic organisms [1,3]. Figure 1.1 shows the multi-

protein units inside the thylakoid membrane that are involved in oxygenic photosynthesis. The

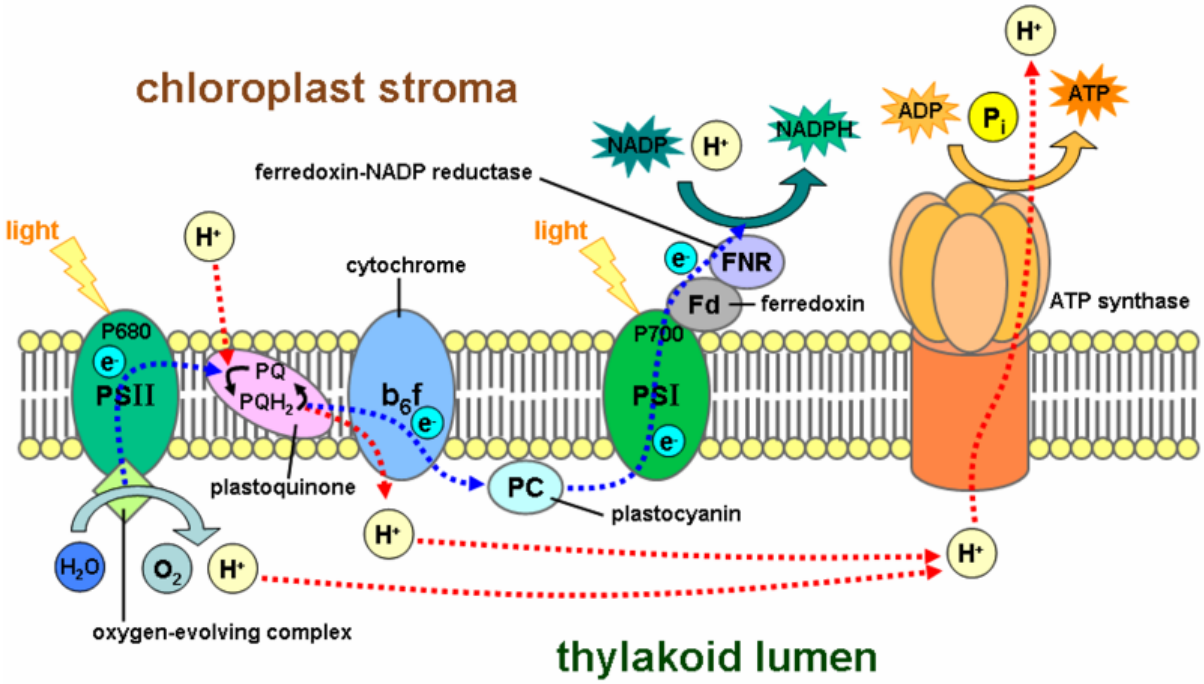

Figure 1.1: Schematic description of the multiprotein units inside the thylakoid membrane of oxygenic photosynthetic organisms, from left photosystem II (PSII), cytochrome b_6f (Cyt b_6f), photosystem I (PSI), and ATP synthases. ADP: adenosine diphosphate, ATP: adenosine triphosphate, NADP: nicotinamide adenine dinucleotide phosphate, NADPH: reduced nicotinamide adenine dinucleotide phosphate, and P_i: inorganic phosphate. Blue and red dashed lines represent the electron (e^-) and proton (H^+) pathways [4].

light dependent reactions are initiated by the absorption of light by a large number of pigments (light absorbing molecules) found in the light-harvesting complexes (LHCs) of PSI and PSII. Absorption of a photon promotes an electron to a higher energy orbital in the pigment. Due to coupling between the LHCs' pigments, the excitation is transferred with a high efficiency from the absorbing pigment to other pigments in the LHCs, and eventually to the reaction centre (RC) of PSII and PSI. As a result a special pair of chlorophylls known as P680 (because it absorbs light around 680 nm) bound to the PSII's RC protein and P700 (absorbs light around 700 nm) bound to the PSI's RC protein, are excited [5]. The excited P680 transfers an electron to adjacent pheophytin which in turn transfers an electron to the first plastoquinone (PQ) and then to a second PQ leading to charge-separation ($P680^+$ and PQ^-) across the thylakoid membrane. After the second PQ, the electron is passed through cytochrome b6f (Cyt b_6f), plastocyanin (PC), Photosystem I (PSI), PSI-bound ferredoxin (Fd), and finally to the ferredoxin-NADP reductase (FNR) at the stromal side of the thylakoid membrane, in order to be used for combining a hydrogen ion and nicotinamide adenine dinucleotide phosphate (NADP) to reduce the latter and form NADPH. During the photolysis process, water (on the reactant side of equation (1.1)) is split as: $2H_2O \rightarrow 4H^+ + 4e^- + O_2$. In this process, 4 photons are needed for splitting 1 water

molecule, and 8 photons to liberate one molecule of oxygen. The electron lost from the reaction center of PSII is replaced with the one that is produced from the photolysis process. The O_2 is released into the lumen and later into the atmosphere as a by-product of photosynthesis. The H^+ is released at the lumenal side of the thylakoid membrane, and later transported to the ATP synthase in order to be used for combining inorganic phosphate (P_i) and adenosine diphosphate (ADP) to produce the adenosine triphosphate (ATP) [5]. The excited P700 transfers an electron through Fd to FNR in order to be used again for the production of NADPH. The electron lost from PSI is replaced with the one that is transferred from PSII. Subsequently, the net products of these light-reactions are: O_2 released into the atmosphere, and formation of ATP chemical energy and NADPH electron donor [5]. In the Calvin Cycle, ATP and NADPH are used in a complex process to convert atmospheric carbon dioxide, CO_2, to glucose.

1.2 The light-harvesting complexes in photosynthesis

The light absorption process is the first step in photosynthesis. This process is performed by the light-harvesting pigment-protein complexes of photosynthetic organisms, also known as the antenna complexes. These complexes contain a number of pigment molecules, mainly chlorophyll and carotenoid, which are described in sections 1.2.1 and 1.2.2, respectively. These pigments are responsible for absorbing light, and funnelling the excitation energy with high efficiency to the pigments (special chlorophylls (P680)) in the RC of PSI and PSII [6, 7], on a timescale of a few hundreds of picoseconds (10^{-12}s) [8]. In the reaction center the absorbed excitation energy induces a charge-separation, which is then stabilized for few milliseconds in order to allow electron migration to Fd and FNR enzymes for the reduction of NADP to NADPH. Antenna pigments' type, organization, arrangement and concentration vary between different photosynthetic organisms and different types of LHCs of the same organism. In this study, the focus is on light-harvesting complex II (LHCII) in PSII of higher plants [6, 9–13], and the fucoxanthin-chlorophyll protein (FCPb), one of the two main LHCs of diatoms [14,15]. These complexes are described in sections 1.2.3 and 1.2.4, respectively.

1.2.1 Chlorophylls

Chlorophylls (Chls) are the primary pigments present in most of photosynthetic organisms. They are magnesium-containing chlorin compounds. Chlorophylls are responsible for several functions in the photosynthetic process, such as absorption of light, excitation energy transfer in the LHCs, and charge separation in the RC. There are several types of Chls found in the photosynthetic organisms, with small differences in their chemical structures. The most common type is chlorophyll-a (Chl-a), which is the most abundant type and is found in most

photosynthetic organisms; chlorophyll b (Chl-b) is found in plants and most types of algae as an accessory pigment; chlorophyll-c (Chl-c) is exclusively found in marine photosynthetic organisms such as diatoms and dinoflagellates [1, 16]. The Chl absorption spectrum has two major bands; one is located in the red or near infrared region and the other in the blue region, as depicted in Figure 1.2 for Chl-a and Chl-b.

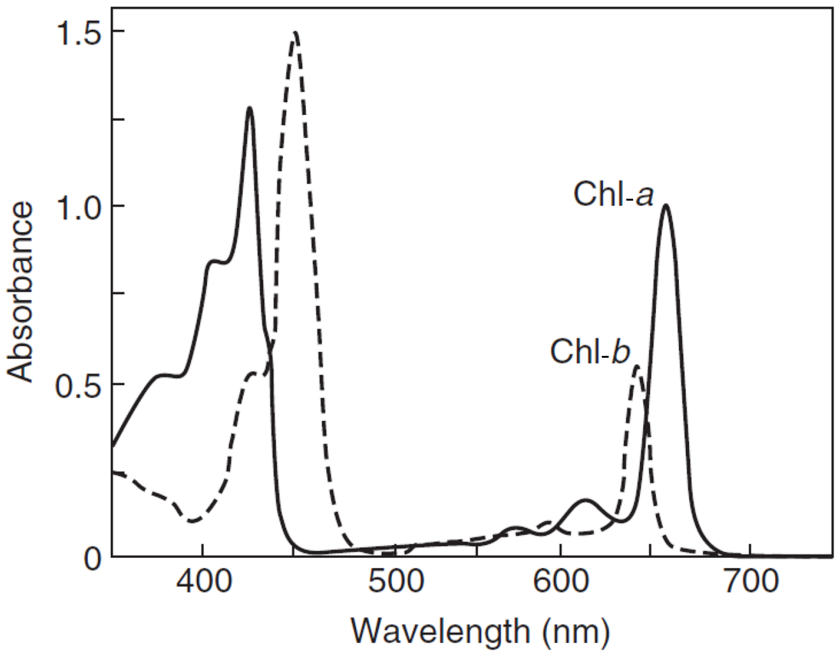

Figure 1.2: Absorption spectra of the Chl-a (solid line) and Chl-b (dashed line) in diethyl ether [17].

These two bands correspond to $\pi \longrightarrow \pi^*$ transitions of electrons in the conjugated π system of the chlorin macrocycle [1]. These spectra are usually described using the four-orbital model that was proposed by Martin Gouterman [18]. In this model the two major bands in the absorption spectrum of the Chl pigment are attributed to the transitions that occur between the two highest occupied molecular orbitals (HOMOs) and the two lowest unoccupied molecular orbitals (LUMOs), as illustrated by the simplified molecular orbital diagram of the chlorin macrocycle in Figure 1.3. The two higher-energy transitions are know as Soret bands which have a mixed polarization, whereas the two lowest-energy transitions are called the Q bands, which in turn consists of two bands due to the difference in orientations and strengths of the dipole moment of the different transitions. The longest-wavelength transition in this band is known as the Q_y band and is directly polarized along the y-axis of the molecule. The other band is called the Q_x band, and its polarization orientation has not been resolved. Theoretical calculations suggested that it is not polarized directly along the x-axis of the molecule [1].

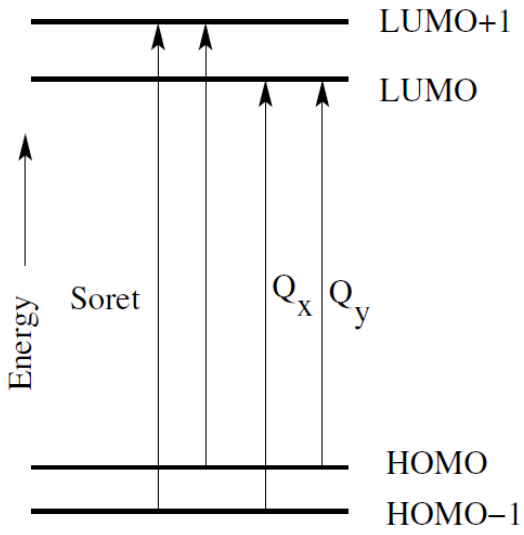

Figure 1.3: Illustration of a simplified molecular orbitals diagram of Chlorophylls. HOMO: highest occupied molecular orbital, and LUMO: lowest unoccupied molecular orbital. The two transitions with the highest energies are known as the Soret bands, while the two lowest transitions are known as the Q_y and Q_x bands. The electronic transition that is associated with the Q_y band is polarized directly along the y-axis of the molecule, whereas the Q_x transition is approximately polarized along the x-axis.

1.2.2 Carotenoids

Carotenoids are the second class of pigments that are found in virtually all LHCs of photosynthetic organisms [1, 19, 20]. They are responsible for the red, orange, and yellow colours of fruits, vegetables, flowers, and autumn leaves seen in nature [21]. Carotenoids involved in photosynthesis are made of two rings at the end of a polyene chain consisting of eight to thirteen π-conjugated C=C bonds. Figure 1.4 shows the molecular structure of the carotenoids lutein, violaxanthin, neoxanthin and zeaxanthin, which are present in the LHCs of higher plants and green algae, as well as fucoxanthin found in the LHCs of diatoms.

Carotenoids have several functions in the LHCs. Firstly, they absorb light in the green-blue spectral range and transfer the excitation energy to chlorophyll pigments. Secondly, they are strongly involved in *photoprotection* mechanisms. In the major photoprotection mechanism, carotenoids' ground state quenches the chlorophylls' triplet excited ^{3}Chl* states very quickly, before the ^{3}Chl* react with oxygen (O_2) to form oxygen singlet excited ($^1O_2{}^*$) states. These $^1O_2{}^*$ states are highly reactive and can cause severe damage to the photosynthetic apparatus. Thirdly, the triplet excited states of carotenoids are also capable to quench the oxygen singlet excited states directly and protect the photosynthetic apparatus [22, 23]. Furthermore, carotenoids play an important role in the regulation of thermal energy dissipation in the antenna systems under high light conditions, through the xanthophyll cycle. In this process, some specific carotenoids change their molecular structure and switch to other types of carotenoids [24, 25], such as the conversion of violaxanthin to zeaxanthin in LHCII, and diadinoxanthin to diatox-

anthin in FCP. The optical properties of carotenoids are determined mainly by the number of

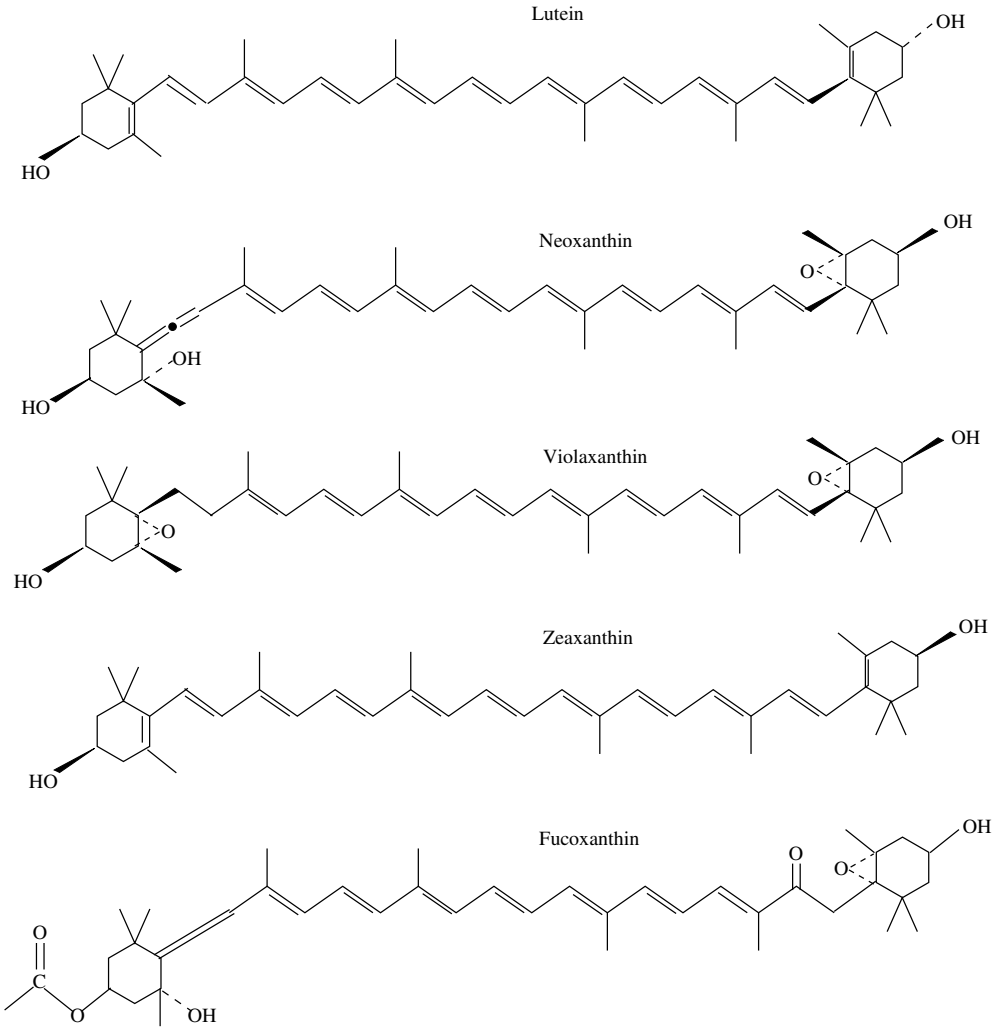

Figure 1.4: Molecular structures of lutein, neoxanthin, violaxanthin, zeaxanthin, and fucoxanthin carotenoids.

π-conjugate bonds on the polyene chain. The optical transition between the ground state S_0 and first electronic excited state S_1 is forbidden due to the inversion symmetry between these states [26, 27]. However, the second electronic excited state S_2 has a different inversion symmetry from S_0, and the optical transition from S_0 to S_2 is therefore allowed. The transition occurs in the 350-550 nm spectral range for carotenoids with eight to eleven π-conjugated C=C bonds. Figure 1.5 shows the absorption spectra of LHCII carotenoids. The lifetime of the S_2 state is usually very short (between 100 fs and 200 fs), and it therefore relaxes to the S_1 state via internal conversion (IC), which is a non-radiative relaxation process [28, 29]. The excited state S_1 then relaxes back to the ground state S_0 via IC [1, 28].

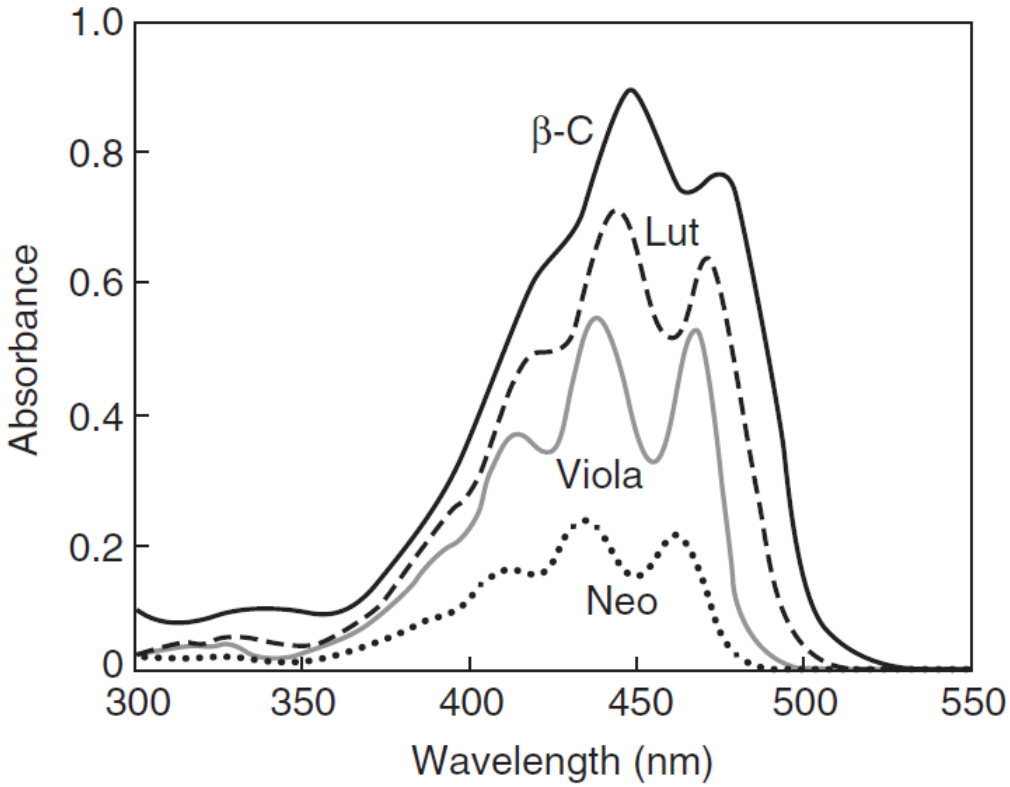

Figure 1.5: Absorption spectra of the LHCII carotenoids in diethyl ether [17]. Neo: neoxanthin, Viola: violaxanthin, Lut: lutein and β-C: β-carotene.

1.2.3 Light-harvesting complex II

Light harvesting is the initial process in photosynthesis, and is carried out by a collection of LHCs. The LHCII complex is the most abundant antenna complex in the chloroplast of higher plants and green algae [10, 11, 30]. The LHCII complex exists naturally in a trimeric form, consisting of three nearly identical monomers. Using X-ray diffraction the structure of LHCII extracted from spinach leaves was determined at 2.7 resolution [11]. Figure 1.6 (a) and (b) shows the membrane view of the crystal structure of an LHCII monomer and the top view of the LHCII monomer pigment organisation, respectively. As can be seen in Figure 1.6 (a) and (b), each monomer complex is composed of 8 Chl-a pigments, 6 Chl-b pigments and 4 carotenoids [6, 11–13, 29, 30]. Furthermore, LHCII plays an important role in the photoprotection mechanisms in order to prevent the photosynthetic apparatus from damage that can occur in the presence of light with a high intensity [6, 31]. In the presence of high illumination intensity, the violaxanthin carotenoid is converted into zeaxanthin, through the xanthophyll cycle, in order to regulate the energy dissipation during the protective mechanisms [24, 25]. Apart from this, LHCII is involved in regulating the distribution of excitation energy between PSII and PSI, through the lateral mobility of LHCII population from the PSII into the PSI in or-

der to increase the absorption cross-section of PSI and then provides excitation energy where it is required [31, 32]. The protein structure of the monomeric subunit of LHCII consists of three transmembrane helices and two short amphipathic helices (light blue colour in Figure 1.6 (a)) [13, 30]. These helices maintain the structure of the complex and bind almost all the pigments. In my research, an experimental technique was developed that can be used to control the excitation energy transfer dynamics in LHCII.

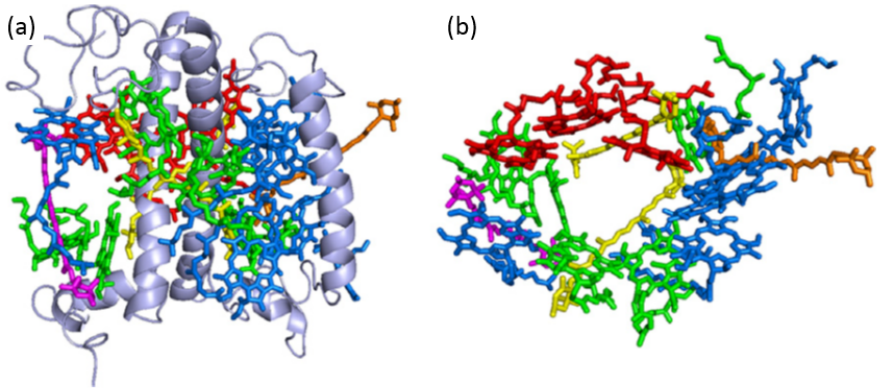

Figure 1.6: Membrane view of the protein crystal structure of the LHCII monomer (a) and top view of the pigments only (b). Blue: Chl-a; red: Chl-b; yellow: lutein; orange: neoxanthin; magenta: violaxanthin; and the light-blue structures are transmembrane and amphipathic helices [13].

1.2.4 Fucoxanthin-chlorophyll protein, the major light-harvesting complex of diatoms

Diatoms are unicellular marine organisms capable of oxygenic photosynthesis, and form a major group of algae that are characterised by their decorative silica shell [33]. They are the major players in the biochemical cycle of silicon, carbon, nitrogen, and phosphorus which have a significant effect on the global climate in ocean and fresh water environments [34]. Diatoms exist in two main groups known as pennate and centric diatoms. The pennate diatoms are needle-like in shape and have two plastids (chloroplasts) per cell, whereas the centric diatoms have a rotational symmetry and they contain more than two plastids per cell [33]. The membrane-intrinsic light-harvesting protein complexes of diatoms fall in the same family as LHCII of higher plants and green algae. However, there are differences in the membrane topology and pigment compositions [33, 35]. To date, the protein structure of the fucoxanthin-chlorophyll protein (FCP) complex is not available.

The main carotenoid in the diatom light-harvesting complex is fucoxanthin (Fx), which is present in high amounts, and is why the main antenna complexes of diatoms are named fucoxanthin-chlorophyll protein (FCP) [33]. Like LHCII, the FCP monomer binds 8 Chl-a.

The Fx:Chl-a stoichiometry is 1:1, so FCP binds a larger number of carotenoids than LHCII. Instead of Chl-b, however, FCP has two Chl-c pigments. Moreover, FCP complexes bind the xanthophyll cycle pigment diadinoxanthin (Ddx) and its de-epoxidated form diatoxanthin (Dtx) [33, 35, 36]. *In vivo* the conversion of Ddx into Dtx was shown to be correlated with the non-photochemical quenching process (Section 1.6) of Chl-a fluorescence in the presence of high illumination intensity [15, 37]. Fx contains a carbonyl group in conjugation with the polyene backbone, similar to the peridinin and siphonoxanthin carotenoids [38, 39]. This carbonyl group is responsible for the generation of the intramolecular charge transfer (ICT) state which couples to the first singlet excited state S_1, and forms a S_1/ICT mixed state where its lifetime depends on the solvent polarity [38,39]. The S_1/ICT state is highly efficient in transferring excitation energy to Chl-a [36] and may also by involved in the photoprotection mechanisms in the organism [40].

Two types of FCP complexes have been isolated from *Cyclotella meneghiniana*: FCPa and FCPb [15]. These complexes primarily differ in their polypeptide compositions and oligomeric states. FCPa is a trimeric complex resembling LHCII, and its trimers are formed by a mixture of the polypeptides Fcp1-3 from the Lhcf family and an Lhcx polypeptide in a smaller quantity [37]. In contrast, FCPb complexes are oligomers formed by nine monomers (nonamer) [41], that contain Fcp5, which is a different type of Lhcf polypeptide [14, 37]. Lhcf polypeptides are a group of proteins thought to be involved mainly in light-harvesting, whereas Lhcx proteins were proven to be involved in photoprotection [36, 37]. In this project, we investigated the energy dissipation mechanisms in the FCPb complex.

1.3 Excitation energy transfer

Excitation energy transfer among the photosynthetic LHCs' pigments is a very important process in photosynthesis. This transfer is facilitated through Coulombic interaction between the partaking molecules [42, 43]. The efficiency of the transfer depends on a number of factors, such as the distance between the donor and acceptor pigments, and the relative orientation of the emission transition dipole moment of the donor pigment and the absorption transition dipole moment of the acceptor pigment [44].

Theoretically, several methods were developed to describe dynamics of excitation energy transfer between pigments in photosynthetic antenna systems. However, choosing an appropriate method for any particular antenna system depends on the relative strength of pigment-pigment V and pigment-environment U interactions. If the ratio $V/U >> 1$ it results in a strong interaction, then excitation energy become delocalized over several pigments and its relaxation is treated as a coherent process. The most common method that has been used to investigate the relaxation dynamics for this case is the Redfield theory [45–47].

In the opposite case, when the ratio V/U $<<$ 1, interaction is classified as a very weak, and it is described by the Förster theory. In this case, the excitation energy is assumed to be localized on either the donor or the acceptor pigment and the transfer process is treated as an incoherent hopping process [8, 45, 47], whose rate is given as follows:

$$k_{DA} = \frac{1}{\tau_f^D}\left(\frac{R_0}{R_{DA}}\right)^6 \tag{1.2}$$

where τ_f^D is the natural lifetime of the excited state of the donor molecule in the absence of the acceptor. R_{DA} is the distance between the centres of the donor and acceptor. R_0 is the Förster critical distance at which the efficiency of the energy transfer is 50% and is given as

$$R_0^6 = 8.785 \cdot 10^{17} \kappa^2 n^{-4} \int F_D(\nu)\varepsilon_A(\nu)\nu^{-4} d\nu \tag{1.3}$$

$\kappa = \cos\alpha - 3\cos\beta_D\cos\beta_A$ is the orientation factor, α is the angle between the two dipoles, and β_D and β_A are the angles between donor and acceptor dipoles and the vector connecting them, respectively. n is the refractive index of the medium between the donor and acceptor. ε_A is the molar absorption coefficient of the acceptor and F_D is the normalised fluorescence spectrum of the donor [1, 42, 44]. Equations (1.2) and (1.3) show that the energy transfer rate is inversely proportional to the sixth power of the distance R_{DA} between the centres of the donor and acceptor. It is also proportional to κ^2, and the overlap integral of the donor emission spectrum and absorption spectrum of the acceptor via R_0.

1.4 Exciton concept

The exciton concept is a quantum model that is used to describe the excitation energy dynamics (relaxation) of strongly coupled molecules such as the pigments of photosynthetic systems. The idea is that when a sample containing strongly coupled molecules is excited, the excited state dynamics cannot be explained by the excitation of a single molecule, because the excitation energy is spread among several molecules (delocalized). In this case, the excitation energy relaxation is assumed to be a coherent process due to the strong interaction between molecules of the system.

If we consider the simplest example of just two isolated molecules. The dynamics of the system can be described through the solutions of the molecular time-independent Schrödinger wave equations [48]:

$$\begin{cases} H_1 \psi_1^i = \varepsilon_1^i \psi_1^i, \\ H_2 \psi_2^i = \varepsilon_2^i \psi_2^i, \end{cases} \tag{1.4}$$

where H_1 and H_2 are the Hamiltonians of the two molecules, ψ_1^i and ψ_2^i are the eigenfunctions of the two molecules, and ε_1^i and ε_2^i are the total energies of the two molecules. The superscript i = 0 refers to the ground state and i = 1 to the excited state. However, when these molecules are strongly coupled, then their excited state dynamics is described by the solution of the following Schrödinger equation:

$$(H_1 + H_2 + V_{12})\Psi^f = E^f \Psi^f, \tag{1.5}$$

where E^f is the total final energy of the system, H_1 and H_2 are the Hamiltonians of the two molecules, and Ψ^f is the eigenfunction of the final state. V_{12} represents the Coulombic interaction potential energy between the two molecules. Equation 1.5 shows that, the total Hamiltonian of the system includes H_1, H_2, and V_{12}. In this case, the system is described by Ψ^f which is given by a linear combination of the product of the molecular eigenfunctions as follows:

$$\Psi^f = C_{f1}\psi_1^1\psi_2^0 + C_{f2}\psi_1^0\psi_2^1, \tag{1.6}$$

where C_{f1} and C_{f2} are the constant coefficients that give the weight of each molecular eigenfunction in the eigenfunction of the final state. The energies of the system are determined by the transition energies of the isolated molecules ε_1 and ε_2, as well as the interaction energy terms V_{11}, V_{22}, and V_{12}. If the interacting molecules have no net charge, the interaction strength in the dipole-dipole approximation is given as follows

$$V_{12} = \frac{1}{4\pi\varepsilon_\circ} \cdot \frac{|\mu_D| \cdot |\mu_A|}{R_{DA}^3}\kappa, \tag{1.7}$$

where $\varepsilon_\circ$ is the vacuum permittivity, μ_D and μ_A are the transition dipole moments of donor and acceptor pigments, respectively. κ and R_{DA} are the orientation factor and the distance between the two molecules (the same as in equation (1.3)), respectively [16,42]. Equation 1.7 shows that the interaction strength between the two coupled molecules depends on the distance between them, and the mutual orientation.

1.5 Excitation annihilation in photosynthetic systems

It has been observed that the excitation lifetime of the photosynthetic system decreases when increasing the excitation intensity in ultrafast spectroscopy measurements [42]. Two processes are responsible for this phenomenon. The first process is called singlet-singlet (S-S) annihilation, which occurs due to dipole-dipole interaction between two singlet-excited pigments that are simultaneously present in the same domain [42]. Therefore, S-S annihilation depends on the initial number of excitation pairs that are present in a domain [42]. In this process, one of

the excited pigments decays to the ground state by transferring its energy to the other excited pigment, which is then promoted to a higher energy state, from which it will rapidly decay back to the lowest singlet-excited state via non-radiative decay [42, 49]. In principle, other products may be expected such as the loss of excitations upon collision or formation of triplet states. The S-S annihilation process is described by

$$\mathrm{Chl}^* + \mathrm{Chl}^* \xrightarrow{\gamma_{SS}} \mathrm{Chl}^* + \mathrm{Chl} \tag{1.8}$$

where Chl^* denotes a singlet-excited chlorophyll, and Chl is the de-excited chlorophyll. γ_{SS} is the overall decay rate constant for S-S annihilation (pair of excitation). From equation (1.8) it is obvious that the result of the S-S annihilation process is annihilating one of the two excitations.

The second process is called singlet-triplet (S-T) annihilation. In the S-T annihilation process the interaction occurs between a singlet and a triplet state, which can be illustrated by the following equations

$$\mathrm{Car}^{\mathrm{T}} + \mathrm{Chl}^* \xrightarrow{\gamma_{ST}} \mathrm{Car}^{\mathrm{T}} + \mathrm{Chl}$$

$$\mathrm{Chl}^{\mathrm{T}} + \mathrm{Chl}^* \xrightarrow{\gamma_{ST}} \mathrm{Chl}^{\mathrm{T}} + \mathrm{Chl} \tag{1.9}$$

where Chl^* is the singlet-excited chlorophyll and Chl is the de-excited chlorophyll. $\mathrm{Chl}^{\mathrm{T}}$ and $\mathrm{Car}^{\mathrm{T}}$ are the triplet-excited states of chlorophyll and carotenoid, respectively. $\mathrm{Chl}^{\mathrm{T}}$ formed via the intersystem crossing from Chl^*, whereas $\mathrm{Car}^{\mathrm{T}}$ obtained through triplet-triplet energy transfer from $\mathrm{Chl}^{\mathrm{T}}$. γ_{ST} is the overall decay rate constant for S-T annihilation. Other products may again be possible for S-T annihilation, however it is assumed that the most probable reaction channel is the one described by equation (1.9). Experimentally, when using a pulse of 100 fs length or less, S-S annihilation becomes the dominant process, whereas for picsecond and nanosecond pulses, S-T annihilation becomes the dominant process [42]. This is because S-S annihilation is a relatively fast process that operates on a timescale of a few picoseconds, compared to S-T annihilation which operates on a timescale of tens of picoseconds in LH-CII [50]. In this project, the S-S annihilation process in the FCPb light-harvesting complexes was investigated.

1.6 Non-photochemical quenching

Non-photochemical quenching (NPQ) is a mechanism utilised by plants, algae and cyanobacteria (i.e. all oxygenic organisms) to protect themselves from photo-oxidative damage under high light conditions. The absorption of sunlight energy is carried out by pigment-protein light-harvesting complexes. The absorbed light energy induce a singlet excitation of a Chl-a

molecule (^{1}Chl*) which can return back to the ground state through several pathways. The excitation energy can be re-emitted as fluorescence or transferred to the reaction centre and utilised to drive photochemistry (used for photosynthesis). The excitation energy can also be dissipated through the internal conversion (IC) process, non-photochemical quenching (NPQ) process, or undergo intersystem crossing (ISC) process leading to the formation of the Chl-a (^{3}Chl*) triplet state [51].

NPQ is divided into three components: ΔpH- or energy-dependent quenching (qE); state transition quenching (qT), which is more prominent in algae and correlated with regulating the distribution of excitation energy between photosystem II and I by uncoupling of some LHCII molecules from PSII and coupling them to PSI; and finally photo-inhibitory quenching (qI) [51–54]. These NPQ components have been classified according to their activation and relaxation timescales. The response times of qE are from a few seconds to minutes, qT relaxes within tens of minutes and qI decays within a range of hours [51, 55]. Alternatively, these components have also been classified by their molecular trigger mechanisms: qE is triggered by the increase in the ΔpH gradient across the thylakoid membrane and the de-epoxidation of the xanthophyll cycle pigments [55], qI by the damage of PSII [51], and qT by the reduction of the plastoquinone pool [55]. Although significant work has been done in order to understand the mechanisms behind the NPQ components, underlying mechanisms for the qE component remain controversial. For the qE process, it is proposed that the quenching of the Chls fluorescence can be induced by a conformational change, In vivo, this process occurs without aggregation [53].

The dominant and fastest process is qE. Therefore, several methods have been used to mimic the native environment to induce a quenched phase of the LHCs, in order to investigate the qE mechanism *in vitro*, with the most common methods being aggregation of the light-harvesting complexes [56,57] and assembling them into liposomes, forming proteoliposomes [58]. *In vivo*, aggregation of LHCs is triggered by the reduction of pH in the lumen surface [53]. Formation of LHC aggregates *in vitro* is achieved by removing detergent with bio-beads or using a detergent concentration below the critical micelle concentration (CMC). Micelles are small spherical aggregates of surfactant molecules dispersed colloidally in the solvent. In our research, the LHCII complexes are contained within the spherical surfaces of the micelles, if the surfactant concentration is above the CMC. Micelles are used to mimic the thylakoid membrane. This aggregation method brings about a significant decrease in the fluorescence yield and lifetime of the aggregated LHCII as compared to the solubilised complexes [53]. Formation of qE is usually accompanied by various of spectroscopic changes, a major one being the appearance of low-energy (red) species in the absorption and fluorescence spectra of LHCII [59–61]. It has been shown that, *in vitro,* aggregation forms of LHCs display similar characteristics to those that accompany qE, such as the enhancement of the low-energy species in the absorption and fluorescence emission spectra and the reduction of the fluorescence yield [53, 62].

In plants, green algae, and diatomic antenna systems, qE is triggered by the low thylakoid lumen pH, which is induced by the electron transport chain in the thylakoid membrane. Lowering of pH in the lumen also plays a significant role in the activation of the xanthophyll cycle and switching to conformations which are also involved in qE [51, 57]. These activations for conformational change and the xanthophyll cycle, have been inferred from a change in the absorption and fluorescence spectra of the these antenna complexes [53, 62]. Although diatoms exhibit robust qE that depends on a low thylakoid lumen pH and presence of a xanthophyll cycle similar to the cycle in plants and green algae, they lack a protein like PsbS which was demonstrated to be a sensor for the qE process in plant. In green algae it's called LHCSR [57, 63]. Incorporation of LHCII complexes into liposomes has shown a drastic decrease of the chlorophyll fluorescence yield and lifetime [58]. Therefore, it has also been used as a model for *in vitro* studies of NPQ in both plants and diatoms [58, 64].

1.7 Aim of this work

The process of light absorption is the first step in both natural and artificial photosynthetic systems. In photosynthetic systems, the energy absorbed by light-harvesting complexes can either be transferred to the reaction center where it is used to drive chemical reactions, or thermally dissipated by processes such as internal conversion or photoprotection. The latter minimizes the damage that can occur in the reaction center due to over-illumination. A current challenge in the field of sustainable energy development is how to improve the efficiency of artificial photosynthetic devices in order to make them perform as well as natural ones by applying the principles underlying natural photosynthesis, such as efficient energy transfer and photoprotection. These processes are not fully understood on a fundamental, quantum level. A deeper understanding of these processes therefore has great importance for the improvement of artificial photosynthetic systems.

In conducting this research, our aim was two-fold: Firstly, we aimed to develop a coherent control experiment in order to coherently control the excitation energy flow in the LHCII complex. In several previous studies, ultrafast dynamics such as energy transfer, internal conversion, and isomerization in natural and artificial molecular complexes have been successfully manipulated and investigated using coherent control in order to understand them on a quantum level [65–69]. In these studies, the pulse parameters under investigation were first optimized using pulse shaping devices in a genetic algorithm learning loop. Then, the pulse that led to achieving the best optimization was characterized and related to the molecular dynamics being controlled. In this study we aimed to adapt a transient absorption pump-probe experiment to a coherent control experiment by incorporating the pump-probe experiment in a learning loop that consists of a spatial-light modulator and genetic algorithm, and then perform a coherent control experiment

to optimize the excitation energy flow in pathways in carotenoids in LHCII. We also set as our aim the characterization of the optimal pulse using frequency resolved optical gating and relating the pulse to the mechanism being controlled.

The second major aim of this research was to investigate the energy dissipation mechanisms in the FCPb light-harvesting complex of the diatom *Cyclotella meneghiniana* using transient absorption pump-probe spectroscopy. Thermal energy dissipative processes in diatoms have been investigated using fluorescence and absorption experimental techniques [40, 64, 70–73]. These investigations showed that qE is very likely established in diatoms through the combination of multiple processes involving different sites. In a previous study, transient-absorption experiments were performed at room temperature, the kinetics and spectral properties of the quenching processes involving Chl-a pigments were investigated in FCPa by using selective Chl-a excitation [74]. The latter study was performed on FCPa complexes in their solubilized and aggregated states. In this work, we aimed at applying a similar approach to FCPb in order to characterize the quenching processes in these complexes and to determine the similarities and differences compared to how quenching takes place in FCPa.

1.8 Thesis outline

In Chapter 2, the techniques used in this work are explained in detail. These include: generation, manipulation and characterization of the ultrashort laser pulse techniques, transient absorption spectroscopy, and coherent control techniques.

In Chapter 3, the experimental setups used in this work are described. These are: the transient absorption spectroscopy setup, laser coherent control setup, frequency resolved optical grating setup and the 4F pulse shaping setup. The analysis methods for transient absorption data and calibration and characterization of the results of the 4F setup are also presented in this Chapter. The genetic algorithm and the optimization procedure used in this study are also explained in this chapter.

In Chapter 4, the experimental results of coherent control of excitation energy flow in carotenoids of LHCII are presented and discussed.

In Chapter 5, the results of transient absorption spectroscopy on the Fucoxanthin-chlorophyll protein, the main light-harvesting complex of the *diatom Cyclotella meneghiniana*, are presented and discussed.

In Chapter 6, a brief summary to results of Chapter 4 and Chapter 5 is presented.

Chapter 2

Techniques and Methods

2.1 Ultrashort laser pulse generation and manipulation

Most of the experimental works described in this study were carried out using ultrashort (femtosecond) laser pulses obtained from commercial laser systems. A femtosecond laser pulse is a laser pulse with a duration on a sub-picosecond timescale (1 ps = 10^{-12}s). Generation of a femtosecond laser pulse is achieved using mode-locked laser systems. A titanium-doped sapphire (Ti:sapphire) crystal is one of the most frequently used gain media in the resonator of a mode-locked laser system. This medium is used because it has a broad emission bandwidth ranging from 700 nm to 1100 nm and peaking at around 800 nm. Generation of a femtosecond laser pulse is usually followed by a chirped pulse amplification (CPA) technique, to produce a high peak power. In the CPA technique, the initial pulse is stretched using some dispersive optics such as diffraction gratings or prisms. Then the signal is amplified in regenerative or multipass schemes, and finally recompressed [75, 76].

Since the femtosecond laser pulse is a kind of electromagnetic radiation, it is described using the spectral E(ω) or the temporal E(t) electric fields, which are related by the Fourier Transform. In the spectral domain the electric field is written as

$$\tilde{\mathrm{E}}(\omega) = \int_{-\infty}^{\infty} \mathrm{E(t)} \mathrm{e}^{-\mathrm{i}\omega \mathrm{t}} \mathrm{dt}, \tag{2.1}$$

whereas the temporal part of the complex electric field is obtained through the inverse Fourier transform of equation (2.1)

$$\mathrm{E(t)} = \frac{1}{2\pi} \int_{-\infty}^{\infty} \tilde{\mathrm{E}}(\omega) \mathrm{e}^{\mathrm{i}\omega \mathrm{t}} \mathrm{d}\omega. \tag{2.2}$$

The complex electric field of the laser E(t) in equation (2.2) consists of both positive values, which are measurable quantities, and values that have no physical meaning (when the frequency

is negative). Thus, equation (2.2) can be written as

$$\mathrm{E(t)} = \mathrm{E^{+}(t)} + \mathrm{E^{-}(t)} \tag{2.3}$$

where $\mathrm{E^{+}(t)}$ and $\mathrm{E^{-}(t)}$ are given as

$$\mathrm{E^{+}(t)} = \frac{1}{2\pi}\int_{0}^{\infty} \mathrm{E}(\omega)\mathrm{e}^{\mathrm{i}\omega \mathrm{t}}\mathrm{d}\omega \tag{2.4}$$

$$\mathrm{E^{-}(t)} = \frac{1}{2\pi}\int_{-\infty}^{0} \mathrm{E}(\omega)\mathrm{e}^{\mathrm{i}\omega \mathrm{t}}\mathrm{d}\omega \tag{2.5}$$

Here $\mathrm{E^{+}(t)}$ has a complex value, which is usually expressed as the product of an amplitude function and phase term:

$$\mathrm{E^{+}(t)} = \mathrm{A(t)} \cdot \mathrm{e}^{-\mathrm{i}\phi(\mathrm{t})}, \tag{2.6}$$

where A(t) and $\phi(\mathrm{t})$ are the temporal amplitude and phase factors, respectively. Thus, from equation (2.6) the temporal intensity I(t) is given by

$$\mathrm{I(t)} = \frac{\varepsilon_{\circ}\mathrm{c}}{2}[\mathrm{A(t)}]^{2}, \tag{2.7}$$

where $\varepsilon_{\circ}$ is the vacuum permittivity and c the vacuum speed of light. The pulse duration $\Delta\tau$ is usually defined as the full width at half maximum (FWHM) of the temporal intensity function I(t) [77, 78]. Similarly, the complex electric field in the frequency domain is expressed as a product of the spectral amplitude $\hat{A}(\omega)$ and phase $\varphi(\omega)$ terms:

$$\mathrm{E^{+}}(\omega) = \hat{\mathrm{A}}(\omega) \cdot \mathrm{e}^{-\mathrm{i}\varphi(\omega)} \tag{2.8}$$

The spectral bandwidth $\Delta\nu$ of a pulse is related to the spectral intensity function $\mathrm{I}(\omega)$, which is given as

$$\mathrm{I}(\omega) = \frac{\varepsilon_{\circ}\mathrm{c}}{4\pi}[\hat{\mathrm{A}}(\omega)]^{2} \tag{2.9}$$

where $\hat{\mathrm{A}}(\omega)$ is the spectral amplitude. For the Gaussian laser pulse $\mathrm{E^{+}(t)}$ is given as

$$\mathrm{E^{+}(t)} = \left(\frac{1}{\sigma\sqrt{2\pi}}\right)\exp\left(-\frac{\mathrm{t}^{2}}{2\sigma^{2}}\right) \cdot \exp(-\mathrm{i}\omega_{\circ}\mathrm{t}) \tag{2.10}$$

where $\omega_{\circ} = 2\pi\mathrm{c}/\lambda_{\circ}$ is the central angular frequency and $\sigma = \Delta\tau/\sqrt{2\ln 2}$ is the standard deviation. The relation between pulse duration $\Delta\tau$ and its spectral bandwidth $\Delta\nu$ is known as the

time-bandwidth product

$$\Delta\tau \cdot \Delta\nu \geq K \tag{2.11}$$

where K is a constant which depends on the shape of the pulse. For Gaussian and Lorentzian pulse shapes, the K value is 0.441 and 0.142, respectively. Equation (2.11) shows that, for the generation of ultrashort laser pulses, one needs to use a broad spectral bandwidth [75]. Figure 2.1(a) shows a simulation of equation (2.8) of the real part of the electric field strength of a femtosecond laser pulse used in this study. Figure 2.1(b) shows the corresponding intensity profile of the pulse.

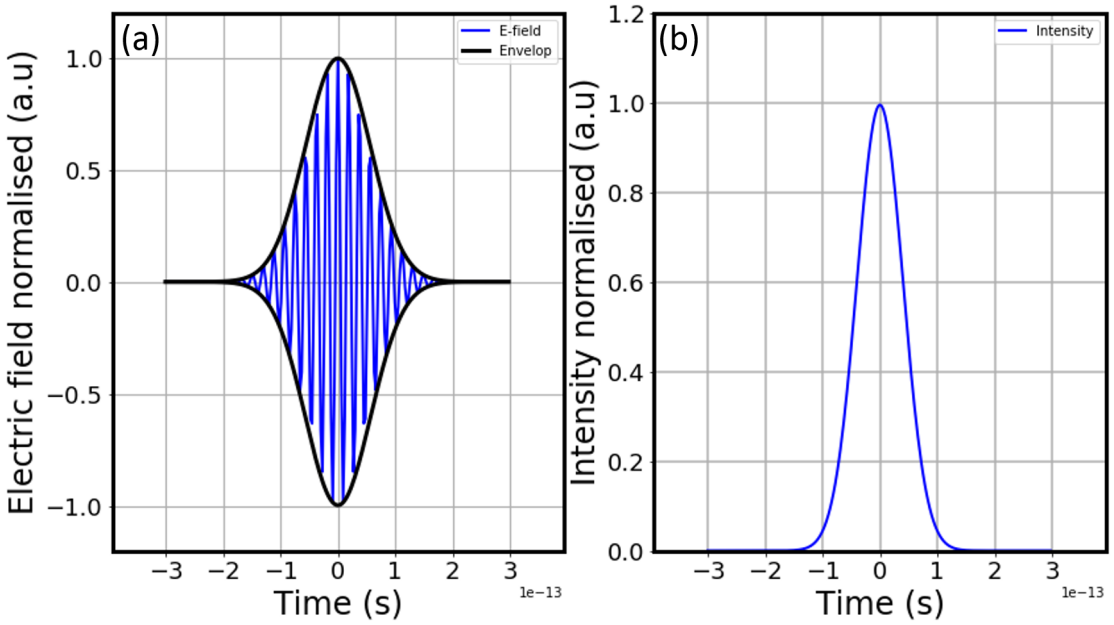

Figure 2.1: Illustration of (a) real part of an electric oscillation and envelope of a femtosecond laser pulse of a Gaussian profile; (b) its corresponding intensity, for a pulse duration of 80 fs and 775 nm central wavelength.

2.1.1 White-light continuum generation

White-light continuum generation is a process whereby narrow spectral bandwidth laser pulses are converted to pulses with a broad spectral bandwidth. The spectral broadening is achieved by focusing laser pulses into a highly non-linear optical medium [76,79]. Since its first observation by R. Alfano and S. Shapiro [79], the white-light continuum became a useful source of light in several applications such as optical parametric amplification and ultrafast time-resolved spectroscopy [79]. Self-phase modulation is thought to be the process responsible for the generation of the white-light continuum [80]. However, it has been argued that multi-photon absorption, non-linear Raman scattering, and plasma creation have a great contribution to the white-light

continuum generation. In this study only a brief description of the self-phase modulation process is provided. When an intense ultrashort laser pulses propagates through a highly non-linear optical medium it causes the total refractive index of this medium to become a function of the incident intensity [76, 81] which can be described as follows:

$$n(I) = n_\circ + n_1 I \tag{2.12}$$

where $n_\circ$ is the normal refractive index of the medium and n_1 is the non-linear refractive index which is laser intensity dependent. For a Gaussian beam, the intensity is higher in the centre than in the wings, which causes the refractive index of the material to be higher in the middle than in the wings across the beam. Consequently, the non-linear optical medium acts as a focusing lens. This phenomenon is known as self-focusing. The self-focusing effect occurs only when the power of the applied electromagnetism radiation exceeds the critical power (P_{crit}) [80–82]

$$P_{crit} = \frac{\alpha \lambda_\circ^2}{8\pi n_\circ n_1} \tag{2.13}$$

where $\lambda_\circ$ is the central wavelength of the laser pulse, and α is a constant which depends on the spatial profile of the beam. For a Gaussian beam, α = 3.77. The high intensity beam resulting from the self-focusing effect will trigger the self-phase modulation process that can be described as follows. The electric field of an incident laser pulse that propagates in the z-axis is given by

$$E(z,t) = E_\circ(z,t) \cdot e^{i(\omega_\circ t - kz)} \tag{2.14}$$

$$= E_\circ(z,t) \cdot e^{i\phi(z,t)}, \tag{2.15}$$

where

$$\phi(z,t) = \omega_\circ t - kz, \tag{2.16}$$

with k the wavenumber, defined as

$$k = \frac{n\omega_\circ}{c} = (n_\circ + n_1 I(t))\frac{\omega_\circ}{c}. \tag{2.17}$$

In the case of a non-linear optical medium of length l, and using equation (2.17), the phase can be written as

$$\phi(z,t) = \omega_\circ t - (n_\circ + n_1 I(t))\frac{\omega_\circ \cdot}{c} l. \tag{2.18}$$

The instantaneous frequency is defined as

$$\omega = \frac{\partial \phi(z,t)}{\partial t} = \omega_\circ - \frac{\omega_\circ n_1}{c} l \cdot \frac{\partial I(t)}{\partial t}. \tag{2.19}$$

Equation (2.19) shows that the change in the refractive index as a function of the applied radiation intensity induces a linear frequency broadening in the pulse. When the pulse modifies its own characteristics, the effect is called self-phase modulation. If one pulse modifies the characteristics of another, the phenomenon is called cross-phase modulation [76]. In this study, white light is used twice: firstly it is used as a seed beam in the Non-collinear Optical Parameteric Amplification (NOPA) setup and secondly, as a probe beam in the transient absorption spectroscopy and coherent control experiments.

2.1.2 Second harmonic generation

Second harmonic generation is a non-linear phenomenon in which two photons of frequency ω interact with a highly non-linear medium and generate one photon at frequency 2ω. This phenomenon is widely used in the field of laser physics to generate an ultrashort laser pulse in the ultraviolet spectral range. Second harmonic generation is described by a non-linear polarisation P of the form

$$P(2\omega) = 2\varepsilon_\circ \chi_{eff} E^2(\omega), \tag{2.20}$$

where $2\chi_{eff} = \chi^{(2)}$, with $\chi^{(2)}$ the second order non-linear optical susceptibility of the medium, $\varepsilon_\circ$ the dielectric constant of vacuum and $E(\omega)$ is the electric field vector of the incident radiation [83]. We introduce the coupled-wave equation in non-linear optics [84]:

$$\frac{\partial}{\partial z} E_n = -i \frac{\omega_n}{2 n_n c \varepsilon_\circ} P_n^{NL} \tag{2.21}$$

where the subscript n denotes the order of the harmonic generation. This equation contains critical information about the different phase relationships between the non-linear polarisation and the applied electric field [84]. By substituting equation (2.20) into equation (2.21), the wave-coupled equation for the second harmonic generation can be written as

$$\begin{aligned} \frac{\partial}{\partial z} E(2\omega) &= -i \frac{\omega}{2nc\varepsilon_\circ} P(2\omega) \\ &= -i \frac{\omega}{nc} \chi_{eff} E^2(\omega) e^{i\Delta k z} \end{aligned} \tag{2.22}$$

where Δk is the phase-matching condition.

Integrating equation (2.22) from z = 0 to z = L, where L is the length of the non-linear medium,

yields

$$E(2\omega) = \frac{\omega\chi_{eff}}{nc}E_{\circ}^{2}(\omega)\cdot(\frac{Sin(\Delta kL)}{\Delta kL})^{2}. \tag{2.23}$$

The intensity $I = \frac{nc\varepsilon_{\circ}}{2n}|E(2\omega)|^2$ of the SH wave is then given as

$$I(2\omega,L) = \frac{2\omega^2\chi_{eff}^2L^2}{n^3c^3\varepsilon_{\circ}}\left(\frac{\sin(\Delta kL)}{\Delta kL}\right)^2 I^2(\omega), \tag{2.24}$$

where $\Delta k = k(\omega) - 2k(\omega)$ for the second harmonic generation. The efficiency of the second harmonic generation is defined by

$$\eta_{SH} = \frac{I_{SH}(2\omega)}{I(\omega)}, \tag{2.25}$$

where $I(\omega) = P/A$ is the intensity of the incident radiation, A is the cross-sectional area of the interaction and P is the power of the incident fundamental radiation. Since $I_{SH}(2\omega)$ is proportional to L^2, according to equation (2.24), the efficiency of the second harmonic generation can be written as

$$\eta_{SH} = C^2\frac{L^2}{A}P, \tag{2.26}$$

where C is a constant and its value depends on ω and $\chi^{(2)}$. According to equation (2.26), to maximise the efficiency of the second harmonic generation, it is important that the incident radiation has the largest power. This is achieved using ultrashort laser pulses that are characterised by their high peak power. To prevent damage of the non-linear crystals, the incident radiation power should not exceed the power threshold of the non-linear crystals. It is also essential to maximise the ratio L^2/A, which means that the beam should be focused into a sufficiently small spot size and that an appropriate thickness for the non-linear crystal should be used. A non-linear crystal that is too thick would introduce a temporal chirp in the pulse which might affect the temporal resolution of the experiment. Moreover, a thick non-linear crystal can also convert the second-harmonic back to the fundamental wavelength, which may affect the quality of the second-harmonic beam. In this study, second-harmonic generation is used for generating a pump beam in the NOPA setup and for characterising the pump beam of a coherent control experiment in the frequency-resolved optical gating (FROG) setup.

2.1.3 Pulse shaping theory

An ultrashort laser pulse shaping system has become an important tool for both ultrafast optical science and technology [85,86]. Nowadays, shaped laser pulses are widely used in several

applications, which include ultrafast optical spectroscopy, coherent laser control, optical communication [85–87] and biological imaging [87]. The parameters of the pulse shape that can be controlled are phase, amplitude and sometimes polarisation of the pulse [86–88]. Direct control of the amplitude and phase of ultrashort laser pulses in the time domain cannot be achieved, due to the fact that the pulse duration is much shorter than the response time of most electronic instruments [89]. Modern modulators such as Mach-Zehnder modulators can only operate up to 60 GHz which corresponds to a duration of 10 ps, much slower compared to the femtosecond duration of pulses [90]. Therefore, an alternative method for shaping an ultrashort pulse was developed. In this method, a Fourier transformation of the ultrashort pulse, from the time domain to the frequency domain, is first performed. Then, the spectral phase and amplitude of the pulse are modulated using a linear filter (shaper). Thereafter, an inverse Fourier transform is performed in order to obtain the temporal modulated pulse [88].

The shaper can be described in both the temporal and spectral domain. In the temporal domain, the shaper is characterised by an impulse response function $\mathrm{R(t)}$. The electric field $\tilde{\mathrm{E}}_{\mathrm{out}}(\mathrm{t})$ of the shaped output pulse after the shaper is given by the convolution product of the temporal electric field of the input unshaped pulse $\tilde{\mathrm{E}}_{\mathrm{in}}(\mathrm{t})$ and the impulse response of the filter $\mathrm{R(t)}$ [85–87]:

$$\tilde{\mathrm{E}}_{\mathrm{out}}(t) = \mathrm{R(t)} \otimes \mathrm{E_{in}(t)}, \tag{2.27}$$

where $\otimes$ denotes convolution. In the spectral domain, the shaper is characterised by a frequency response function $\mathrm{H}(\omega)$, where the electric field of the shaped output pulse is given by the product of the electric field of the input unshaped pulse $\tilde{\mathrm{E}}_{\mathrm{in}}(\omega)$ and $\mathrm{H}(\omega)$

$$\mathrm{E_{out}}(\omega) = \mathrm{H}(\omega)\tilde{\mathrm{E}}_{\mathrm{in}}(\omega), \tag{2.28}$$

where $\mathrm{H}(\omega)$ is the Fourier transform of $\mathrm{R(t)}$ [85–87]. Several programmable shapers have been used for shaping ultrashort laser pulses, such as liquid crystal spatial light modulators (LC-SLM), acousto-optic modulators (AOM), deformable mirrors and holographic patterns [86–88,90,91]. In this work, an LC-SLM pulse shaper was used because of its high modulation efficiency, capability of polarisation control, and independence on the pulse repetition rate. Moreover, LC-SLMs have a lower cost and better intensity throughput compared with an AOM. For these reasons, it is one of the most popular pulse shapers. However, the LC-SLMs have a number of disadvantages: They have a refreshment time (defined as the time required by the LC-SLM to be oriented) of $\sim$100 μs (10 kHz) which will not work well with a laser pulse source having a repetition rate higher than 10 kHz [87]. Finally, the pixelated nature of the LC-SLM modulator can lead to temporal gaps for spectral patterns which vary too rapidly from one pixel to the next. These gaps can be corrected by programming a replica with similar intensity but opposite in phase; however, this reduces the effective number of pixels available for pulse shaping [85, 87]. The LC-SLM used in this work is described in detail in section 3.2.1.

2.1.4 Pulse characterisation techniques

Since the pulse duration of an ultrashort pulsed laser determines the time-resolution of ultrafast spectroscopy experiments, it becomes necessary to know the duration of the pulses that are used in such an experiment. Moreover, in some experimental techniques that are used to investigate the dynamics of molecular vibrations, like the coherent control technique, additional pulse details play an important role in the manipulation of the outcome of the experiments [92]. It is therefore important to have a technique that can be used for a complete characterisation of the pulses in such experiments. Several methods have been developed for characterising ultrashort laser pulses. The most widely used techniques are based on temporally and spatially overlapping the pulse with its replica or with a known pulse structure in a non-linear optical medium such as a beta Barium Borate (BBO) crystal. This allows the resulting second harmonic generated signal to be recorded as a function of the delay between the pulses, using a detector [76]. BBO crystals are the most often used non-linear optical media because of their broad phase-matching region [93]. This idea has been implemented in different ways, for example in autocorrelators, crosscorrelators and Frequency Resolved Optical Gating (FROG) devices. In the autocorrelator and crosscorrelator devices, the detection system is a photodiode and oscilloscope. In the former technique the pulse overlaps with its duplicate, while in the latter it overlaps with a reference pulse of a known profile [78]. For both techniques, if the field intensity of the two pulses is $\mathrm{I(t)}$ and $\mathrm{I(t-\Delta t)}$, respectively, the measured autocorrelation intensity of the two pulses is

$$\mathrm{I_{intAC}}(\tau) = \int_{-\infty}^{\infty} \mathrm{I(t)I(t-\Delta t)dt}, \tag{2.29}$$

where Δt is the time delay between the two pulses. Autocorrelation intensity is described by a symmetric function that has its maximum at $\Delta \mathrm{t} = 0$ [78]. The autocorrelator and crosscorrelator techniques can only provide limited information about the temporal profile of the pulse, but they do not give information about the phase of the pulse because the photodiode can only measure intensity and not the spectrum. Moreover, they cannot be used to characterise complex pulse shapes. A superior alternative, called the FROG technique, was invented by Rick Trebino in 1991 [92]. It allows for the characterisation of ultrashort laser pulses in both time and frequency domains [92]. In the FROG technique, the detection system consists of a spectrometer and computer. The spectral signal of the FROG can be described mathematically by

$$\mathrm{I_{FROG}^{SHG}}(\omega, \tau) = \left| \int_{-\infty}^{\infty} \mathrm{E(t)E(t-\Delta t)} \exp(-\mathrm{i}\omega \mathrm{t}) \mathrm{dt} \right|^2 \tag{2.30}$$

with Δt being the relative delay between the pulses, $\omega = 2\pi \mathrm{c}\lambda$ being the angular frequency and λ is the wavelength and c is the speed of light in vacuum. Therefore, FROG provides temporal and spectral information of the pulse. In this study we used our home built FROG setup for the

characterization. The experimental setup of the FROG technique is discussed in section 3.4.

2.2 Ultrafast laser spectroscopy and control

Investigation of ultrafast molecular dynamics such as energy transfer between chromophores, internal conversion, and intersystem crossing, requires a spectroscopic technique with a temporal resolution that is relatively faster than the processes' timescale. Such techniques have nowadays become possible through the use of ultrashort laser pulses, which have pulse durations comparable to the timescale of ultrafast molecular dynamics [94]. The most used techniques are: transient absorption spectroscopy also known as pump-probe spectroscopy [95–97] in which the absorption signal of the excited sample is monitored as a function of time, time-resolved infrared spectroscopy [98], four-wave-mixing spectroscopy [99], two-dimensional optical spectroscopy, and laser coherent control [65, 67, 100–103] techniques. These techniques are known as absorption techniques because they rely on the absorption signal of an excited sample. However, in some other types of ultrafast spectroscopy experiments, the fluorescence of an excited sample is monitored as a function of time. These types of experiments are known as time-resolved fluorescence techniques [104], which includes: fluorescence up-conversion [105], streak camera [106], time-correlated single photon counting [104], phase-modulation [105]. In this project, we used pump-probe spectroscopy and coherent control techniques, therefore we described them in more detail in sections 2.3 and 2.4, respectively.

2.3 Transient absorption spectroscopy

The transient absorption spectroscopy approach is typically used to investigate the ultrafast dynamics of a light sensitive molecular system. Figure 2.2 shows a typical scheme for transient absorption spectroscopy. In this technique, an ultrashort pump pulse is used to promote molecules to their electronically excited state. The excited state dynamics of the molecules are then monitored by a weak probe pulse sent through the sample with a delay (τ) relative to the pump pulse [97]. The probe beam can be a white light continuum. The pump beam is usually obtained from a tunable laser source and is used to promote electrons from a lower energy level in an atom, molecule or molecular complex in the sample under the investigation to higher energy levels. This beam will be blocked after passing through the sample [94]. The resulting absorption spectrum of the probe after the sample is measured as a function of the delay time (τ) between the pump and probe pulses, using a detector [76]. A mechanical chopper wheel was positioned in the path of the pump beam, in order to allow measurement of the probe intensity alone in the excited (pumped) or unexcited (unpumped) system. In this way, the difference in absorption (ΔOD) can be obtained. By changing τ between the two pulses

and recording the spectrum of ΔOD at each delay time, a set of $\Delta OD(\lambda, \tau)$ will be obtained. This set contains important information about the ultrafast dynamics of the excited state of the molecules [96, 97].

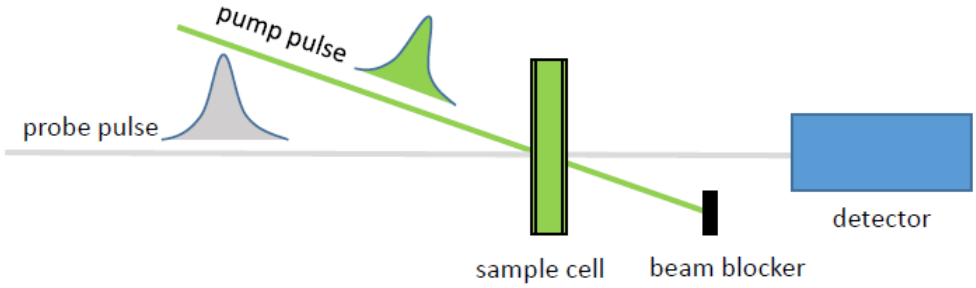

Figure 2.2: Illustration of the transient absorption spectroscopy technique.

Using the Beer Lambert law for linear absorption in a liquid sample, the measured absorption signal of the probe pulse is expressed as:

$$OD(\lambda) = -\log_{10} \frac{I(\lambda)}{I_{\circ}(\lambda)}.$$

From this equation follows:

$$\begin{aligned} \Delta OD =& OD(\lambda, t)_{on} - OD(\lambda)_{off} \\ =& -\log_{10} \frac{I(\lambda, t)_{off}}{I_{\circ}(\lambda)_{on}} \end{aligned} \tag{2.31}$$

with $I(\lambda)$ and $I_{\circ}(\lambda)$ being the transmitted probe intensities through the sample when it is excited and not excited, respectively. $OD(\lambda, t)_{on}$ and $OD(\lambda)_{off}$ are the absorption signals when the pump is on and off, respectively [96, 107]. ΔOD, in fact, often consists of signals from four processes at least. The first signal is the ground state bleaching (GSB), which occurs when the pump pulse populates the excited state of the molecules. In this case, relatively few molecules remain in the ground state compared to the number of molecules in the ground state for the unpumped sample. As a result, a negative signal located in the absorption region of the molecules is observed in the ΔOD spectrum as shown in Figure 2.3 (dotted line).

The second contribution is from the stimulated emission (SE) process. If we consider a two-level system, the pump pulse populates the excited state of the system, while the probe pulse induces stimulated emission. The emitted photons propagate in the same direction as the probe pulse and therefore will be detected. Consequently, this process results in a negative signal in the stimulated emission region of the ΔOD spectrum, as depicted in Figure 2.3 (dashed line). The SE spectrum is Stokes-shifted relative to the GSB spectrum. This shift is due to the vibrational relaxation that happens within the excited state before stimulation emission occurs.

The GSB and SE bands are typically broad, moreover in many systems, the Stokes shift of the SE is small, and as a result, the GSB and SE signals overlap. For such a system, the bands merge into one signal.

The third contribution is excited-state absorption (ESA). As the pump populates the molecular excited state, optically allowed transitions to high-lying excited states may occur from the initially excited state. Consequently, a positive signal in the ΔOD spectrum is measured in the wavelength region of the ESA of the molecules, as shown in Figure 2.3 (dashed-dotted line). However, due to the weakness of the probe beam intensity, the population of the exited state is not affected appreciably by the ESA process [97]. The fourth contribution may arise from absorption due to a photoproduct. This occurs after excitation of biological molecules like photosynthetic systems. Following excitation, reactions may produce long-lived molecular states, such as triplet-molecular states and charged-separated states, or lead to the formation of different isomers. These new states yield a positive signal in the ΔOD spectrum [97].

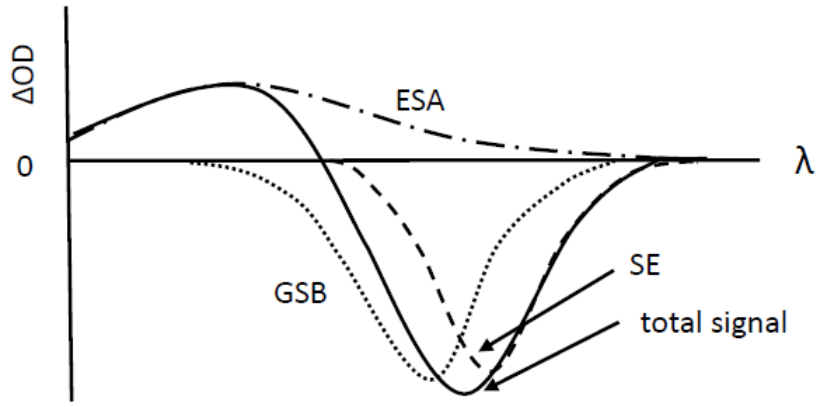

Figure 2.3: Illustration of the components of the measured probe beam spectrum. GSB-ground state bleach, SE-stimulated emission, ESA-excited state absorption, ΔOD-difference in absorption, and λ-wavelength.

2.4 Ultrafast laser control techniques

The coherent control technique is an approach that is used to manipulate the dynamics of wavepackets in molecular excited states, in order to guide the outcome of photophysical and photochemical reactions in a desired direction [102, 108], using an external electromagnetic field in the form of ultrashort laser pulses. Coherent control experiments require laser pulses with a duration shorter than the inherent molecular dynamics of the system in order to excite coherent superpositions of quantum mechanical states such as vibrations and rotations, which are observed as coherent wavepacket dynamics [109]. Several approaches have been proposed for controlling the ultrafast molecular dynamics by changing the characteristics of the applied

field. The three most successfully implemented ones are: a time-resolved scheme (also known as pump-dump scheme) proposed by Tannor, Kosloff and Rice (1986) [100]. In this scheme, a sequence of ultrashort laser pulses is used to manipulate the vibrational wavepackets on the potential surface of the electronic excited state of a molecule [108–111]. The experimental demonstration of this method was achieved by Gordon and coworkers in 1991 [112].The second approach is a frequency-resolved scheme (also known as the phase-control scheme) proposed by Brumer and Shapiro (1986) [101]. This approach exploits the quantum interference between different light-induced reaction pathways as a control parameter for the outcome of the reaction [108–110]. Experimental success of this method was demonstrated by Baumert and coworkers [113]. The third approach focuses on the stimulated transition induced by the effect of Raman adiabatic passage (STIRAP). Bergmann and coworkers demonstrated the feasibility of this approach (1998) [114]. The approach relies on a Raman-type transition that is induced by a pair of pulses [109], where one of the fields couples the ground state with the initially excited state, and the other field couples the initially excited state with the state of which population is desired [109, 110].

Although the possibility of coherent control with these approaches was demonstrated experimentally, some limitations are encountered when these techniques are applied to complex large molecular systems. These limitations originate from the fact that most of these proposed approaches allow only a single parameter of the applied electric field from the laser to be controlled at a given time. This parameter can be pulse amplitude, relative phase between two pulses, linear-chirp, polarization or time delay between two pulses. These types of control work well for simple systems (consisting of two or three atoms) with calculatable quantum dynamics. However, these approaches are insufficient for large molecular systems, which possess complex multidimensional potential energy surfaces [110]. Therefore, a number of theoretical studies were conducted to generalize these approaches to allow changing multiple parameters simultaneously in order to obtain pulses with complicated shapes, which lead to more precise control of the ultrafast dynamics of large molecules. How to find the optimal pulse shape practically, however, has been the main challenge for all suggested approaches [110].

The development of computer-controlled ultrafast laser pulse shapers and automatic feedback control methods has led Judson and Rabitz (1992) [102, 115] to overcome the above-mentioned limitation of practicability. They proposed the utilization of a learning algorithm in order to obtain the optimal field [102, 115]. In their scheme, they connected the molecular system under investigation, the laser pulse system (pulse shaper) of which the parameters are controlled by a computer and the measurement devices (detector) in a closed-loop, as illustrated in Figure 2.4.

A genetic algorithm was used to optimize the pulse-shaping parameters, using continuous outcome evaluation from the detectors. In this approach, the detector sends the feedback results to the GA code that evaluates the fitness of the obtained pulse. The GA algorithm retains a set of

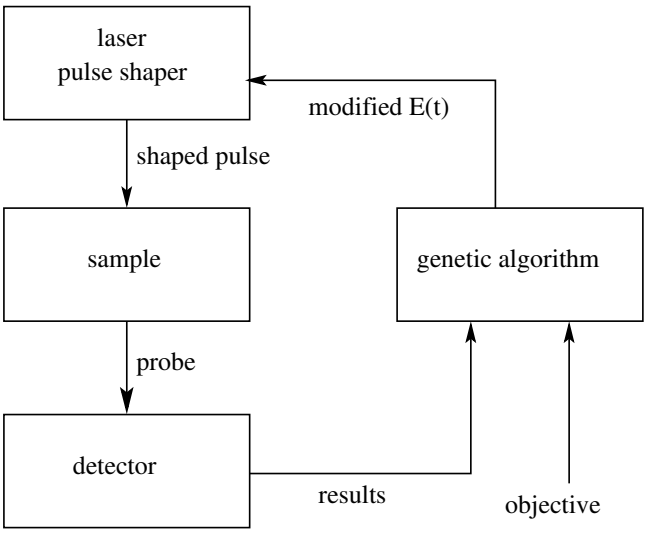

Figure 2.4: Block diagram of the coherent control scheme using a learning algorithm, pulse shaper, molecular system under investigation and measurement device in a closed-loop system.

parameters that gave the fittest outcomes, and adapts this set (see explanation below) in order to generate new candidate pulse shaping parameters. The algorithm then provides the pulse shaper with these candidate parameters (in the form of voltages for generating a new complex pulse sequence), records the fitness of the result, and feeds it back into the algorithms for the generation of new candidates. This process is continued iteratively until convergence within a specified limit is achieved. Practically, this method has been successfully implemented by several groups to control ultrafast dynamics of a number of large molecules, relying on one of the basic control theories [65–67, 69, 103, 116]. The ultrafast molecular dynamics that have been successfully controlled so far are dissociation, ionization [112], isomerization [69], charge transfer, energy transfer path ways [67, 116] and molecular vibrations [103].

In general, the purpose for most of the conducted control experiments on ultrafast molecular dynamics falls under the following three examples: Firstly, the technique can be utilised as a tool for understanding the underlying dynamics of certain photoreactions (photochemical and photophysical). Such investigations are done by characterising the optimal laser pulse shape needed to optimise yield of a specific reaction product. Secondly, coherent control can be used as a tool to transfer a molecule to a specific state that is hard to reach thermodynamically, in order to synthesize a new product that can then be further investigated by other ultrafast spectroscopic methods. Thirdly, coherent control is a potential method for controlling reactions in large molecules with complex structure, such as biological molecules that exhibit complex chemical reactions. By controlling these reactions one can investigate the underlying mechanisms in these complexes. Examples of the effective coherent control of dynamics in large complexes include the investigation of isomerization of *retinal bacteriorhodopsin* (BR) [66], control of the excited state energy flow in an artificial light-harvesting complex [68, 117], as

well as in natural complexes such as the light-harvesting complex LH2 from *Rhodopseudomonas acidophila* [67]. The energy transfer step is one of the important primary processes that determine the efficiency of the natural and artificial light-harvesting complexes. In the latter investigation, the aim was to control the energy flow process in order to understand the underlying mechanisms that would help in the development of a more efficient artificial light harvesting complex [68], since energy transfer to a desired molecular destination competes with other loss channels, such as fluorescence.

In the present study, I utilised the time-resolved control scheme for developing an experimental setup and protocol for controlling the energy transfer pathways in light-harvesting complexes II (LHCIIs) of higher plants. In this study, I incorporated a 4f pulse shaping setup, a pulse characterization (FROG) setup and the traditional pump-probe setup into a closed-loop experiment with a genetic algorithm (GA) in order to perform the laser control experiments. In this loop, the GA code iteratively optimizes the pulse shape until a satisfactory solution (defined by the convergence condition) is achieved. The laser control techniques that are developed in this study, are presented in Chapter 4.

Chapter 3

Experimental setup

In this study, the existing pump-probe setup at the National Laser Centre (NLC) of the Council for Scientific and Industrial Research (CSIR) in South Africa, was adapted to carry out coherent control measurements on LHCII. The setup is described in section 3.1.1. For the energy transfer dynamics in the diatom light-harvesting complexes, we used two pump-probe setups [29, 97] of LaserLaB Amsterdam. A brief description of this setup is given in section 5.2.2.

3.1 Transient absorption spectroscopy setup

3.1.1 Overview

Figure 3.1 gives a schematic illustration of the pump-probe experimental setup at the NLC. The experiment is driven by a femtosecond laser source described in section 3.1.2. The BS1 beam splitter is mounted in the path of the output beam to split the fundamental beam into two parts. One part is reflected to pass through the non-collinear optical parametric amplifier (NOPA) setup and the compressor (COMP) setup. These two setups are described in section 3.1.3. The beam after the COMP setup is directed to pass through the chopper and is focused by the lens L6 onto the sample. This beam is then blocked. The transmitted part of the fundamental beam is directed to the delay line and then to the photodiodes PD1 and PD2, which are used to synchronize the detection system with the chopper, and monitor the stability of the laser power. The CDP synchronisation device model 2024A S/N 706241 was used in this setup. This beam is then used to generate the white-light continuum (WL) for the probe and reference beams. Both beams are allowed to propagate through the sample and are then sent to the spectrograph (SPECT) via the optical fibers OF1 and OF2. The spectrograph disperses them onto the photodiode array (PDA) detection system. Generation and detection of the probe and reference beams are explained in section 3.1.4.

3.1.2 Femtosecond pulses laser source

In this study, the commercial Clark-MXR CPA-2110i, femtosecond pulsed laser source was used. In this system, a mode-locked fibre laser oscillator centred at 775 nm wavelength pumped with a diode laser. The output from this oscillator is used as a seed beam in a regenerative amplifier cavity. The seed beam was stretched first in order to avoid damage to the optics inside the amplifier cavity and then amplified using a Ti:Al_2O_3 amplifier and the second harmonic signal of the Nd:YAG laser (of wavelength 532 nm and 7 W power). After being amplified these pulses are recompressed in order to obtain ultrashort pulses. The resulting output beam has of 80 fs duration with an average power of 1 W (1 mJ/pulse), at a repetition rate of 1 kHz, with 775 nm central wavelength [118]. The output beam of the laser source is split by a beam splitter (BS1) into two parts: 40% is reflected and is used for generation of the pump beam and 60% is transmitted through BS1. A small portion of the transmitted part of the laser power is used to generate the probe beam.

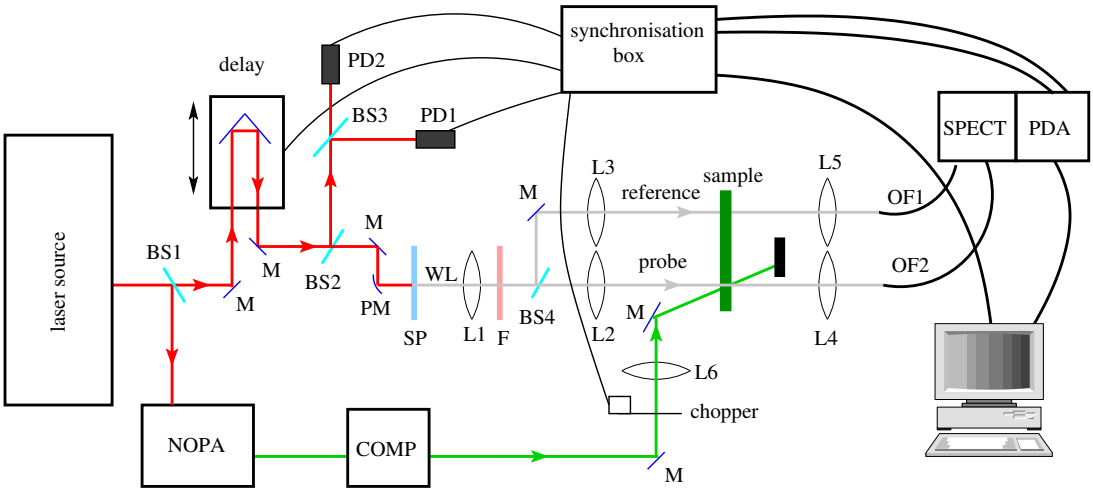

Figure 3.1: Schematic illustration of the pump-probe setup at the NLC: Key: COMP-compressor, NOPA-non-collinear optical parametric amplifier, SP-sapphire plate, F- path filter, BS1, BS2, BS3 and BS4-beam splitters, M-mirror, PM- parabolic-mirror, WL-white light continuum, L1, L2, L3, L4, L5, and L6-lenses, SPECT- spectrograph, OF1 and OF2- optical fibres, PD1 and PD2- photodiodes, and PDA- photodiode array.

3.1.3 Generation and compression of the pump pulse

In this section, we describe the generation of the pump pulse. From the beam splitter, the 40% of the fundamental beam that is reflected, is sent through a double-staged NOPA setup. This setup is used for tuning the wavelength of the fundamental beam from 775 nm to the desired wavelength in the visible range (470-680 nm), using a WL-seed beam and SH pump light at 387.5 nm. In this study, the commercial NOPA setup from Clark-MXR, Inc. [119] was used. Figure 3.2(a) is a schematic illustration of the NOPA setup used in this study. The first stage

is used to generate the pump beam at a specific wavelength, while the second stage is used to amplify the power of the pump signal that is generated in the first stage. The input beam is

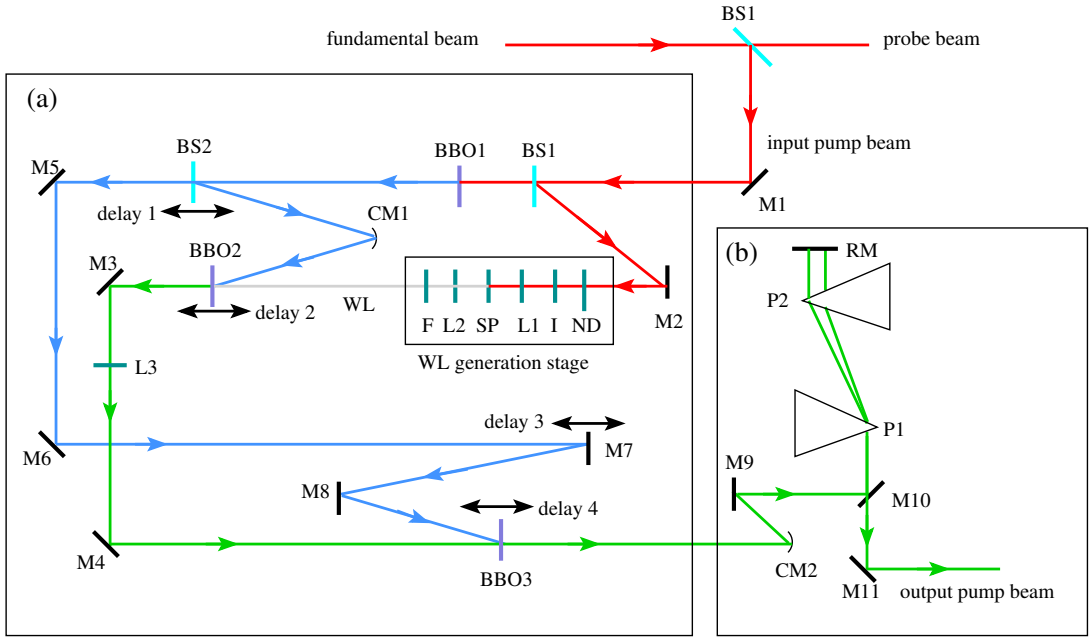

Figure 3.2: Scheme of the NOPA (a) and compressor (b) setups. Key: BS1, BS2, and BS-beam splitters, BBO1, BBO2 and BBO3, Beta-barium borate crystal. M-mirrors, CM-concave mirrors, ND- neutral density filter, I- iris, L1 and L2- lenses, P- prisms, RM- retro-reflecting mirror, SP- sapphire plate, F-filter, WL- white light continuum.

split by beam splitter BS1 into two parts. 5% of the light is reflected, and used for the WL-seed generation. Using the mirror M2, this part of light is directed to the WL-seed generation stage. The latter consists of several optical components that are used for controlling the light before and after the sapphire plate (SP), where the WL-seed beam is generated. Before the SP crystal, a neutral density (ND) filter and an iris (I) are used to control the intensity of the beam, which is an important step that helps in obtaining a single white light filament. A convex fused silica lens (L1) is then used to focus the beam into the SP crystal. This lens is mounted on an XYZ stage to maintain alignment and to move the beam focus from the front surface of the SP crystal to protect it from being damaged by high-intensity light, that may have intensity beyond the damage threshold of the SP. Another convex fused silica lens (L2) is placed after the SP and before the first amplification stage to refocus the WL-seed beam inside the BBO2 crystal. Finally, a band-pass filter (F) is positioned in the WL-seed beam path to remove light around the fundamental beam wavelength, and thereby improve the WL-seed light intensity distribution.

The 95% transmitted part of the input beam is used to generate the second harmonic (SH) pump light. This beam passes through the BBO1 crystal, where it is converted to SH pump light at 387.5 nm. Then 20% of the SH pump light is reflected by the BS2 beam splitter to the CM1 concave mirror, which focuses the beam into the BBO2 crystal. The mirror CM1 is also

used to align the SH pump light to overlap at an adjustable angle (phase-matching angle) with the WL-seed beam inside the BBO2 crystal in order to generate the pump beam at the desired wavelength in the visible range. Tuning of the wavelength of the pump beam is achieved by changing the phase-matching angle using the mirror CM1, and tuning offset using the variable translation stage of BS2 in order to adjust temporal overlap of the SH pump light with the WL-seed beam inside the BBO2 crystal. After the BBO2 crystal the SH pump light is blocked, while the generated pump beam is directed via the mirrors M3 and M4 to the BBO3 crystal for the second amplification stage. The lens L3 refocuses the WL-seed beam into the BBO3 crystal.

Using mirrors M5, M6, M7 and M8, the 80% transmitted part of the SH pump signal after the beam splitter BS2 is directed to pass through the BBO3 crystal. The transmitted part of the SH pump light is again aligned to overlap with the generated pump beam at an adjustable angle inside BBO3 for the second amplification stage. M7 is mounted on a variable translation stage to optimise the temporal overlap and the phase-matching angle inside the BBO3 crystal. The BBO2 and BBO3 crystals are mounted on a mechanical translation stage in order to optimise the spatial overlap of the SH pump light with the WL-seed and pump signal inside the crystals. The SH pump light is blocked after the second amplification stage, while the pump signal is sent to the compressor setup (COMP).

When a femtosecond laser pulse propagates through a transparent medium, it encounters a positive chirp because of group velocity dispersion inside the medium. The NOPA setup consists of several lenses and crystals that induces a positive chirp into the pump beam pulses. The positive chirp usually increases the pulse duration. It occurs when the longer wavelength (red part) components propagate slower than those with shorter wavelength (blue part). Therefore, it is necessary to have an optical system that delivers a negative group velocity dispersion after the NOPA setup, in order to recompress the pulse. The so-called prism or diffraction grating pulse compression are common methods used to accomplish compensation for the positive chirp. These systems are based on an angular dispersion that is induced by prisms and gratings [43]. In such a system, the blue spectral components travel faster than the red spectral components. In this study the prism pulse compression setup shown in Figure 3.2(b) has been used. The setup is formed by two fused silica prisms (P1 and P2) in a folded configuration with a 900 mm distance between the prisms. P1 disperses the light, whereas P2 collimates the beam. Using a retro-reflecting mirror (RM) the beam is sent back to pass through the prism pair again. This causes the red part of the beam to propagate a longer distance inside P2 than the blue part. When the P1 beam is refocused, the positive chirp is recovered. The retro-reflecting mirror RM is slightly tilted upward, so that the reflected beam pass over the M10 mirror. Using our home-built FROG setup (described in section 3.4) the temporal and spectral profile of the excitation pulses was measured after the compression. Figure 3.3 (a) and (b) show the FROG traces and the intensity autocorrelation of the pump beam after the compression, respectively. It has 30 fs

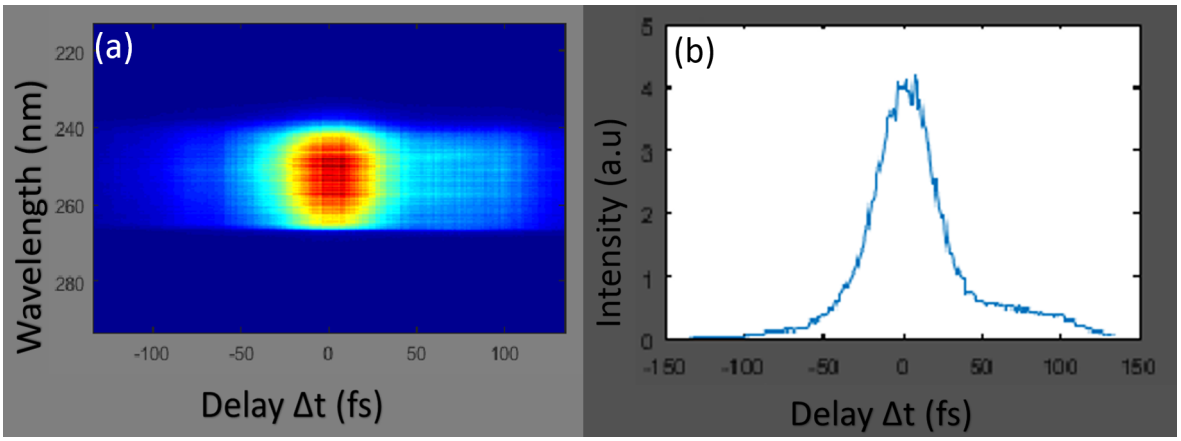

Figure 3.3: (a) experimental SHG-FROG traces and (b) its intensity autocorrelation of the pump beam of λ = 506 nm, after compression.

duration and 25 nm bandwidth calculated at the FWHM. The pump pulse after compression is directed by M11 to be chopped mechanically using a chopper (Figure 3.1) that is synchronized with the delay-line, in order to allow probing of the sample when is excited (pump-on) and not excited (pump-off). Thereafter the beam is focused onto the sample using lens L6 with 150 mm focal length. This beam is then blocked after passing through the sample with a beam blocker. The spot size of the pump beam at the sample position is 200 μm, measured with a ThorLabs DCC1545M CMOS camera.

3.1.4 Generation and detection of the probe pulse

The transmitted beam is sent through a delay-line of 30 cm (2 ns) length, and a small part of this beam is directed by beam splitters BS2 and BS3 to the photo-diodes PD1 and PD2, respectively. PD1 is used for the delay-line and chopper synchronisation, and PD2 for monitoring the laser power stability during the measurement.

Using a parabolic mirror (PM) of 200 mm focal length, the main beam is focused on a sapphire plate (SP) of 2.2 mm thickness to generate the white light (WL) continuum. Thereafter, lens L1 (Figure 3.1) with a 50 mm focal length, is used to collimate the WL, and the 700 nm short-pass filter (F) eliminates the residual fundamental light at 775 nm from the WL. Finally, the WL is split by the BS4 50/50 beam splitter into two, called the probe and reference beams. Both beams are focused on the sample using two identical lenses (L2 and L3) of 150 mm focal length. The probe beam is aligned in such a way that it overlaps spatially and temporally with the pump beam in the sample. While the reference beam passes through the sample without overlapping with the pump beam, the probe is used to maintain the WL continuum shot-to-shot intensity fluctuations. Both beams have a spot size of 150 μm.

Both probe and reference beams are focused by two identical lenses (L4 and L5) of 100 nm

focal length onto optical fibers (OF1 and OF2), after which they are dispersed with a CDP spectrograph (model 2022iS/N706222) on a photo-diode array (PDA). The sample holder is mounted on a mechanical shaker in order to prevent sample degradation. In this study, the commercial ExciPro setup was operated using ExciPro data acquisition software version 2.4.3 [120].

3.1.5 Transient absorption data analysis methods

A transient absorption spectroscopy measurement yields three-dimensional data. It is viewed on a two-dimensional graph as absorbance change (ΔOD) as a function of the delay time (τ) between the pump and probe pulses, and of the wavelength (λ) of the probe pulse. ΔOD(t) alone is defined as a kinetic trace, whereas ΔOD(λ) is known as a spectrum. For a simple and quick investigation of the data, it is typically possible to look at the evolution of any kinetic trace at the selected wavelength λ. It is also possible to look at the features (GSB, SE and ESA) of any spectrum at the selected delay time (t). This method of initial investigation is usually used to get a glimpse of an expected or unexpected feature. However, the transient absorption data usually consist of a few hundred spectra times few tens of kinetic traces. In order to extract valuable information from this type of data, global and target analysis methods [121, 122] can be employed. These methods of analysis provide quantitative information of dynamics that take place in a molecular system after excitation, using a sum of exponentially decaying and exponential growth functions convolved with the Instrument Response Function (IRF) [121, 122].

Before explaining global and target analysis methods, a brief summary of the molecular dynamics after excitation is necessary. Excitation of molecular systems leads to the promotion of electrons from the ground state to an excited state. Considering a simple two-level system having a ground state E0 and an excited state E1, where the system is excited to E1 with a pump beam, the excitations can decay back to E0 with a certain probability. This process can be expressed mathematically using exponential decay and growth functions for the E1 and E0 levels, respectively:

$$E0 = E0_0 \cdot \exp\left(-\frac{t}{\tau}\right) \tag{3.1}$$

$$E1 = E1_0 \cdot \left[1 - \exp\left(-\frac{t}{\tau}\right)\right] \tag{3.2}$$

where $E0_0$ and $E1_0$ are the initial populations of the two levels and τ is the average lifetime of E1. However, in the case where the excited sample consists of complex molecules with two or more excited states, multiple excitation decay pathways are possible and a multi-exponential function is needed in order to describe the sample dynamics correctly.

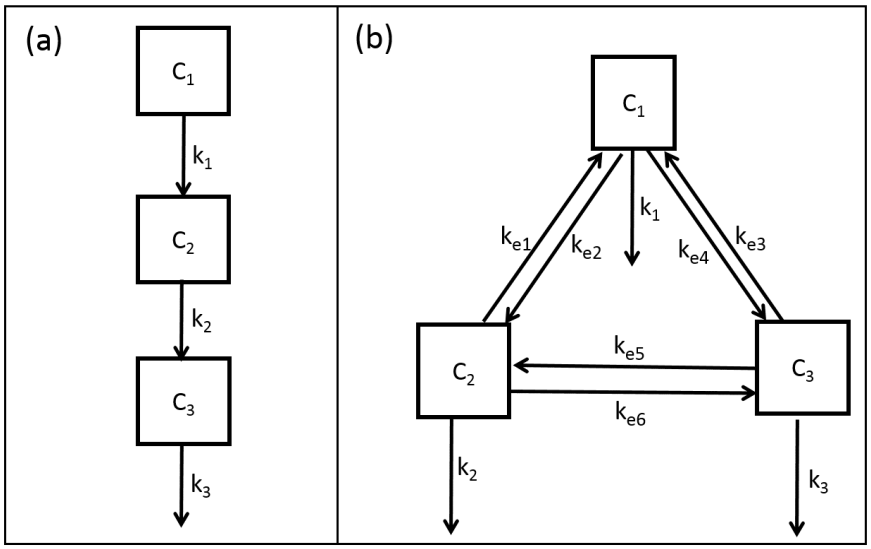

Figure 3.4: Schematic illustration of (a) global analysis and (b) target analysis for a three compartment system

In global analysis, the transient absorption data of a complex molecular system are presented by a number of compartments with specific spectral properties connected by linear kinetic rates. Figure 3.4(a) presents a simple sequential global analysis model consisting of three compartments. In the sequential model the back-reactions are omitted, based on the assumption that the losses are larger than the back-reactions [121]. The first compartment (C_1) is populated by an input excitation pulse I(t) at t =0 (no delay time between the pump and probe pulses). Subsequently, C_1 decays into the second com- partment (C_2) with decay rate constant k_1. Therefore, C_2 is populated with a rate constant k_1, and simultaneously depopulated by decaying into the third compartment (C_3) with a decay rate constant k_2. This process continues until the final compartment decays into the ground state. Therefore, the evolution of the population of several compartments can be described using the following differential equations:

$$\frac{dC_1(t)}{dt} = I(t) - C_1 k_1 \tag{3.3}$$

$$\frac{dC_i(t)}{dt} = k_{i-1} C_{i-1} - k_i C_i(t) \qquad i \neq 1 \tag{3.4}$$

In both global and target analysis methods, the number of compartments is estimated using singular value decomposition (SVD), that is also used as a results-inspection tool to check the quality of the fit and determine if additional compartments need to be included in the model. The global analysis fit yields the Evolution Associated Difference Spectra (EADS) with their associated lifetimes. EADS is regarded as an average state of the system, which describes dynamics of a mixture of molecular states.

In the target model, the analysis is made more realistic, by branching the sequential model in such a way that describes the true underlying photochemical or photophysical processes. The rate constants that are associated with each process are obtained and back-reactions can also be considered in the target model. The initial values of the parameters in the target analysis are estimated from the results of the global analysis fit. Target analysis yields the species associated difference spectra (SADS) that describe dynamics of pure molecular species associated with each compartment in the analysis model. Figure 3.4 (b) shows an example of a target analysis model used in this study. It consists of three compartments (C_1, C_2 and C_3), with k_1, k_2, and k_3 decay rate constants of the compartments. The rate constants k_{e1}, k_{e2}, k_{e3}, k_{e4}, k_{e5}, and k_{e6} here represent the equilibration (energy transfer between pigments) rate constants between the compartments.

3.2 Experimental setup for coherent control

The transient absorption setup described in section 3.1 was adapted to carry out coherent control experiments, by adding a 4F setup for pulse shaping and a FROG setup. Figure 3.5 shows a schematic illustration of the coherent control setup. The 4F and FROG setups are described in sections 3.2.1 and 3.4, respectively. The optimisation and searching approaches for the best solution in the coherent control experiments were carried out using a home-developed Genetic Algorithm (GA) code that is described in section 3.5. The FROG and 4F setups, as well as the transient absorption setup with its operational softwares, and the GA code were operated with our home-developed GUI code in MATLAB. Both the GUI and GA codes were developed by Dr. A. J. Hendriks [123].

3.2.1 Experimental setup for 4F pulse shaping

In this work the folded geometry 4F setup was designed as illustrated Figure 3.6. The setup consists of a diffraction grating (DG), a convex lens (L), a liquid crystal (LC) spatial light modulator (SLM) with a plane mirror attached behind its LC, and a polarising beam splitter (PBS) placed on the path of the output beam. The plane mirror is used to retro-reflect the beam to propagate again through the SLM, lens and diffraction grating. In the second path the lens and diffraction grating reverse their functions. This setup allows a broader amplitude and phase modulation because the beam passes twice the SLM, and easy to align and to almost get it aberration-free [87].

The incident beam is first dispersed with DG into its frequency components, after which, using a plano convex lens the dispersed frequency components of the incident beam are collimated. These frequency components of the incident beam are sent to the SLM. The dispersion allows

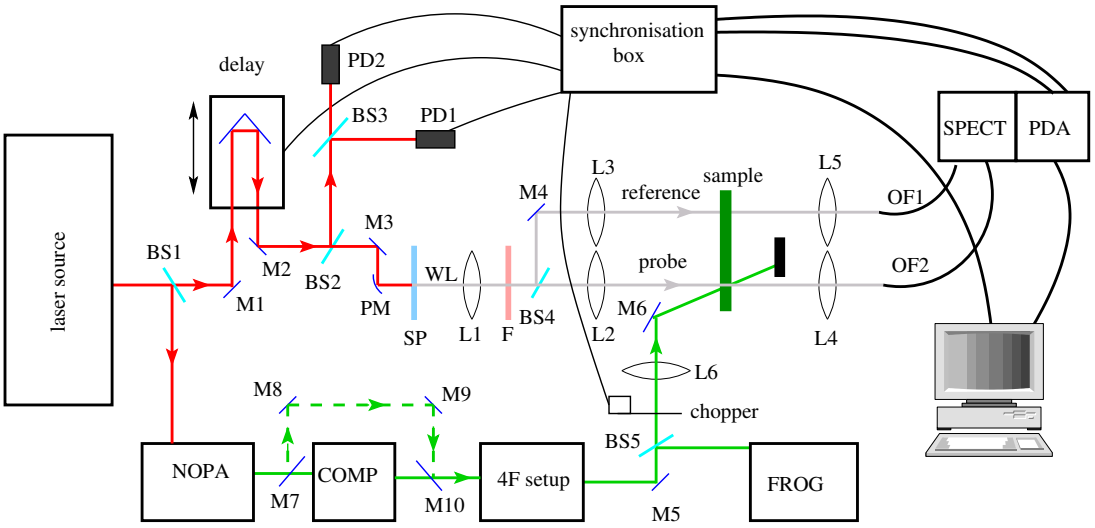

Figure 3.5: Schematic illustration of the coherent-control setup at NLC: COMP-compressor, NOPA-non-colinear optical parametric amplifier, SP-sapphire plate, F-path fliter, BS1-, BS2-, BS3-, BS4-, and BS5-beam splitters, M-mirror, PM-parabolic-mirror, WL-white light continuum, L1, L2, L3, L4, L5, and L6-lenses, SPECT- spectrograph, PD1- and PD2-Photodiodes, PDA-photodiode array, 4F-setup- 4F-pulse shaping setup, FROG-frequency resolved optical-gating setup.

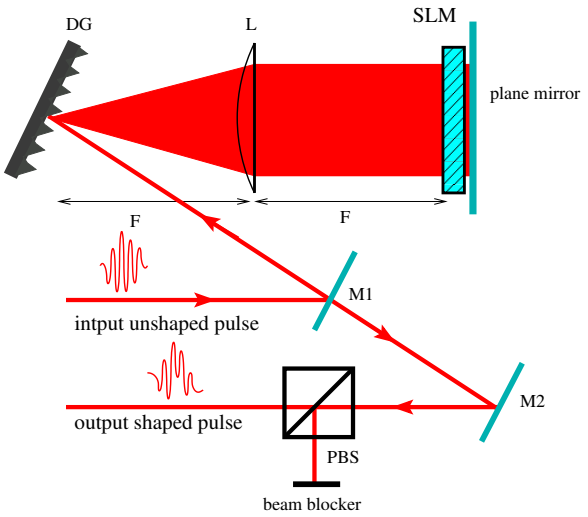

Figure 3.6: Layout of the folded geometry 4F-setup. Key: DG-diffraction grating, L-plano-convex (cylindrical) lens with a focal distance of F = 3= mm, SLM-spatial light modulator, M1- and M2-mirrors, PBS-polarising beam splitter

the pixels of the SLM to modulate each spectral component separately. The modulated beam passes through the SLM and is retro-reflected to a small vertical tilt by the plane mirror to pass through the SLM again, which modulates the beam again. The reflected beam is now focused by the lens on the diffraction grating, which will recombine the ultrashort into a small beam of 3-5 mm diameter. The beam after compression is 90% horizontally polarised and 10% vertically polarised. The diffraction grating used in this setup was designed for horizontally polarised light; therefore, a polarising beam splitter (PBS) was introduced on the output beam

path to remove the unshaped vertically polarised components. We used a cylindrical lens with antireflection coating for visible light (400-700 nm) with a size of 62×62 mm and a focal length of 300 mm, hence the 4F setup length becomes 600 mm. The lens was made by EKSMA Optics. The diffraction grating used in this setup was manufactured by Spectrogon (code 715.706.270). Its specifications are shown in Table 3.1.

Pulse shaping experimental approach

An LC-SLM is used with diffraction gratings and plano-convex lenses to design a 4F pulse shaping setup (see Figure 3.7). The 4F setup consists of an LC-SLM placed between a pair of diffraction gratings and plano-convex lenses with a focal length F. The distance between each two components in the setup is equal to the focal length of the plano-convex lens, and the length of the whole setup equals four times the focal length and that is why the setup termed as 4F. A detailed review of the LC-SLM used in this work is provided in section 3.2.1. The first grating

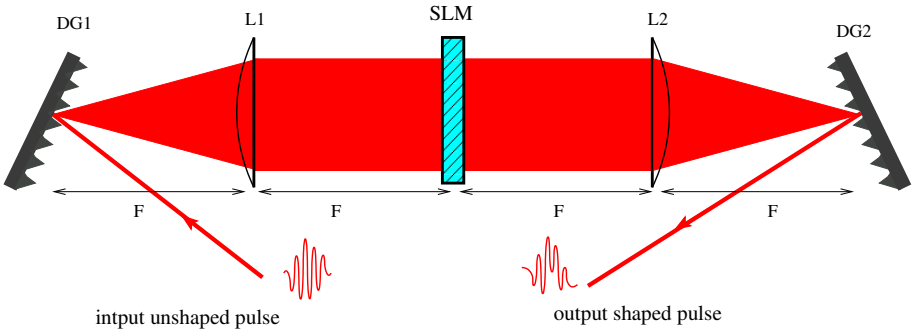

Figure 3.7: Layout of the 4F setup. Key: DG1 and DG2 -diffraction gratings, L1 and L2 plano-convex lenses with a focal length F and SLM-spatial light modulator (own work). The laser beam travels from left to right.

disperses the incoming pulse laser into its frequency components and the first lens collimates the dispersed frequency components in order to allow the pixels of the SLM modulate each spectral component separately. According to the grating equation, the spatial dispersion of the frequency can be calculated as follows:

$$m\lambda = d(\sin(\theta_i) + \sin(\theta_d)), \tag{3.5}$$

where λ is the wavelength of the incident beam, d is the grating groove spacing, θ_i and θ_d are the incident and diffracted angles, respectively. m is the diffraction order of the dispersed light. The convex lens in an important component in the setup as it influences the dispersion of the beam. The widely dispersed beam results in a good shaping. The second lens performs an inverse Fourier transform and the diffraction grating re-combines the ultrashort pulse spectral components into a single collimated beam [87, 90]. Consequently a temporally shaped output pulse is achieved. One advantage of this design is that all optical components are on the same

optical axis. In the case of shaping a pulse in the order of a few tens of femtoseconds, the plano-convex lenses can be replaced by curved mirrors, in order to avoid chromatic aberrations and temporal dispersion [87, 88]. The 4F setup is assumed to be a free dispersion setup, which means that the output laser beam has to be identical to the input beam in the absence of the LC-SLM [86, 88]. The 4F setup allows control of phase and amplitude simultaneously, as well as polarisation and transverse spatial profile [87].

Liquid crystal display of the SLM

In this study the SLM-S640d USB spatial light modulator series manufactured by Jenoptik was used. This series contains two separately controllable liquid crystal displays. Figure 3.8 is a schematic diagram of the side view of the liquid crystal displays of the SLM-S640d USB. These liquid crystal displays are composed of a nematic liquid crystal material sandwiched between a pair of glass plates. Figure 3.9 is a schematic diagram of a single piece of the liquid crystal displays [87, 124]. Each display consists of 640 pixels electrodes each with a width of 97 μm, separated by a gap of 3 μm. The inside surfaces of the glass plates are coated with a thin layer of a transparent conductive material of Indium Tin Oxide (ITO) [124]. The nematic liquid crystal material consists of long, thin rod-like molecules, which afford the material a regular pattern, like a crystalline solid, see Figure 3.10(a). The long axis of the molecules are aligned parallel to the x-axis (parallel to the optical axis) in the absence of the electric field [86]. The ITO layers act as electrodes to align the molecules of the liquid crystal a long to the direction of the applied electric field.

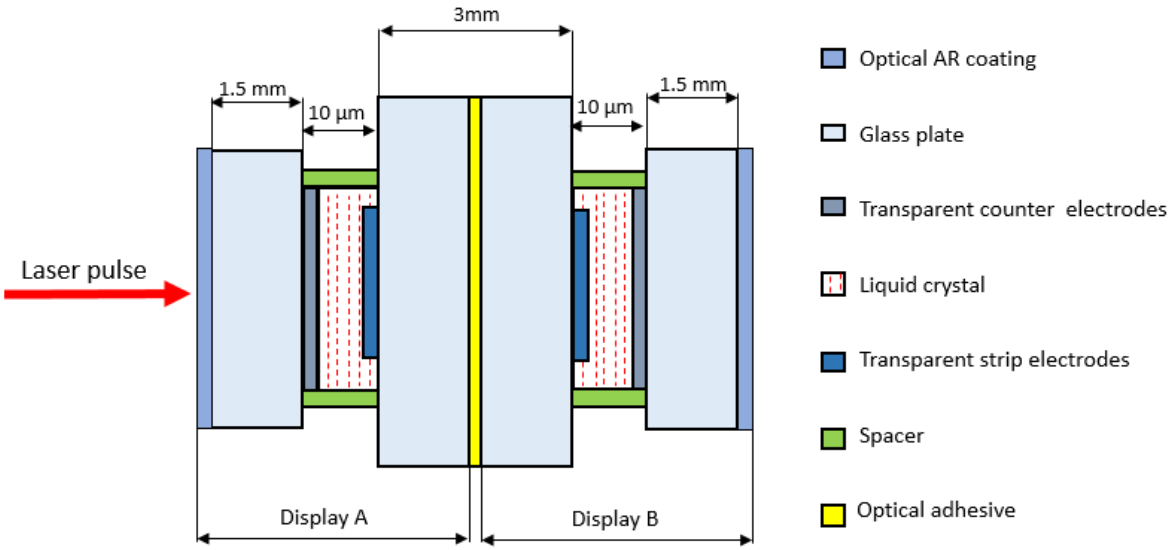

Figure 3.8: Schematic illustration of the side view of the liquid crystal displays of the SLM.

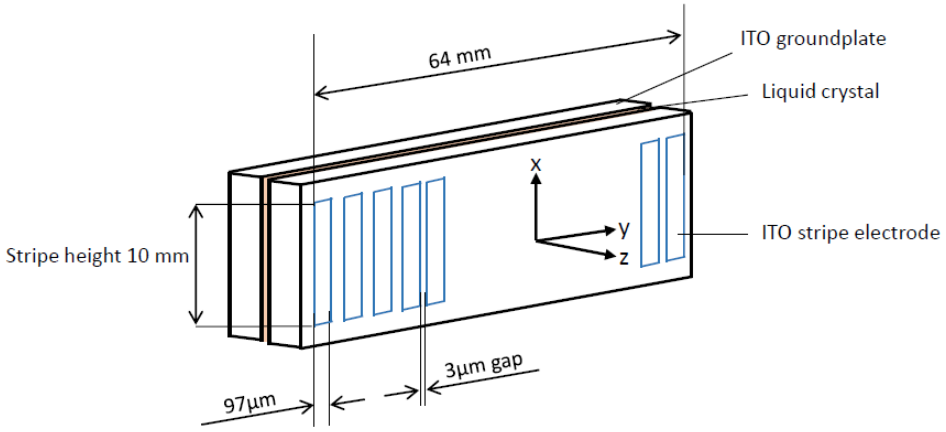

Figure 3.9: Schematic illustration of the stripe electrodes of a single piece of the liquid crystal display.

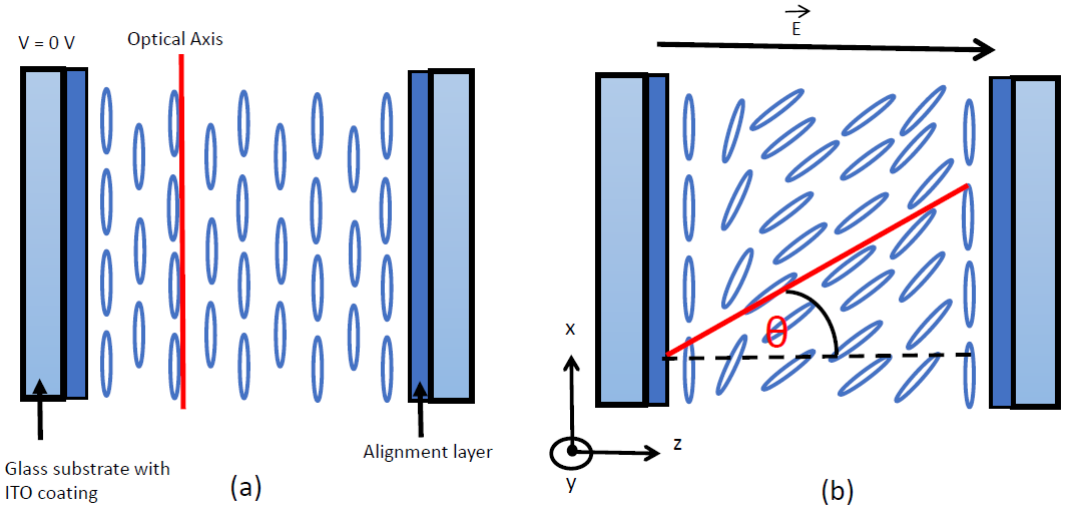

Figure 3.10: Schematic illustration of the liquid crystal display of the SLM; (a) without an electric field and (b) with an electric field applied in the z-direction.

The liquid crystal display acts like a uniaxial birefringent material with its optical axis parallel to the long axis of its molecules. Therefore, when light propagates through the liquid crystal display along the z-axis, it will decompose into two polarisation components. The first component known as an ordinary ray (o-ray) is polarised perpendicular to the optical axis (along the x-axis) encounters a refractive index n_o independent of the orientation of the optical axis. The other component known as an extraordinary ray (the e-ray) is polarised parallel to the optical axis (along the y-axis) encounters a refractive index n_e, which depends on the orientation of the optical axis. The birefringence of the liquid crystal is given as $\Delta n = n_e - n_o$. Consequently, the phase difference between the o-ray and e-ray in the absence of the electric field is given by the

expression

$$\Delta\phi = \quad (n_e - n_o)\frac{d_{LC}}{\lambda_0},$$

where d_{LC} is the thickness of the liquid crystal display and λ_0 is the wavelength of the incident light [124]. When the electrical voltage V, applied in the z direction exceeds the voltage threshold of the liquid crystal, its molecules will tilt in the x-z plane towards the z-axis, as shown in Figure 3.10(b). The optical axis of the liquid crystal will also rotate by an angle θ in the same direction with the molecules. The angle θ has a maximum value when the applied voltage V = 0 V and decreases continuously with increasing the applied voltage, until the liquid crystal display gets saturated when molecules aligned along the z-axis [86]. Consequently, the refractive index n_e value varies by altering the applied voltage, whereas n_o remains constant. This leads to a phase retardation dependent voltage that can now be expressed as

$$\Delta\phi(V) = (n_\theta(V) - n_o)\frac{d_{LC}}{\lambda_0} \quad \text{with} \quad \frac{1}{n_\theta(\omega,V)} = \sqrt{\frac{\cos^2\theta(V)}{n_o^2(\omega)} + \frac{\sin^2\theta(V)}{n_e^2(\omega)}}.$$

The output phase retardation of the e-ray (ϕ_e) comprises the phase retardation that depends on the applied electric field of the liquid crystal ϕ_{LC}, and retardation due to the two glass surfaces of the liquid crystal. Therefore, the total phase retardation can be expressed as

$$\begin{aligned}
\phi_e &= \phi_{LC} + \phi_{glass} \\
\phi_e &= \frac{\omega}{c}\left[n_{LC}(\omega,V)\cdot d_{LC} + 2n_{glass}(\omega)\cdot d_{glass}\right], \\
\text{with} \qquad \Delta n(\omega,V) &= n_{LC}(\omega,V) - n_{o,LC}(\omega) \\
\phi_e &= \frac{\omega}{c}\left[\Delta n(\omega,V)\cdot d_{LC}\right] + \frac{\omega}{c}\left[n_{o,LC}(\omega)\cdot d_{LC} + 2n_{glass}(\omega)\cdot d_{glass}\right] \\
&= \phi(\omega,V) + \phi_{fix}(\omega) \qquad (3.6)
\end{aligned}$$

Equation (3.6) shows that the phase retardation of the e-ray can be described by two terms. The first term, $\phi(\omega,V)$, describes the voltage dependent phase retardation at a specific omega. $\phi(\omega,V)$ has a maximum value when V = 0 V. The second term is constant, for a given ω. The term $\phi(\omega,V)$ is the term that is utilised to manipulate the phase and amplitude of ultrashort laser pulses [124].

3.3 Characterisation of the 4F setup

3.3.1 Modulation of phase and amplitude

The LC-SLM used in this study consists of two liquid crystal displays attached together back-to-back as shown in Figure 3.11. The optical axes of LC display A (LC-A) and LC display B (LC-B) are aligned at 45° and -45°, respectively, relative to the polarisation of the incident light wave, as shown in Figure 3.11. The SLM requires a horizontally polarised light in order to achieve pure phase modulation or pure amplitude modulation or both simultaneously for the ultrashort laser pulses [124]. Using Jones matrices the mathematical description of the electric

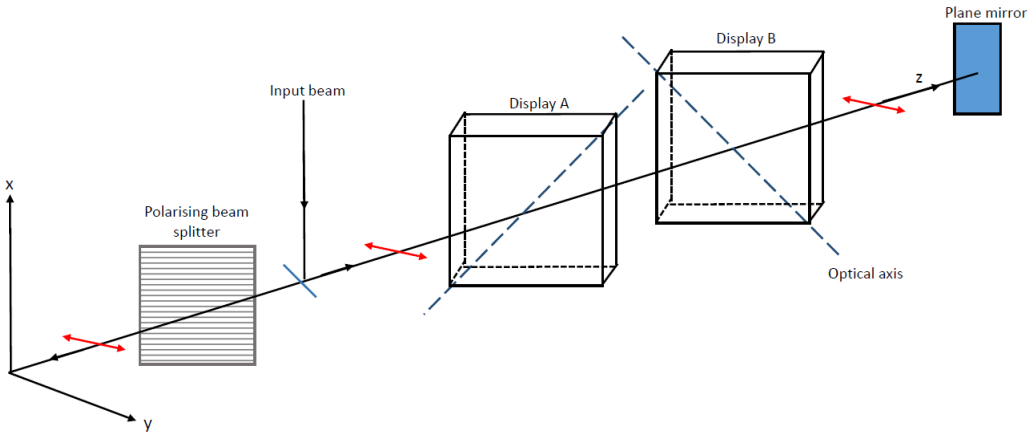

Figure 3.11: Schematic illustration of the optical axes of the liquid crystal displays in the folded geometry 4F setup

field that describes the output radiation for the 4F setup can be given as follows:

$$E_{out} = \overbrace{\begin{bmatrix} 1 & 0 \\ 0 & 0 \end{bmatrix}}^{\text{Polariser}} \cdot \overbrace{\begin{bmatrix} \cos(\theta) & \sin(\theta) \\ -\sin(\theta) & \cos(\theta) \end{bmatrix} \cdot \begin{bmatrix} 1 & 0 \\ 0 & e^{i\Delta\phi_1} \end{bmatrix} \cdot \begin{bmatrix} \cos(-\theta) & \sin(-\theta) \\ -\sin(-\theta) & \cos(-\theta) \end{bmatrix}}^{\text{LCB}}$$
$$\cdot \overbrace{\begin{bmatrix} \cos(-\theta) & \sin(-\theta) \\ -\sin(-\theta) & \cos(-\theta) \end{bmatrix} \cdot \begin{bmatrix} 1 & 0 \\ 0 & e^{i\Delta\phi_2} \end{bmatrix} \cdot \begin{bmatrix} \cos(\theta) & \sin(\theta) \\ -\sin(\theta) & \cos(\theta) \end{bmatrix}}^{\text{LCA}} \cdot E_{in}, \tag{3.7}$$

where $\Delta\phi_1$ and $\Delta\phi_2$ are the relative changes in phase retardations between the e-ray and o-ray polarised components due to the applied voltage on LC-A and LC-B, respectively, and θ is the angle between the optical axes of the liquid crystal displays and the horizontal axis. The term "polariser" is the Jones matrix of the horizontal polariser, placed on the path of the output beam, while the terms "LCB" and "LCA" describe the Jones transformation matrices of LC-B and LC-A, respectively, rotated by an angle θ relative to the horizontal axis [124].

Using the 4F folded geometry (double path setup), which implies the radiation will pass twice through SLM, the polarisation of the radiation reverses due to the retro-reflection. Equation (3.7) is multiplied by the terms LCB and LCA again but using a negative sign for θ for both terms. Consequently, a linearly horizontally polarised incident light wave E_{in} propagates in the z-axis. The mathematical description of the electric field of the output radiation is obtained as follows:

$$E_{out} = \begin{bmatrix} 1 \\ 0 \end{bmatrix} \cdot \cos(\Delta\phi_1 - \Delta\phi_2) \cdot e^{(\Delta\phi_1 + \Delta\phi_2)} \cdot E_0 e^{i(\omega t - kz)}. \tag{3.8}$$

Therefore the amplitude modulation (A) and phase modulation (ϕ) induced by the generated phase retardations by the LC-A and LC-B are given as:

$$A = \cos(\Delta\phi_1 - \Delta\phi_2) \tag{3.9}$$

and

$$\phi = \Delta\phi_1 + \Delta\phi_2, \tag{3.10}$$

with

$$\Delta\phi_1 = \tfrac{1}{2}[\phi + \arccos(A)] \tag{3.11}$$

and

$$\Delta\phi_2 = \tfrac{1}{2}[\phi - \arccos(A)] \tag{3.12}$$

The condition for the pure amplitude modulation is $\Delta\phi_1 = -\Delta\phi_2$, whereas $\Delta\phi_1 = \Delta\phi_2$ is the condition for the pure phase modulation. The phase modulation is determined by the sum of $\Delta\phi_1$ and $\Delta\phi_2$, while amplitude modulation is achieved by the difference between $\Delta\phi_1$ and $\Delta\phi_2$.

3.3.2 Transmission-voltage dependence

Since the voltage dependent transmission $T(V_1,V_2)$ is related to the modulated amplitude square, equation (3.9) is used to investigate the transmission as follows:

$$\begin{aligned} T(V_1,V_2) &= \cos^2(\Delta\phi_1(V_1) - \Delta\phi_2(V_1)) \\ T(V_1,V_2) &= \tfrac{1}{2}[1 + \cos(2\Delta\phi_1(V_1) - 2\Delta\phi_2(V_2))] \end{aligned} \tag{3.13}$$

Hence

$$\Delta\phi_1(V_1) = \Delta\phi_2(V_2^{max}) \pm \tfrac{1}{2}\arccos\left[2T(V_1, V_2^{max}) - 1\right] \tag{3.14}$$

$$\Delta\phi_2(V_2) = \Delta\phi_1(V_1^{max}) \pm \tfrac{1}{2}\arccos\left[2T(V_1^{max}, V_2) - 1\right] \tag{3.15}$$

where V_1 and V_2 are the applied voltages on LC-A and LC-B, respectively. Since there is no direct way to measure the phase, the voltage dependent transmission can be used to obtain the relative phase change, hence it calibrates each liquid crystal display separately. The calibration was achieved by measuring the transmission as a function of the applied voltage for one of the liquid crystal displays while the other was set to be inactive. The liquid crystal display becomes inactive (transmissive only) at the maximum voltage V^{max}, because the angle θ has a minimum value at the maximum voltage, therefore $\Delta\phi_1$ and $\Delta\phi_2$ are approximated to zero.

Using the experimental setup illustrated in Figure 3.12, the liquid crystal displays were calibrated separately. A spectrometer is positioned on the path of the output radiation from the 4F setup for measuring the transmission at a specific wavelength. LC-B is set to maximum voltage while the voltage on LC-A is varied through all 4095 possible drive voltages and the overall transmission is measured. The procedure is repeated for LC-B while LC-A is set to the maximum voltage. Figure 3.13 shows the measured transmitted electric field as a function of the applied voltage for both liquid crystal displays. This result show more oscillations of the transmitted electric field compared to results provided by the supplier of the SLM in [124]. This is because the folded geometry 4F setup in which the pulse passes twice through the SLM was used. Hence this setup allows a broader phase and amplitude modulation than the single path 4F setup.

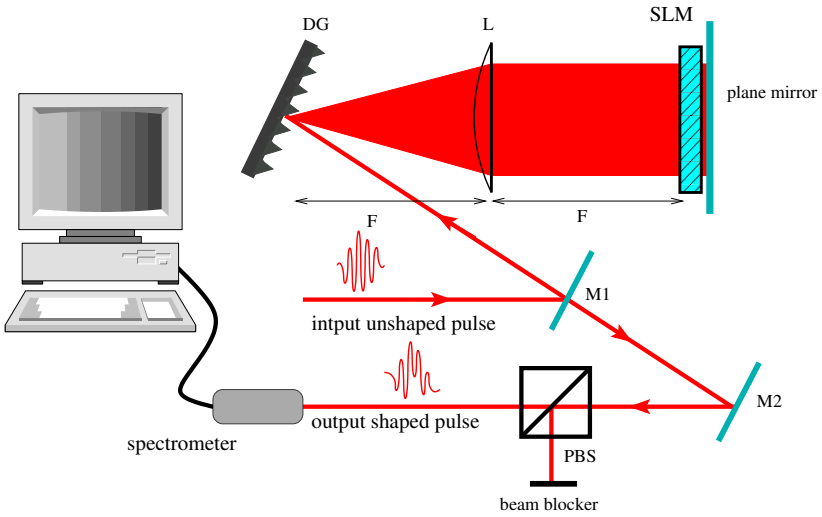

Figure 3.12: 4F setup folded geometry used to calibrate the LC displays of the SLM

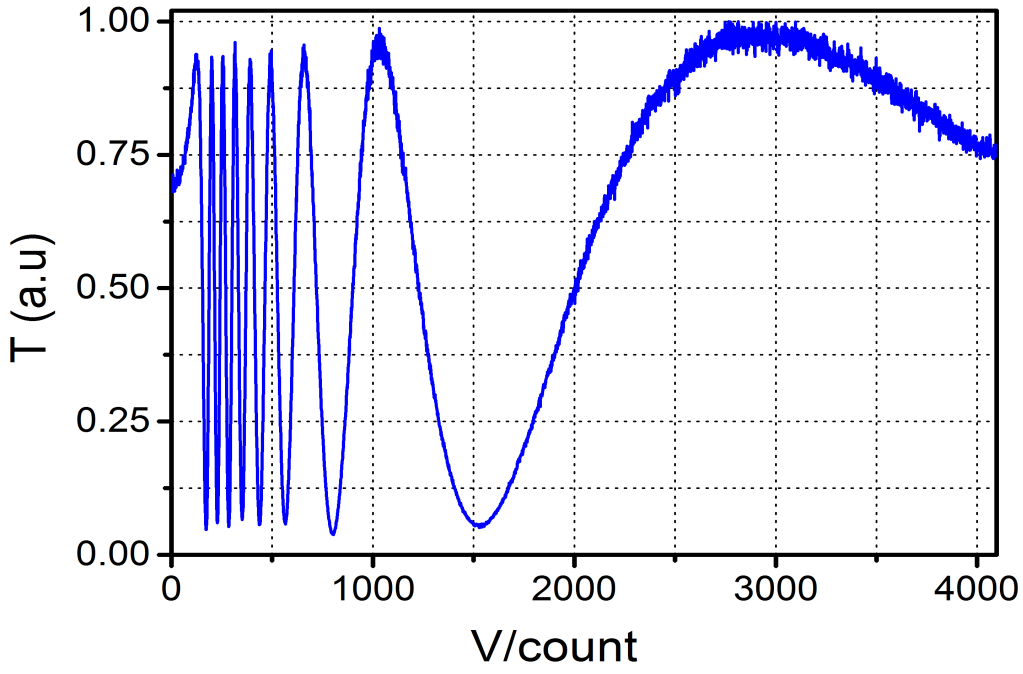

Figure 3.13: Transmission-voltage dependence of the LC-A

3.3.3 Calculation of the phase calibration curve

For the calculation of the relative change in the phase $\Delta\phi(\mathrm{V})$ due to the applied voltage, the measured transmission data were used. For simplification the voltage dependent transmission equation (3.13) can also be written using a sine function instead of a cosine:

$$\mathrm{T(V)} = \quad \sin^2(\Delta\phi(\mathrm{V})). \tag{3.16}$$

Since $\sin^2(\Delta\phi(\mathrm{V}))$ is a periodic function, the equation (3.16) can be written as

$$\mathrm{T(V)} = \quad \mathrm{T_0} \cdot \sin^2(\Delta\phi(\mathrm{V}) \pm \mathrm{k}\pi) \quad \text{where k} = 0,1,2,... \tag{3.17}$$

Therefore

$$\Delta\phi(\mathrm{V}) = \mathrm{k}\pi \pm \arcsin\sqrt{\frac{\mathrm{T}}{\mathrm{T_0}}} \quad \text{where k =0, 1, 2,...} \tag{3.18}$$

In the ideal case, the transmission T(V) reaches the zero at the maximum value of the applied voltage V, and vice versa [124]. T(V) values have to be standardized before applying equation (3.18) in order to calculate $\phi(\mathrm{V})$ as a function of T(V). For standardization the following

equation was used:

$$\frac{\mathrm{T}}{\mathrm{T}_0} = \frac{\mathrm{T_i} - \mathrm{T_{min}}}{\mathrm{T_{max}} - \mathrm{T_{min}}},$$

where $\mathrm{T_i}$ is the transmission corresponding to the ith voltage count and $\mathrm{T_{max}}$ and $\mathrm{T_{min}}$ are the extreme adjacent values to $\mathrm{T_i}$ [124].

$$\Delta\phi(V) = \begin{cases} 2k\pi - 2\arcsin\sqrt{\dfrac{T(V) - T(V_{2k})}{T(V_{2k-1}) - T(V_{2k})}} & \text{for the positive slope} \quad (3.19a) \\ 2k\pi + 2\arcsin\sqrt{\dfrac{T(V) - T(V_{2k})}{T(V_{2k-1}) - T(V_{2k})}} & \text{for the negative slope} \quad (3.19b) \end{cases}$$

For the calculation of the phase retardation $\Delta\phi(\mathrm{V})$, T(V) values that are presented in Figure 3.13 and equation (3.18) are used, and the calculation starts from right to left. For the positive slope, equation (3.19a) is applied, while for the negative slope, equation (3.19b) is applied. The obtained results of the phase retardation-voltage dependence are shown in Figure 3.14. The calibration allows obtaining $\Delta\phi_1(\mathrm{V})$ and $\Delta\phi_2(\mathrm{V})$ for given values of the amplitudes and

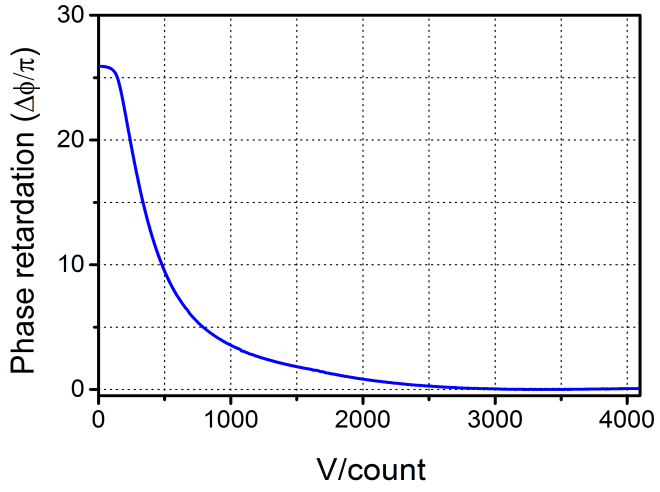

Figure 3.14: Phase retardation as a function of the applied voltage, calculated using equation (3.18) and Figure 3.13.

phases and the corresponding voltage count extracted from the result in Figure 3.14. It shows that the maximum phase retardation value is $26/\pi$ achieved at the low voltage value.

3.3.4 Pixel-spectrum calibration

For the pixel-spectrum calibration the 4F setup presented in Figure 3.12 was used. This calibration indicates the pixel position of each signal wavelength on the LC-SLM. The study is performed by deactivating all pixels of the LC-SLM and allowing only one to be active, while the wavelength that corresponds to this active pixel is detected with a spectrometer. The procedure is done for all pixels starting from the first to the last. The linear relation between the LC-SLM pixels and wavelength obtained from this experiment is shown in Figure 3.15. The resolution of the SLM calculated from the slope of this relation is 0.16 nm/pixel. The central wavelength 506 nm of the beam corresponds to pixel 375.

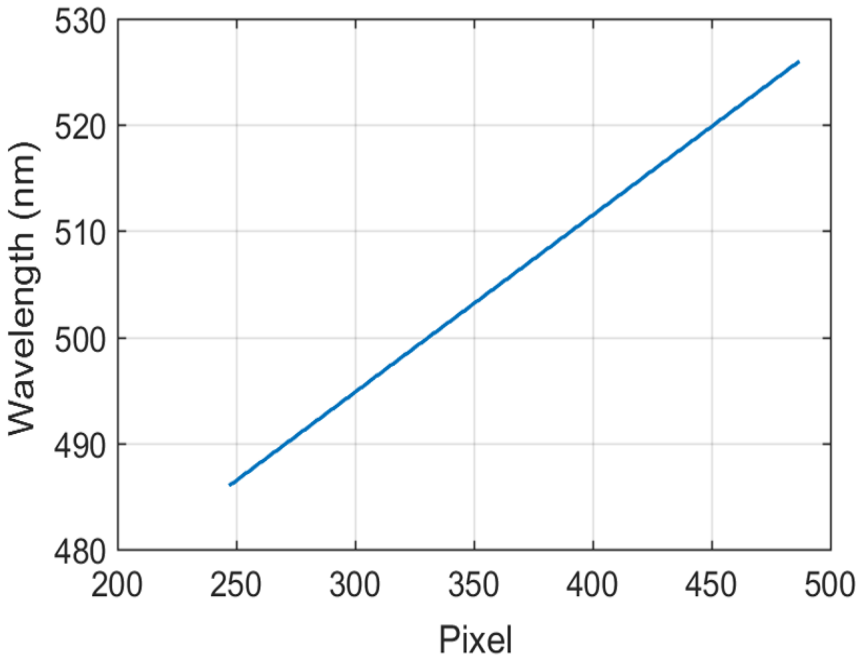

Figure 3.15: Calibration results of LC-SLIM pixels and wavelengths of pump beam in the 4F setup.

3.4 Experimental setup of the FROG

Figure 3.16 is a schematic illustration of our home-built FROG setup. The incoming beam is split into two parts by a beam splitter (BS) with an intensity ratio of 30/70 (reflected/transmitted). The BS is mounted at 45° with respect to the propagation axis of the incoming beam. The reflected beam is sent to a pair of mirrors (M) aligned at 90°, and the transmitted beam is retro-reflected by a mirror (M). This is mounted on a motorised translation stage which can delay this beam by a time Δt. Using a parabolic mirror of 150 mm, the beam is aligned in such a way that it can spatially overlap with itself and be focused in a second harmonic

generation (SHG) crystal to generate second-harmonic signals as a function of Δt, which is a so-called FROG trace. In this setup, a BBO crystal with a size of 6×6 mm^2 and 0.2 mm thickness, cut at $\theta = 44.3°$ and $\Phi = 90°$, is used. The second harmonic FROG signals were measured using the Ocean Optics spectrometer model USB2000. The sensitivity of the FROG setup is 3.3 fs which is determined by the step size of the motorized translation stage (MTS25/M-ZBE from Thorlabs). The FROG software version FROG F-3.2.4 from Femtosoft Technologies was used to analyse the FROG trace data and characterise the ultrashort laser pulses in the time and frequency domains.

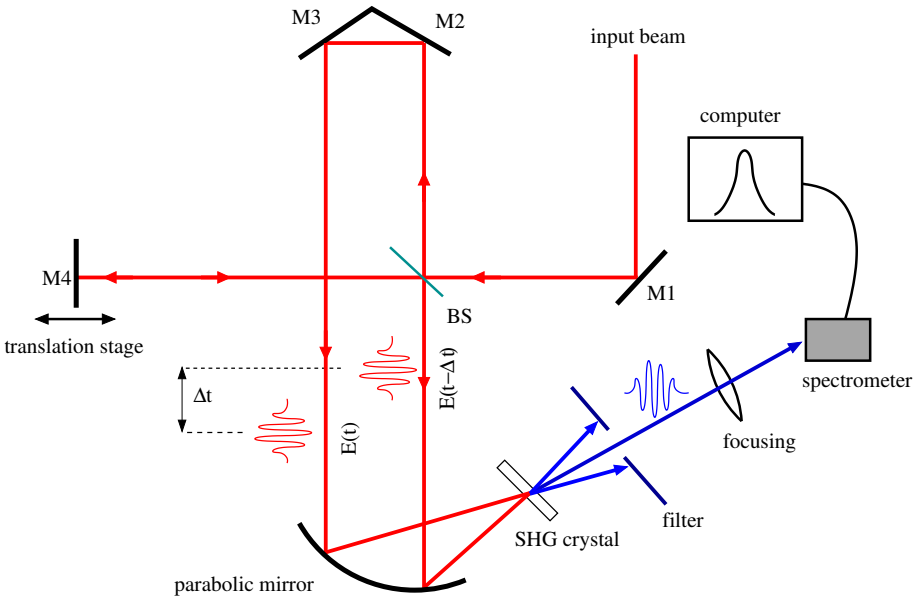

Figure 3.16: Schematic diagram illustrating the optical layout of the home-built FROG setup. Key: BS-beam splitter; M(1-4)-mirrors; and SHG-second harmonic generation crystal

3.5 Genetic Algorithm

Genetic Algorithms (GAs) are adaptive heuristic search and optimization algorithms that are based on the principles of evolution through natural selection and natural genetics [125, 126]. This type of algorithm is usually exploited in an iterative evolution procedure based on the genetic operators of reproduction, crossover, and mutation to optimize an initial population until reaching an appropriate solution to a specific problem [125, 127, 128]. In every search or optimization procedure, the reproduced population (called generation) is expected to produce a better candidate solution to the problem under investigation than the previous generation. Every generation in GA consists of individual proposals to a solution of the problem at hand (called individuals or chromosomes), and in every search procedure the fitnesses of all individuals are evaluated to determine the solution's quality. The fitness of an individual is defined

as the value of an objective function in the optimization problem being solved. Individuals can encode parameters in different forms, such as binary or real number representations of candidate solutions [126]. The most common representation of solutions by individuals is that of binary number encoding, because this representation allows easy decoding and evolution (i.e., the genetic operators act naturally in the basis of binary-number representation) [126]. The best way to understand the working of a genetic algorithm is to examine how the genetic operators act on a population. The reproduction operator acts by selecting some individuals, based on a ranking of their fitnesses, for that will be used for the production of a next generation. The crossover operator produces a pair of offspring by combining genetic material (i.e., parts of a binary number encoding) from multiple (typically two) parents from the previous generation. Both parent selection and crossover exchange are performed with some randomness. The mutation operator mutates these offspring individually by inverting the value of some of their bits randomly [127].

GAs have been used as a search and optimization tool to find the solution of problems in various fields including sciences, engineering and commerce. They have also been used as an analysis tool for the nuclear magnetic resonance data of DNA in order to predict the correct protein instruction of the DNA [127]. Usually, in coherent control experiments, the GA iteratively optimizes the shape of the laser pulse that is being used to optimize certain molecular dynamics. Thereafter, the optimal laser pulse shapes are investigated and related to the actual molecular dynamic in order to understand its underlying mechanisms. In this study, a home-developed GA code [123] was used. Figure 3.17 illustrates the important parts of the GA algorithm that was used in our coherent control experiment. These phases can be explained as follows:

1- *Initial population:* in this phase, an initial population (generation) consists of N number of individuals (candidate solutions) are generated randomly. Initial conditions were given to ensure that some results will be obtained.

2- *Measurement:* an initial measurement (transient absorption spectrum) is performed using the initial population. The measurement parameters can be an amplitude at a selected point in a spectrum, power or other characteristics of the optimization problem.

3- *Fitness evaluation:* in this phase, the fitness value (quality of the solution) of all individuals in the current population is calculated and evaluated according to the defined objective function.

4- *Reproduction:* in this phase, a particular number of individuals are selected according to their fitness values to form the parent population that will be used for offspring (children) generation. This means that individuals with a higher fitness value are kept in the population and more copies of them are made, while individuals with lower fitness values are eliminated and replaced with the copies of those ones that have higher fitness values. The

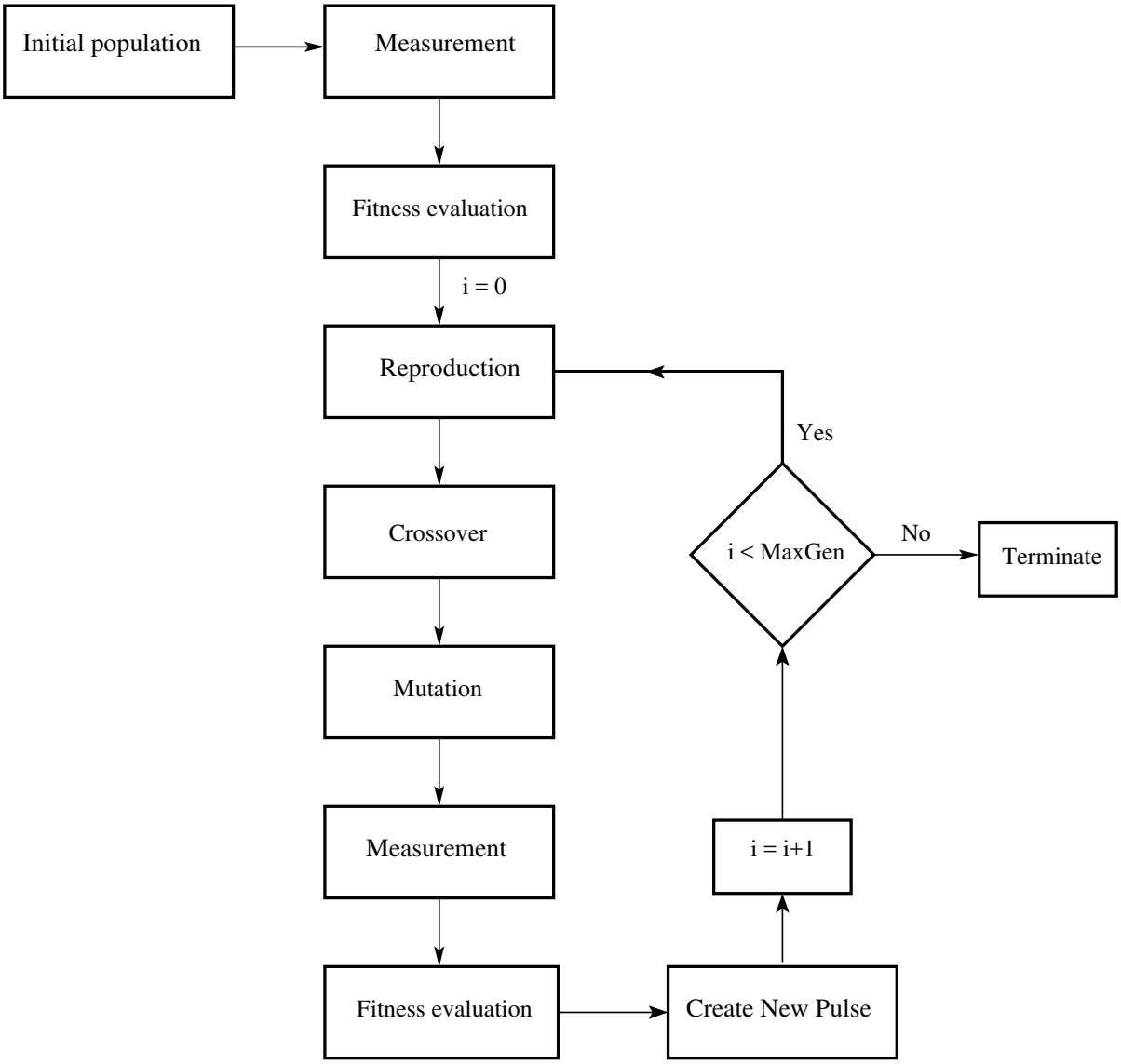

Figure 3.17: Block diagram of the genetic algorithm procedure

number of individuals in the population does not change after the reproduction process; it remains the same as the number in the initial population.

5- *Crossover:* in this phase, pairs of the reproduced string (parents population) are selected randomly and mated together to create two new offspring. Since the parents' string is presented in a binary approach, the mating is done by selecting a crosspoint along the strings from a uniformly random distribution. The characters beyond the chosen point in the first string are then swapped with the characters beyond the same point in the second string.

6- *Mutation:* in this phase, the operator introduces random alterations into the offspring string. It randomly selects one bit (0 or 1) from the offspring string and changes it to 1

if it had a value of 0, or vice versa. Figure 3.18 shows the change that occurs during the crossover and mutation phases.

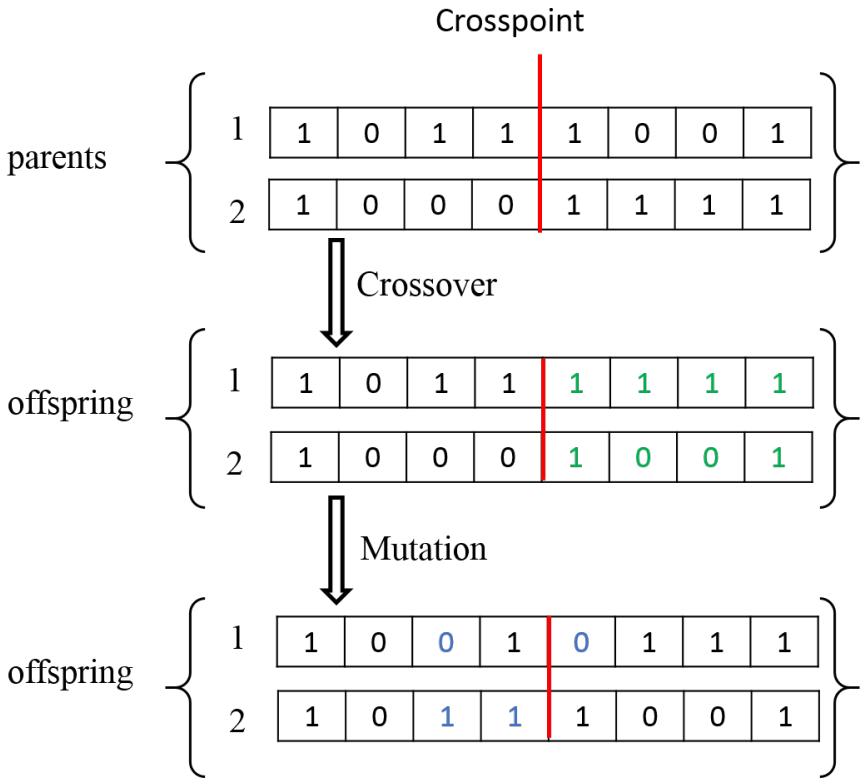

Figure 3.18: Illustration of the crossover and mutation genetic operator procedures. The red line indicates the location of the cross point after which bits are exchanged between the two strings in the crossover operator as indicated by the green colored bits. The mutation is illustrated by the blue colored bits.

7- *Measurement:* in this phase, an experimental measurement is performed using the parameters of each individual of every new generation.

8- *Fitness evaluation:* in this phase, the fitness values of the individuals of every new generation are evaluated.

9- *Create new pulse:* in this phase, the parent population is totally or partially replaced by the offspring population.

10- *Termination:* Steps 4 up to 9 are repeated until the GA terminates, either when the maximum number of generation is produced (MAXGen), or a satisfactory convergence is achieved. In our work, we terminated the iteration when MAXGen reached 58.

3.6 Visualization of the GA individuals in a joint time-frequency basis

The electric field that describes the laser pulse can be visualized as a one-dimensional function in the frequency (spectral) or time (temporal) domain. Both are related by a Fourier Transform as introduced previously in section 2.1. Therefore, when the laser pulse interacts with matter, the resultant effect of the interaction can be well understood in either domain, knowing that moving from one of the domains to the other does not lead to any loss of information. However, using these types of representation, some features of the pulse are obscured [129], and can only appear when the pulse is visualized in both domains simultaneously. For example, when using ultrashort laser pulse shaping devices (Dazzler and SLM), the spectral and temporal representation functions have to be visualized in a two-dimensional joint time-frequency (JTF) function in order to manipulate the related features in both domains simultaneously. These ultrashort laser pulse shaping devices usually transmit the effect of functions that are applied on them to an input pulse. These devices can only operate on a numerical two-dimensional representation function, because they are pixelated. Therefore, several JTF representations of the electric field of the laser pulse have been introduced such as the Husimi-Wigner [130] and Von Neumann [129, 131] representations.

In this study, the Von Neumann representation method is used, because it provides a one-to-one mapping from either time or frequency representation to the JTF representation of electric field of a pulse. Moreover, it visualizes the electric field of a pulse by using a discrete function in the phase-space lattice of nonorthogonal Gaussians as a basis [129]. In the Husimi and Wigner representations, the electric field of a pulse is presented as a continuous function in JTF space. The conversion of an electric field signal from a frequency or time domain representation to the two-dimensional joint time-frequency representation in the Von Neumann lattice, is explained in more detail in references [129, 131]. Implementation of the JTF representation in our coherent control experiment is described in the thesis of Dr. A. J. Hendriks [123].

3.7 Pump-probe setups of LaserLaB Amsterdam

Femtosecond transient absorption (TA) spectroscopy on the FCPb complexes incorporated into liposomes (plFCPb) and FCPb aggregates (qFCPb) was conducted with a pump-probe setup described in ref. [97], while annihilation studies on the solubilized FCPb (sFCPb) were performed on a setup described in ref. [29]. The main difference between the two setups is the laser source.

The first setup [97] uses 80 fs laser pulses at a wavelength of 800 nm, obtained from a Ti:sapphire oscillator-regenerative amplifier (Coherent Mira seed and RegA) operating at a 40

kHz repetition rate. The amplified light at 800 nm was split into two parts. One part was used to drive a double-pass optical parametric amplifier (OPA) setup to generate the excitation beam at the desired wavelength. After the OPA setup the excitation beam was sent through a delay-line of 80 cm (≈5 ns) length and a minimal step size of 0.1 μm (≈0.5 fs), thereafter was focused to a spot size of 130-200 μm at the sample position. The excitation beam was blocked after passing through the sample. For the probe beam in this setup, the other part of the amplified light at 800 nm was focused on a sapphire plate to generate the white light continuum, which is then focused on the sample to a spot size smaller than the excitation beam, and spatially overlapped with the excitation beam. The probe beam was collimated and directed to a spectrograph that spectrally disperses and projects the light on a silicon diode array that consists of 76 diodes and read by a computer. In order to measure the probe beam when the sample is excited (pump-on) and not excited (pumped-off), the excitation beam was sent to pass through a mechanical chopper whose frequency was synchronized with the repetition rate of the laser.

The second setup [29] is driven by an ultrashort 50 fs laser pulse at wavelength of 800 nm at a 1 kHz repetition rate, generated also from a Ti:sapphire oscillator (Coherent Mira seed) and amplified with a kilohertz amplifying system (Alpha-1000 US, B.M.Industries). In this setup, the probe beam was also generated and detected in a similar way to the first setup. However, the excitation light was generated by a single-pass OPA setup. In this setup, the probe beam was sent to a similar delay-line as in the first setup.

3.8 Appendix: Supplementary information

Table 3.1: Diffraction grating details

Specification	Value
Groove density	1800 grooves/mm
Size	64$\times$ 64 mm
Thickness	10 mm
Optical range	500-700 nm
Polarisation type	horizontal polarisation

Chapter 4

Laser coherent control of excitation energy flow in the LHCII complex

4.1 Abstract

Laser coherent control experiments have been widely used to direct the outcome of photoreactions to a desired path in order to further investigate specific reactions. In this study, we were able to adapt a transient absorption pump-probe experiment to a laser coherent control experiment. We have successfully managed to perform a laser coherent control experiment that controls excitation energy flow from the S_2 state of carotenoids to the chlorophylls in LHCII using a shaped pulse train. The yield of the energy transfer channel was optimized over the internal conversion channel through the temporal manipulation of the amplitude and phase of the excitation pulse shape using a blind phase function in a spatial light modulator. The optimization curve of the optimal pulse shape was enhanced by 24% compared with the initial pulse shape. The optimal pulse exhibited a shape that consists of 7 sub-pulses with a separation time of 178 fs between every two consecutive sub-pulses, and a FWHM of 92 fs for each sub-pulse. The main mechanism that is responsible for the optimization was attributed to the enhancement of vibrational modes via impulsive stimulated Raman scattering in order to facilitate energy transfer. Optimization of incoherent processes such as annihilation and saturation can be excluded due to the low excitation density that was induced by the pump pulse and low excitation energy that was used in this study.

4.2 Introduction

The light-harvesting process is the primary step in photosynthesis, and is performed by the light-harvesting complexes of photosynthetic organisms. The main light-harvesting complex

(LHCII) of photosystem II in higher plants and green algae is the most abundant membrane protein on land [10]. In LHCII, absorption of the solar energy is accomplished by chlorophyll (Chl) and carotenoid pigments, and the excitation energy is then funneled to the reaction center (RC) through a series of transfers amongst the pigments [7]. In addition to the light harvesting and excitation energy transfer functions, the LHCII complex plays an important role in the photoprotective mechanism of the photosystems against damage under high-light conditions, by dissipating excess excitation energy [6, 31].

LHCII complexes naturally exist in the form of trimers, as was determined using X-ray diffraction crystallography at a resolution of 2.5-2.7 Å [6, 11, 30]. Each trimer is composed of three nearly identical subunits (monomers), each of which contains of 14 Chls (8 Chls-a and 6 Chls-b) and 4 carotenoids (2 luteins, 1 neoxanthin, and 1 violaxanthin) [6, 10–13, 29, 30]. The monomer protein structure is formed by 3 transmembrane α-helices and 1-2 short amphipathic helices [6, 11–13].

The Chl pigments absorb light in almost the entire visible region and predominantly in the red and blue regions with the most dominant peaks located at around 675 nm and in the blue around 470 nm, respectively. The carotenoid pigments absorb light only in the blue-green region that corresponds to the transition from the ground state energy level to the second singlet excited state, i.e., $S_0 \longrightarrow S_2$ [28,29]. The transition $S_0 \longrightarrow S_1$ is forbidden due to the inversion symmetry between the two states [26–29]. The lifetime of the second singlet excited state S_2 is very short (between 100 and 500 fs) and in LHCII 60–65% of the excitation energy of this state is transferred to Chl pigments (mainly Chl-a), whereas the remaining 40–35% of the excitation energy decays to the first singlet excited state S_1 via internal conversion (IC) [28,29,132,133]. Besides the light absorption function, carotenoids play an important role in the major photoprotection mechanisms, by which Chl fluorescence is quenched in order to prevent the formation of singlet excited state oxygen, which is a reactive product that can cause damage to the photosynthetic apparatus [20, 23, 51]. Carotenoid triplet excited states can also neutralize the singlet excited state oxygen directly [22]. Furthermore, carotenoids are involved in the regulation of thermal energy dissipation in antenna systems in the presence of high illumination intensity through the xanthophyll cycle [24, 25], in which violaxanthin carotenoids convert to zeaxanthin in LHCII.

Due to their high absorption capacity of light in the blue-green region and transfer of the excitation energy to other pigments, carotenoids have been used in artificial photo- synthetic antenna systems, to improve their sunlight harvesting efficiency [134–136]. The excitation energy transfer (ET) process from the donor carotenoid pigments to acceptor pigments such as Chls and porphyrins is one of the critical factors that determine the efficiency of both natural and artificial light-harvesting systems. However, the ET efficiency is negatively affected by other competing ultrafast processes such as IC [68, 137]. Therefore, an understanding the mechanism of the energy flow process in the natural light-harvesting systems will also add a significant contribution to the development of efficient artificial antenna systems. Laser coherent control

has been a powerful technique to study and understand various ultrafast molecular dynamics using femtosecond pulse shaping in a learning loop [102]. The optimal pulse that leads to the best control (as found by the learning loop) is then analyzed and related to the processes that are controlled in order to understand the underlying mechanisms. This technique has been successfully used to control the population transfer [65] and excitation ET in natural and artificial LHCs [67, 116] and isomerization of the retinal molecule in bacteriorhodopsin [66, 69].
Our aim in this study is to develop an experimental protocol to control the ultrafast energy flow pathways from the S_2 state of carotenoids selectively excited at 506 nm in the LHCII complex. The results show that we have successfully optimized the ET channel over the IC channel in carotenoids in the LHCII complex, and the optimal pulse shape was characterized and related to the ET and IC processes.

4.3 Materials and spectroscopic methods

4.3.1 Sample

LHCII trimers used in this study were extracted from spinach leaves by Dr. Erica Belgio from the Czech Academy of Sciences, using the protocols described in [138]. LHCII complexes were obtained with an optical density (OD) of 16 at the maximum Chl-a Q_y absorption. The protocol specified the use of a detergent-buffer mixture containing 20 mM HEPES buffer (pH 7.5), and 0.03% of a weight/volume (w/v) beta-Dodecyl-maltoside (β-DM) detergent. The sample was diluted to a final concentration of OD 4.2 and was placed in a cuvette with an optical path length of 1 mm. The cuvette was mounted on a mechanical shaker in order to limit sample degradation due to multiple consecutive pulses.

4.3.2 Measuring of the steady state absorption spectrum

Steady state absorption spectrum of the solubilized LHCII trimers was recorded between 400 nm and 740 nm at room temperature using a CARY-100 Bio UV-Vis spectrophotometer. To check for sample stability, spectra of LHCII were measured before and after the experiment.

4.3.3 Measuring of a transient absorption spectrum

In the laser coherent control experiment, the transient absorption spectra related to each shaped pulse were used as a feedback signal in the Genetic Algorithm (GA) for the optimization process. Transient absorption spectra of solubilized LHCII trimers were obtained using pump-probe spectroscopy. The sample was excited with a shaped pump pulse at a wavelength of

506 nm, and energy of 700 nJ/pulse, which corresponds to a fluence of 1×10^{15} photons/cm^2 per pulse, and the transient absorption spectra were subsequently collected using an unshaped probe pulse. The spot size of the pump beam at the sample position was 200 μm. The transient absorption spectra were collected at a fixed time of 300 fs after excitation because the excited state absorption (ESA) signal has a maximum amplitude at this delay time as shown in previous studies [29, 139]. The pump beam pulse has a duration of 130 fs and was measured with a home-built FROG device. The utilized pumping wavelength, mainly excites the lutein and violaxanthin carotenoid pigments, which transfer their excitation energy from the S_2 state preferentially to Chl-a [29, 132, 139].

4.3.4 Closed-loop control protocol

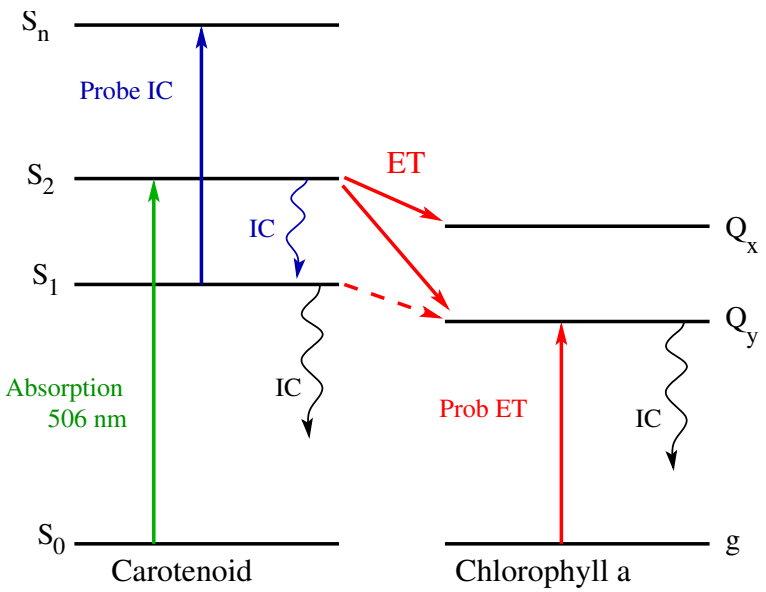

Figure 4.1: Schematic diagram showing the decay of the S_2 state of carotenoids in LHCII. The green upward arrow indicates absorption, while blue and black wavy arrows present the relatively fast and slow IC decay pathways, respectively. Red solid and dashed sloping arrows indicate ET pathways from the S_2 and S_1 states to the Q_x and Q_y states of Chl-a. Blue and red upward arrows represent the two probe channels that can be controlled with the laser coherent control experiment

Figure 4.1 shows a simple model that describes the energy flow pathways from the carotenoid S_2 state. The model was made according to results from previous transient absorption spectroscopy studies of S_2 energy flow pathways in carotenoids after excitation at 506 nm [29, 132, 139]. According to these studies, the carotenoid S_2 state has a lifetime of few hundred femtoseconds (100-500 fs). In the transient absorption spectrum of LHCII trimers, the ET process from carotenoids to Chl-a pigments is resolved as a negative signal at 675 nm, which is attributed to the ground state bleach of Chl-a pigments. The IC process is resolved as a broad positive signal peaking at 540 nm, which is attributed to the excited state absorption of

carotenoids from S1 to higher levels. The IC decay process from the S_1 and Q_y states occurs at a timescale that is long compared to IC from S_2 to S_1, because of the relatively long lifetimes of the S_1 and Q_y states (about 20 ps) [29, 139]. The red dashed sloping arrow indicates the relatively slow ET process from the S_1 to Q_y state, which has a characteristic time of 1 ps [29, 139]. For the optimization process in the laser coherent control experiment, a closed-

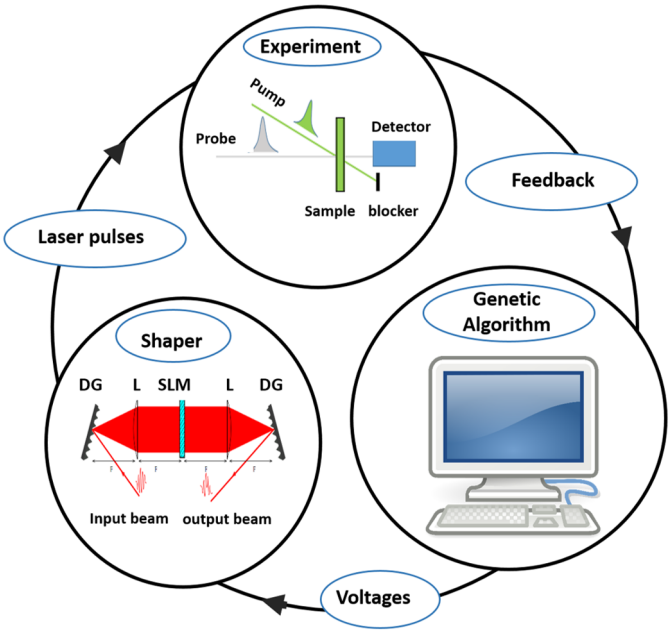

Figure 4.2: Block diagram describes the three main parts of the optimization closed-loop that was used in the laser control of the energy flow pathways of LHCII.

loop optimization strategy was used [102, 115] (see Figure 4.2). The loop consists of three basic elements: the pump-probe experiment, the genetic algorithm (described in Section 3.5) in which the fitness of individuals was calculated and the optimization was performed, and the shaper, through which new pulse shapes were generated. The experiment was initiated by a randomly produced generation, that consisted of a set of 60 individuals (pulses) using a blind phase function for the phase and amplitude modulation. For the initial generation production, initial conditions were given to ensure that some results will be obtained. An experimental feedback signal was then sent to the GA code in order to calculate the fitness values of the 60 individuals using the defined target function. In this study, the transient absorption spectra were used as a feedback signal to the GA where fitness values were obtained using the ratio A_{ET}/A_{IC} as a target function for every individual. A_{ET} is the absolute value of the GSB amplitude at 675 nm and A_{IC} is the ESA amplitude at 540 nm. After evaluating the fitness of the first generation the GA supplied the shaper with a new set of voltages to produce a new generation that also consisted of 60 individuals. This new generation is expected to provide better fitness values than the previous generation. This optimization process was programmed to run for 16 hours (for fifty-eight generations). The NLC-CSIR (where the laser facility is located) does not allow

running of experiments without a researcher being present. Although the optimization result could have been improved if the experiment was allowed to run for a longer time, we expect such potential improvement to be marginal, since noise and drift in the laser system and the sample response become significant after about 12 hours and efficient optimization is therefore impeded. The duration of the transform-limited pulse of the pump beam used in this study is 130 fs (see Figures 4.3) measured using the FROG device.

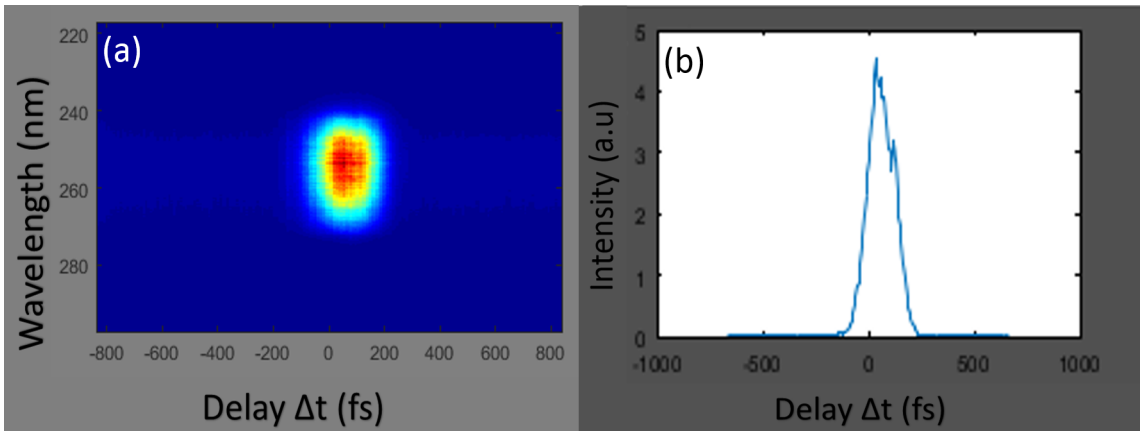

Figure 4.3: (a) experimental SHG-FROG traces and (b) intensity autocorrelation of the pump beam at λ = 506 nm

4.4 Results

4.4.1 Steady state absorption spectrum

Figure 4.4 shows the room temperature steady state absorption spectrum of the trimeric LHCII sample that was used for our laser coherent control experiment. Absorption peaks at 675 nm, 600 nm and 437 nm correspond to the Q_y, Q_x, and Soret absorption bands of Chl-a, respectively. The Q_y and Soret absorption bands of Chl-b peak at 650 nm and 471 nm, respectively. The shoulders at 414 nm and 484 nm correspond to absorption due to the $S_0 \longrightarrow S_2$ transition in the carotenoids. These results are in good agreement with previously measured absorption spectra of LHCII trimers [10, 23, 29, 139].

4.4.2 Transient absorption spectrum

The transient absorption spectrum of the LHCII trimers obtained with every individual solution was used in the laser coherent control experiment to calculate the fitness value of the individual. Figure 4.5 presents the transient absorption spectrum obtained with the first individual. The spectrum exhibits two intense negative bands with an additional small band peaking at $\sim$

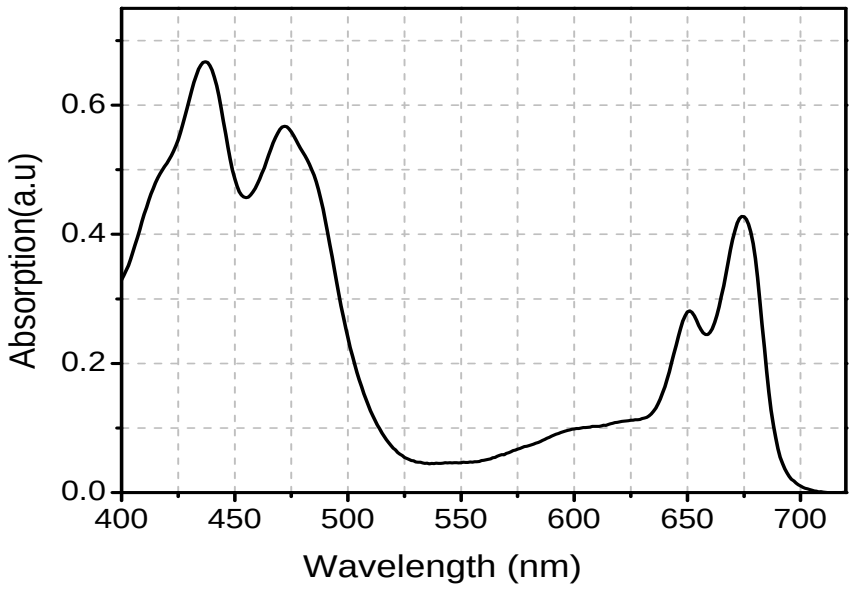

Figure 4.4: Steady state absorption spectrum of solubilized LHCII trimers recorded from 400 nm to 720 nm at room temperature using a CARY-100 Bio UV-Vis spectrophotometer.

640 nm. The first band, appearing $<$ 500 nm is mainly attributed to ground state bleaching and stimulated emission (GSB/SE) of the carotenoid pigments which occur immediately after photoexcitation. However, this main GSB/SE band also contains $\sim$ 10% GSB/SE of Chl-b that is directly excited with the pump beam. Since Chl-b transfers all its excitation energy to Chl-a, this amount of excited Chl-b does not affect the laser coherent control results. Moreover, the influence of the shaped pump pulse on ET from carotenoids to Chl-a is monitored at the carotenoid ESA band. The other negative band peaking at 674 nm is attributed to the GSB/SE of Chl-a pigments, which occurs due to the ultrafast ET process from the initially excited carotenoids to Chl-a pigments. The small negative band peaking at $\sim$ 640 nm is attributed to GSB/SE of Chl-b, which results from the ultrafast ET from the initially excited carotenoids to Chl-b. The excited Chl-b at $\sim$ 640 nm also transfers its excitation energy to Chl-a within few hundred femtoseconds. However, the GSB/SE amplitude of Chl-b at $\sim$ 640 nm is relatively small (5 % compared with that of carotenoid at $\sim$ 500 nm), indicating that the ET from Chl-b to Chl-a is relatively small compared with the transfer from carotenoid to Chl-a, which leads to a negligible effect on the coherent control results. The positive signal peaking at 540 nm is attributed to ESA of carotenoids, which occurs primarily due to absorption of the probe light by carotenoids in S_1 after decay from S_2. The GSB/SE and ESA signals resolved in this spectrum are similar to those resolved in previous studies [29, 139]. The amplitudes of the GSB/SE and ESA signals were used to optimise the ET channel in the laser coherent control experiments.

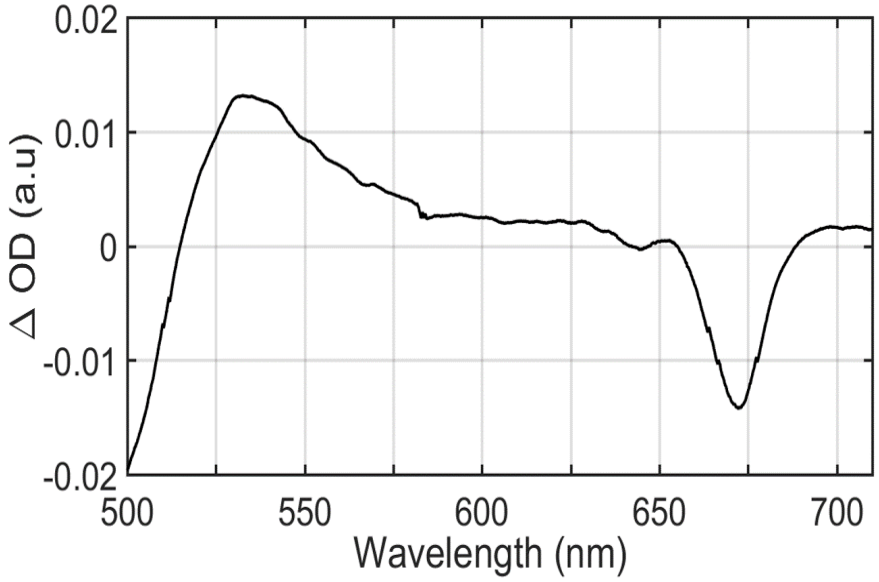

Figure 4.5: Transient absorption spectrum of solubilized LHCII trimers measured at 300 fs delay time upon excitation at 506 nm for the initial generation. This spectrum is an average over 500 pump-probe spectra.

4.4.3 Results of the coherent control experiments on LHCII

In this study, we performed both phase and amplitude modulation of the excitation pulse in order to optimise the ET channel over the IC channel. Due to the complexity of LHCII, the optimization process requires a large search space to achieve sufficient optimization. In this study, the large search space was achieved by allowing GA to produce 58 generations each consisting of 60 individuals, and using a blind optimization method. In the blind optimization method, the experiment is initiated with a set of random phase patterns generated by the pulse shaper, which are then tested on the sample. After testing a random phase pattern on the sample, the feedback signal is fed into a GA that calculates and evaluates the fitness of the particular phase pattern, compared to a defined target function (A_{ET}/A_{IC}), in order to perform the optimization procedure. The blind optimization method has been used as an initial optimization step to find the initial optimal pulse shape and estimate the initial phase function; which are then used as starting parameters in a second optimization step, that can be restricted to a specific class of pulses [67, 68].

Figure 4.6 presents the optimization curve of fitness values (given by the ET/IC ratio) of the generations. Each generation's fitness value is the average of fitness values of the 60 individuals in the generation. The fitness optimization curve (Figure 4.6) shows that an enhancement value of 24% obtained by generation 56 compared to the initial generation fitness value. By dividing the enhancement value by 58 (total number of generations) we obtained an enhancement of 0.4% per generation. In the optimization procedure, some generations can be classified as outliers that were caused by laser instabilities. The initial generation, made up of 60 individuals,

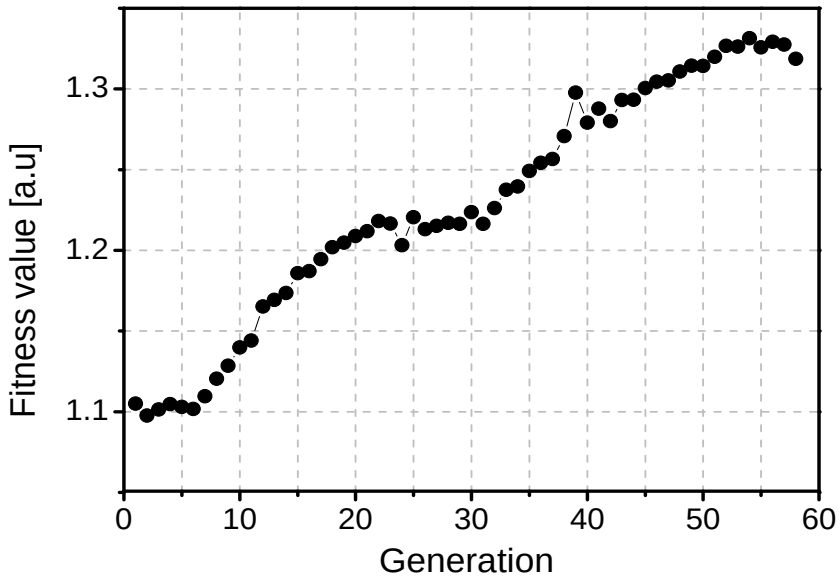

Figure 4.6: Optimization curve of fitness values of the ET/IC ratio, which is obtained using the ratio A_{ET}/A_{IC}, where A_{ET} is the absolute value of the GSB amplitude at 675 nm and A_{IC} is the ESA amplitude at 540 nm. The curve shows that an optimization of 24% compared to the initial fitness value is achieved.

was produced randomly. In each new generation the 10 individuals with the best fitness values were duplicated, and replaced the 10 worst values. Due to the initial randomness the improvement of the first few new generations is slow, which can be seen as an initially flat slope. The optimization curve exhibits a flat feature toward the end of the curve, and for the last generation the fitness decreased, which might be due to laser instabilities or the optimum convergence of the curve was not achieved.

In this study, we were not able to compress the pump pulse after the NOPA setup because the compressor setup reduced our pump beam power significantly. Moreover, the experiment was allowed to run for only 58 generations. Therefore, only a preliminary conclusion to this study is provided. In the future, after optimizing the coherent control setup including compressing the pump pulse after NOPA, the experiment should be run for more iterations until the optimal convergence is achieved. The experiment should be initiated with a Gaussian pulse shape, in order to compare the fitness of the optimal pulse with the initial Gaussian pulse shape.

For characterizing the temporal and spectral profiles of the optimal pulse, a home-built FROG setup was used. Figure 4.7 shows the temporal profile of the optimal pulse of generation 56 that provided the best fitness value of all the generations. The autocorrelation of the optimal pulse (Figure 4.7(a)) shows that the optimal pulse was stretched into 1.2 - 1.3 ps, and that it contained a train of 7 pulses with a periodic time of about 178 fs, and the full width at half maximum (FWHM) of each sub-pulse was about 91 fs. An oscillation frequency of 187 cm^{-1} (5.6 THz) together with an additional frequency component of 83 cm^{-1} (2.5 THz) were obtained by calculating the fast Fourier transform (FFT) of the intensity temporal profile (Figure 4.7 inset).

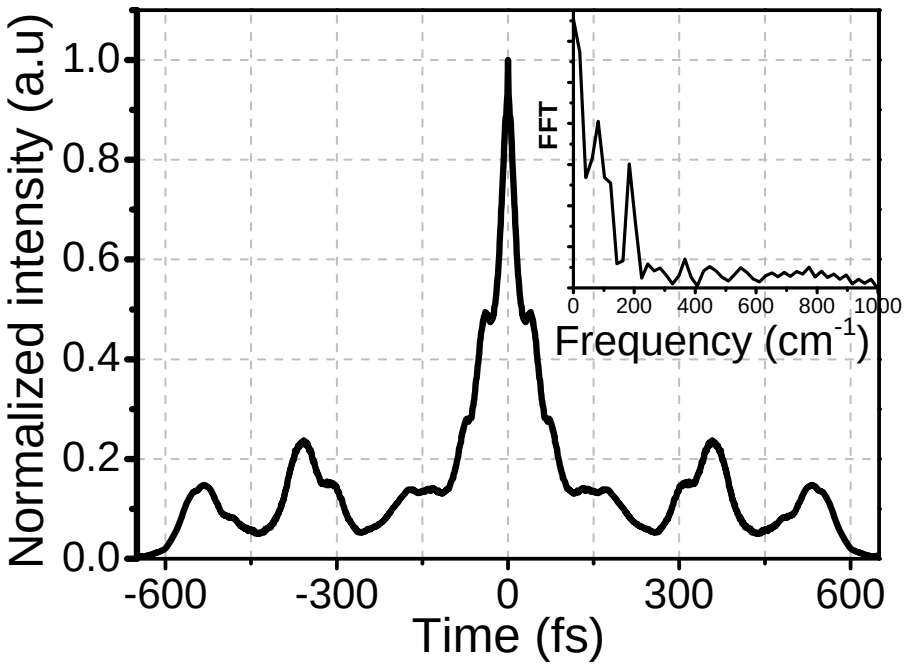

Figure 4.7: Temporal intensity profile of the optimal pulse measured with the home-built FROG setup. Inset Figure presents the corresponding fast Fourier transform (FFT).

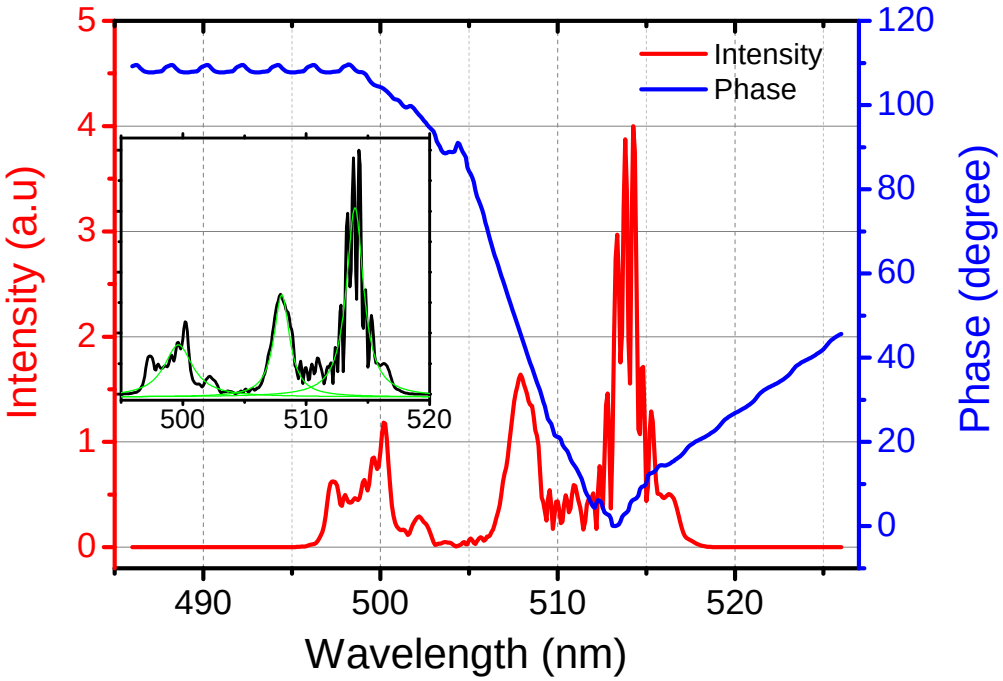

Figure 4.8: Spectral intensity and phase profiles of the optimal pulse. Inset shows the Gaussian fit (green) of the intensity profile peaks.

The spectral intensity and phase profiles of the optimal pulse show an artificially narrow shape. This narrow shape is due to the low power of the laser beam that serves as input to the FROG setup. Consequently, we present the calculated spectral intensity and phase profiles of the optimal pulse as shown in Figure 4.8. The spectrum is centered at 506.0 nm and is composed of three main peaks each with an additional substructure. The higher intensity peak is located on the red side of the spectrum at 513.9 nm with a FWHM of 1.8 nm, the peak in the middle is centered at 508.0 nm with a FWHM of 1.5 nm, and the smallest peak is located on the blue side of the spectrum at 499.6 nm with a FWHM of 2.8 nm. These results were obtained by Gaussian fits (Figure 4.8 inset) of the peaks. The blue solid line in Figure 4.8 presents the phase profile of the optimal pulse with a distinct shape similar to the spectral phase profile that was obtained in a previous coherent control experiment of CO_2 vibrational modes [123]. The phase values vary between 0° and 110°. The maximum values of the phase are located on the red side at $<$ 498 nm of the spectrum where the smallest peak of the spectral intensity profile is located and the minimum value is located at 517 nm close to the centre of the higher intensity peak. We suggest that the correlation between the minimum phase value and the maximum amplitude value could have a significant influence in achieving the optimal control.

In previous studies, the optimal pulse shape of coherent control experiments on the excitation energy flow in the light harvesting complex LH2 from *Rhodopseudomonas acidophila* [67, 140], and artificial light-harvesting complexes [116, 141] showed a similar train of pulses separated by few tens, and hundreds of femtoseconds, respectively. Such a pulse train can be obtained by applying the $[\phi = \mathrm{a}\sin(\mathrm{b}\omega) + \mathrm{c}]$ sinusoidal phase function on the SLM, where b is the modulation period, ω is the phase frequency, a is the factor that adjusts the amplitudes between subpulses (i.e it determines the depth of modulation), and c is the factor that adjusts the shift of the phase on the SLM [67, 68, 140, 142, 143]. It has been shown that, when the inverse modulation period of the optimal pulse (1/b) matches the frequency of a slow vibrational mode in the ground state, the first sub-pulses of the pulse train excite this mode to a higher vibrational level (still in the electronic ground state) via impulsive Raman scattering (IRS) [67, 116, 140, 142, 143]. Therefore, the following sub-pulses excite this mode to a higher electronic level at a specific coordinate of the potential energy surface, leading them to enhance a specific process such as internal conversion, isomerization, or energy transfer. These studies show that the frequency of the selected vibrational mode depends on the phase function that is applied to the SLM. In our study of LHCII, we suggest that the optimal pulse was modulated with a modulation function whose frequencies matched frequencies of vibrational modes that facilitated the energy transfer from carotenoids to Chl-a in the LHCII. These low-frequency vibrational modes most likely are related to the bending modes of the -C=C-C=C- backbone in carotenoids as proposed in the work on LH2 [67, 140].

4.5 Discussion

Our laser coherent control results show that we were able to manipulate the S_2 population and optimize the ET pathways in carotenoids of LHCII using shaped pulse trains with 178 fs temporal spacing between sub-pulses. In this study, we used an excitation energy corresponding to 1×10^{15} photons/cm^2, which is lower than the saturation energy for carotenoids (4×10^{18} photons/cm^2, calculated using formulas in [66]). At such low excitation energy the S_2 state highly can be populated with electrons without saturating the carotenoid $S_0 \rightarrow S_2$ transition [140]. Saturation occurs when the excitation energy exceeds the saturation energy threshold and induces multiple light-matter interactions that lead to multiple excitations on single chromophores, which are then de-excited via SE [144]. The coherent control experiment at such low excitation energy is classified as control in a weak field, which is preferred over an open-loop optimization method. In an open-loop technique, feedback from the experiment is not needed for the GA. Instead, small molecular systems with a finite number of eigenstates, which can be described using the Schrödinger equation, are used to obtain the electric field function that corresponds to the optimal pulse shape [66]. However, in our study, a closed-loop optimization method was utilized, because the LHCII trimer is a complex open quantum system that contains about 54 pigments [6, 11]. This makes it difficult to use the Schrödinger equation and obtain important information related to the optimal pulse shape. After excitation of a carotenoid to its S_2 state, the relatively fast IC via a conical intersection competes with the ET to the Chl-a. In this study, the optimization process curve started after the conical intersection point of the ET and IC potentials. This is because at 300 fs ET already has a bigger amplitude than IC as shown in the transient absorption spectrum (Figure 4.5).

Since the S_0-S_1 transition in carotenoids of LHCII is forbidden due to the inversion symmetry between the two states, the S_1 wave-packets' vibrational modes are not involved in the controlled mechanisms in this study. In previous pump-probe studies on β-carotene vibrational coherence was only created in the ground state potential energy surface, and the induced wave-packets in the S_2 potential energy surface were not transferable to the S_1 potential energy surface via IC [145]. These support the assumption that the S_1 wave-packets' vibrational modes are not involved in the controlled mechanisms in this study.

In previous coherent control experiments both the ET and IC processes were manipulated in carotenoids of natural LH2 [67, 140] and artificial light-harvesting complexes [68, 141] using pulse trains. In these studies, the authors suggested that modulation periods of the optimal pulses are synchronized with specific vibrational modes that facilitated the optimized process. Their suggestion was based on results of previous studies, in which selective amplification of a specific vibrational mode in the ground state via impulsive stimulated Raman scattering (ISRS) was achieved using an excitation pulse that is periodically modulated with a sinusoidal phase function [140, 142, 146–148]. In those studies, they have shown that the first few subpulses

of the pulse trains excite the ground state vibration mode whose frequency matches the pulse modulation period, while the rest of the pulse train excites this mode to a higher electronic state at a specific coordinate that correlates with a specific process such as IC, ET, or isomerization. Therefore, in this study, we suggest that optimization of the ET process over the IC process in carotenoid molecules is achieved by coherently controlling a vibrational mode that is related to the bending mode of the -C=C-C=C- backbone in carotenoids whose frequency matches the modulation period of the optimal pulse.

In a previous study that used dispersed multipump-probe spectroscopy techniques [144], it was suggested that optimization of some incoherent processes such as singlet-singlet annihilation and saturation could have a significant contribution to the overall optimization when using an intense pump beam with a very short temporal spacing between sub-pulses (i.e. in the order of 20 fs). As was explained in Section 1.4 , singlet-singlet annihilation would become a dominant process when using a high excitation intensity, which can also be involved in the optimized process.

In order to investigate the influence of singlet-singlet annihilation in the optimization process, we calculated the initial number (n_0) of excited molecules per trimer and the probability of having more than one excitation per trimer $P_{(n>1)}$ = 1-P_0 -P_1, where $P_i = \frac{(n_0)^i}{i!}e^{-n_0}$ is the Poisson distribution, which is used as an estimation for the probability of having a number of excitations per pulse [149, 150]. P_0 and P_1 are probabilities of having zero and one excitation, respectively. The utilized pump intensity in this study yielded n_0 = 0.31 which corresponds to $P_{(n>1)}$ = 4%. Additionally, the singlet-singlet annihilation in the LHCII complex has a rate of 24 ps^{-1} [150], which is long compared to the timescale at which the optimization experiment was performed. These results indicate that there is a low chance for singlet-singlet annihilation to be involved in the control mechanism. In order to avoid the effect of saturation, we utilized an excitation energy that was below the saturation energy limit. Moreover, the temporal spacing between the sub-pulses of the optimal pulse was 178 fs, which does not allow for saturation to occur.

To support the proposed mechanism of coherent control using multipulse excitation, several investigations have been conducted elsewhere [140]. In this study, the IC process was optimized over the ET process in the carotenoids of LH2, and the optimal pulse was used to excite the sample. The transient absorption amplitudes of IC and ET signals for different excitation energies were recorded. The results showed that for all utilized excitation energies the IC amplitudes were 60% optimized compared to the ET amplitude, indicating that the pulse energy was not involved in the optimization process, but the pulse shape was involved in optimizing the IC signal over the ET signal. In another experiment, IC and ET amplitudes of the optimal pulse and another defined pulse were measured at different excitation energies and compared. The defined pulse was obtained by adding π to the phase of optimal pulse. The results showed that the IC amplitude of the optimal pulse for all measured excitation energies was 35% optimized compared with those of the defined pulse, whereas the ET amplitude was shown to be very

sensitive to the change in phase.

In this study, the optimal pulse exhibited a periodic uniform structure indicating that light-matter interaction occurs in an iterative manner. This led to the creation of a coherent vibrational mode of wave-packets in the S_2 state which interfere constructively and enhance the ET process in carotenoids. Moreover, the optimal pulse shape has shown a similar structure as the shape of the optimal pulse that was obtained in previous coherent control experiments. Therefore we conclude that our results demonstrate clear evidence of quantum coherence of the controlled vibrational mode in carotenoids.

4.6 Conclusion

In this study, we have successfully optimized the yield of the energy transfer from carotenoids to Chls over the internal conversion in the carotenoids of the LHCII complex. The optimal pulse shape shows a structure that is formed by a series of 7 sub-pulses with a separation time of 178 fs between every two consecutive sub-pulses, and a FWHM of 92 fs for each sub-pulse. Such a pulse shape is a result of the sinusoidal phase function that was applied on the SLM as a modulation function. We conclude that the main mechanism responsible for optimization in this study originates from enhancement of specific vibrational modes of wave packets that facilitate the energy transfer process using a periodic excitation pulse. We also conclude that selection of the enhanced vibrational modes depends on the frequency of the modulation function that was applied on the SLM, which is similar to previous coherent control results. From the initial number of excitations per pulse, excitation energy, and the probability of having more than one excitation per complex per pulse, we conclude that optimization of incoherent processes such as singlet-singlet annihilation and saturation is negligible.

4.7 Future recommendations

Our aim in this study was to develop a coherent control setup that can be used to manipulate the ultrafast energy flow pathways from the S_2 state of carotenoids selectively excited at 506 nm in the LHCII complex. However, this setup can also be used to investigate the nonphotochemical quenching (NPQ) mechanism, which is utilised by plants, algae and cyanobacteria to protect themselves from photo-oxidative damage under high light conditions. Therefore, I make the following suggestions which might be useful to perform this investigation using the laser coherent control setup. In this study, the spectrograph is coupled to a photodiode array camera (NMOS camera) that has a bit-level resolution of 2^{12}, which requires more averages (minimum of 300 spectra) to have a good resolution for transient absorption spectra. Moreover, this NMOS camera communicates with a computer through the serial port RS232.

Using this detection system, it was possible to perform one laser coherent control experiment within 16 hours. In laser coherent control experiments on a complex molecular system such as LHCII, a high-resolution transient absorption spectra is required in addition to a large search space in order to achieve sufficient optimization. Therefore, we suggest that the NMOS camera has to be replaced with a fast CMOS camera that has a bit-level resolution of 2^{16} and higher dynamic resolution compared with NMOS camera. Moreover, CMOS camera communicates with a computer through USB 3.0 which is a very fast channel, and can operate directly with MATLAB. This suggestion should improve the quality of data by a factor of 16. Moreover, it shortens the time of experiments, so that it will be possible to perform measurements on a sample that has short stabilizing phase.

Investigation of the NPQ process requires a pump beam of 680 nm in order to excite Chl-a molecules that are involved in the NPQ process and to investigate the excitation transfer back from Chl-a to carotenoids. Our NOPA setup is capable of generating pump beam pulses at 680 nm, of a few tens of femtoseconds duration, which has to be compressed in order to access and control more vibrational modes. We therefore suggest that compression of the pump pulse after the NOPA setup should be implemented. A compressed pump pulse (transform-limited pulse) would lead to access and control of more vibrational modes, which might yield better optimization of certain dynamics. Moreover, the cylindrical lens in the 4F setup can be replaced with a convex mirror to avoid temporal pulse chirp and back reflection. We also suggest that the parabolic mirror of the FROG setup should be replaced with one that has a shorter focal length, more curved, allowing tighter focus for characterization of pulses at low energy.

Chapter 5

Energy dissipation mechanisms in the FCPb light-harvesting complex of the diatom *Cyclotella meneghiniana*

Abstract

Transient absorption spectroscopy has been applied to investigate the energy dissipation mechanisms in the nonameric fucoxanthin-chlorophyll-a,c-binding protein FCPb of the centric diatom *Cyclotella meneghiniana*. FCPb complexes in their unquenched state were compared with those in two types of quenching environments, namely aggregation-induced quenching by detergent removal, and clustering via incorporation into liposomes. Applying global and target analysis, in combination with a fluorescence lifetime study and annihilation calculations, we were able to resolve two quenching channels in FCPb that involve chlorophyll-a pigments for FCPb exposed to both quenching environments. The fast quenching channel operates on a timescale of tens of picoseconds and exhibits similar spectral signatures as the unquenched state. The slower quenching channel operates on a timescale of tens to hundreds of picoseconds, depending on the degree of quenching, and is characterized by enhanced population of low-energy states between 680 and 710 nm. The results indicate that FCPb is, in principle, able to function as a dissipater of excess energy and can do this *in vitro* even more efficiently than the homologous FCPa complex, the sole complex involved in fast photoprotection in these organisms. This indicates that when a complex displays photoprotection-related spectral signatures *in vitro* it does not imply that the complex participates in photoprotection *in vivo*. We suggest that FCPa is favored over FCPb as the sole energy-regulating complex in diatoms because

This Chapter is based on the following publication:
Huzifa M.A.M. Elnour, Lars Dietzel, Charusheela Ramanan, Claudia Büchel, Rienk van Grondelle, and Tjaart P.J. Krüger, Biochimica et Biophysica Acta (BBA)-Bioenergetics 1859 (10), 1151-1160, 2018.

its composition can more easily establish the balance between light-harvesting and quenching required for efficient photoprotection.

5.1 Introduction

Diatoms are unicellular photosynthetic organisms. They play an important role in the biochemical cycles of nitrogen, silicon, phosphorus and carbon, and, consequently, have a great impact on the global climate in marine and freshwater environments [34]. The light-harvesting complexes (LHCs) of diatoms belong to the same extended family as those of higher plants and green algae [9]. However, there are some clear differences in their protein and pigment compositions [14, 15]. Diatoms bind up to 8 chlorophyll-a (Chl-a) pigments per monomer [151], as in the main light-harvesting complexes of plants, LHCII [11]. However, diatoms bind Chl-c instead of the Chl-b found in LHCII. Furthermore, diatoms comprise unique types of carotenoids. The main carotenoid is fucoxanthin (Fx) and is present in a similar quantity as Chl-a [36], giving diatoms a brown colour and their LHCs the name of fucoxanthin-Chl-a,c-binding protein (FCP). FCPs additionally bind the xanthophyll-cycle pigments diadinoxanthin (Dd) and diatoxanthin (Dt) in substoichiometric amounts.

The two main types of FCP purified from centric diatoms like *Cyclotella meneghiniana* are known as FCPa and FCPb [15]. They mainly differ in their polypeptide composition and oligomeric state. FCPa is a trimer consisting of a mixture of the polypeptides Fcp1-3 from the Lhcf family and an Lhcx polypeptide in a smaller quantity, whereas FCPb assumes a nonameric arrangement [41] of Fcp5, a different type of Lhcf polypeptide [14]. The amount of Lhcx per FCPa scales with the light intensity incident on the diatoms and this polypeptide plays an important role in photoprotection [152]. Specifically, the photoprotection process known as nonphotochemical quenching (NPQ) of Chl-a fluorescence is triggered by a low lumenal pH and it is also associated with a high Dt content [15,25,153,154]. The fluorescence yield of isolated FCPa complexes was shown to depend strongly on the Dt content and the environmental pH, while FCPb was found to be insensitive to such changes [64,155]. FCPa is therefore widely considered to be the site of qE, the dominant, fast, energy-dependent, reversible component of NPQ, while FCPb is regarded to be merely involved with light harvesting.

Since the early studies of NPQ in higher plants, aggregation of light-harvesting complexes has been a useful model for the investigation of qE [51–53, 156, 157]. More recently, this approach was also used to investigate qE in diatoms [64, 155, 158]. Evidence of aggregation in the membranes of higher plants has been found under NPQ conditions [16, 159, 160]. Moreover, the fluorescence from isolated FCPa complexes was strongly reduced upon decrease of the ambient pH, likely due to spontaneous aggregation, while a lower pH only marginally reduced the fluorescence from isolated FCPb complexes, possibly due to their aggregation state remaining

unaltered [155]. Based on the above-mentioned evidence, NPQ models in diatoms have considered aggregation of FCPa complexes in the membrane as one of the excited-state quenching mechanisms [64, 70, 72, 161].

Time-resolved fluorescence measurements on whole high-light acclimated diatoms at room temperature have revealed two spectroscopic signatures of their NPQ state: a bathochromic shift of their fluorescence emission spectrum and enhanced emission between 700 and 750 nm, in the tail of the spectrum [70, 72]. These signatures were proposed to originate from the formation of FCPa aggregates [64]. In addition, 77 K steady-state fluorescence spectra of FCPa aggregates induced *in vitro* showed similar spectral features [70], but so do the spectra of FCPb aggregates [64]. In fact, the low-energy emission from FCPb aggregates is more pronounced than for FCPa aggregates [64] and may have an important contribution to the low-energy emission of diatoms under NPQ conditions. A Stark fluorescence spectroscopy study on FCPa and FCPb complexes revealed the appearance of a low-energy band peaking between 692 and 694 nm upon aggregation of both complexes [40]. The same study showed that FCPa aggregates exhibit an additional, more red-shifted emission band (peaking at 740 nm) and it was argued that FCPb complexes may display a similar behaviour *in vivo* [40].

Different thermal energy dissipative processes have been revealed through fluorescence and absorption studies [40, 64, 70–73], suggesting that qE is very likely established in diatoms through the combination of multiple processes involving different sites. The kinetics and spectral properties of quenching processes in FCPa involving Chl-a pigments were investigated in a recent room-temperature transient-absorption study of FCPa complexes in their solubilized and aggregated states, using selective Chl-a excitation [74]. Here, we apply a similar approach to FCPb in order to characterize the quenching processes in these complexes and to determine the similarities and differences compared to quenching processes taking place in FCPa. Quenching of FCPb was induced in two different ways, namely through strong aggregation by detergent removal, and by incorporating the complexes into liposomes of natural lipids with a high protein-to-lipid ratio. The latter represents a milder environment, giving rise to smaller clusters [162], and provides a better representation of the native environment of the complexes. Global and target analysis was applied to the data to resolve the energy transfer kinetics and timescales, with a particular focus on quenching states. In addition to singlet-singlet annihilation, we were able to resolve two quenching channels associated with different molecular mechanisms in FCPb and we identified their associated transient spectra and operation timescales.

5.2 Materials and methods

5.2.1 Sample preparation

Cyclotella meneghiniana (Culture Collection Göttingen, strain 1020-1a) was grown in artificial seawater [163] supplemented with 2 mM silica, in low light conditions (40 μmol photons $m^{-2}s^{-1}$, 16 h light, 8 h dark) with temperatures kept between 15-17 °C. Cells were harvested after one week of cultivation in the light-adapted state. FCPb isolation was carried out as described in [64]. In brief, thylakoids were isolated with a beadmill followed by an ultracentrifugation step. Thylakoids corresponding to 250 μg Chl-a ml^{-1} were solubilized with 20 mM β-dodecylmaltoside (β–DM) and subjected to ion exchange chromatography followed by ultracentrifugation using a freeze thaw gradient (19% sucrose (w/v), 25 mM Tris, pH 7.4, 2 mM KCl and 0.03 % (w/v) βDM). The collected FCPb fraction was washed in 25 mM Tris, 2 mM KCl, pH 7.4 and concentrated via ultrafiltration (centripreps, 30 kD cutoff). Liposomes were prepared as described in [162], using plant thylakoid lipids (Larodan Fine Chemicals, Sweden) with a Chl-a-to-lipid molar ratio of 12. Figure 5.8 shows the separation of purified FCPb complexes used in this study. FCPb aggregates were prepared by removing the detergent with bio-beads (SM-2 adsorbent, Bio-Rad) during continuous magnetic stirring and monitoring of the fluorescence intensity. The fluorescence yield of the aggregated FCPb was reduced by a factor of ten, after which the bio-beads were removed via centrifugation.

5.2.2 Spectroscopic methods

Steady-state spectroscopy

Steady-state absorption spectra were recorded with a Lambda 40 UV/VIS spectrometer (Perkin-Elmer) from 350 nm to 750 nm using 1 mm path length cuvettes. The fluorescence emission spectra were recorded with a Fluoromax-3 Horiba from 600 nm to 800 nm, upon excitation at 465 nm. For the fluorescence emission measurements, cuvettes with a 1 cm path length were used and samples were diluted to an OD of 0.05 at the maximum of the Chl-a Q_y band.

Fluorescence lifetime measurements

Time-resolved fluorescence measurements were performed using a FluoTime 200 fluorometer (PicoQuant). The samples were diluted into the appropriate buffer to an OD of 0.05 at the Q_y maximum of 672 nm and stirred in a cuvette with a path length of 1 cm. Excitation was provided by a 468 nm diode laser with a repetition rate of 10 MHz. An excitation energy of 8 nJ/pulse was used to pump the samples. The instrument response function (IRF) was obtained with pinacyanol iodide dissolved in methanol, which has a fluorescence lifetime of 6 ps [164].

Emitted fluorescence was recorded at 675 nm at an angle of 90° with respect to the excitation. All measurements were performed at ambient temperature, and the maximum number of counts in the peak channel was 20,000. The full width at half maximum of the IRF was 88 ps.

Transient absorption spectroscopy

Femtosecond transient absorption (TA) spectroscopy on the FCPb complexes incorporated into liposomes (plFCPb) and FCPb aggregates (qFCPb) was conducted with a pump-probe setup described in ref. [97], while annihilation studies on the solubilized FCPb (sFCPb) were performed on a setup described in ref. [29]. The main difference between the two setups is the laser source. The first setup [97] uses 80 fs laser pulses at a wavelength of 800 nm, obtained from a Ti:sapphire oscillator-regenerative amplifier (Coherent Mira seed and RegA) operating at a 40 kHz repetition rate. The second setup [29] is driven by an ultrashort 50 fs laser pulse at the wavelength of 800 nm at 1 kHz repetition rate, generated also from a Ti:sapphire oscillator (Coherent Mira seed) and amplified with a kilohertz amplifying system (Alpha-1000 US, B.M.Industries). For both setups, the pump beam wavelength was tuned to 680 nm and its polarization was set at the magic angle (54.7°) with respect to the probe beam polarization. The TA spectra were collected at pump energies of 6 nJ/pulse and 10 nJ/pulse for the plFCPb sample, whereas 10 nJ/pulse was used for qFCPb. In order to perform singlet-singlet (S-S) annihilation studies on the sFCPb sample, we used pump energies of 10, 20 and 30 nJ/pulse. The time evolution of the number of excitations $n(t)$ is given by [49, 149]:

$$\frac{\mathrm{dn(t)}}{\mathrm{dt}} = -\frac{1}{\tau}\mathrm{n(t)} - \gamma \mathrm{n(t)}^2 \tag{5.1}$$

which has the analytical solution

$$\mathrm{n(t)} = \frac{\mathrm{n_0 e^{(-t/\tau)}}}{1 + \frac{1}{2}\mathrm{n_0}\gamma\tau(1 - \mathrm{e^{(-t/\tau)}})} \tag{5.2}$$

where n is the number of excited nonamers per pulse at a time t after excitation, with $\mathrm{n(t=0)} = \mathrm{n_0} = \mathrm{I}\sigma$ being the initial number of excitations per pulse, I the intensity of the pump beam and σ the absorption cross-section of an FCPb nonamer. γ is the rate of S-S annihilation, and τ the lifetime of an exponential decay component. This kinetic method for the S-S annihilation study is valid for supermolecules such as small LHCII aggregates, which have a size greater than or equal to the excitation diffusion length [49, 149]. Due to the relatively large size of the FCPb complex, we assumed the same approach for this complex. The samples were inserted in a 1 mm path length cuvette, which was mounted on a shaker to prevent sample degradation from over-exposure due to multiple laser shots. Sample ODs were adjusted to 0.5 at the Chl-a Q_y absorption maximum. All measurements were conducted at room temperat-

ure (RT). Absorption spectra were taken before and after the TA measurements to monitor the stability of the samples. Global and Target Analysis [121, 122] was applied to analyze the TA spectroscopy data.

5.3 Results

5.3.1 Steady-state absorption and fluorescence emission spectra

The abbreviations sFCPb, plFCPb, and qFCPb will be used to denote solubilized FCPb nonamers, FCPb nonamers incorporated into liposomes and aggregated (quenched) FCPb complexes, respectively. The room-temperature steady-state absorption and fluorescence emission spectra of these complexes are displayed in Figure 5.1. The Soret and Q_y absorption bands of Chl-a are centered around 438 and 670 nm, respectively, whereas those for Chl-c are visible as a shoulder at 455 nm and a small band at 635 nm, respectively. The broad tail between 480 and 575 nm is principally due to the $S_0 \rightarrow S_2$ transition of fucoxanthin molecules and a minor contribution from the xanthophyll-cycle pigments, mainly diadinoxanthin. The spectral features correspond well with previous reports [14, 15, 158]. The liposome environment as well as aggregation induced significant broadening of the Soret band towards higher energies (i.e. shorter wavelength) and a slight enhancement in the tail of the Q_y band towards the red (Figure 5.1(a) inset). Similar broadening was observed for FCPa aggregates in a previous study [74]. The somewhat reduced amplitude between 500 and 560 nm and around 635 nm for qFCPb is likely due to pigment loss during bio-bead treatment to induce aggregation.

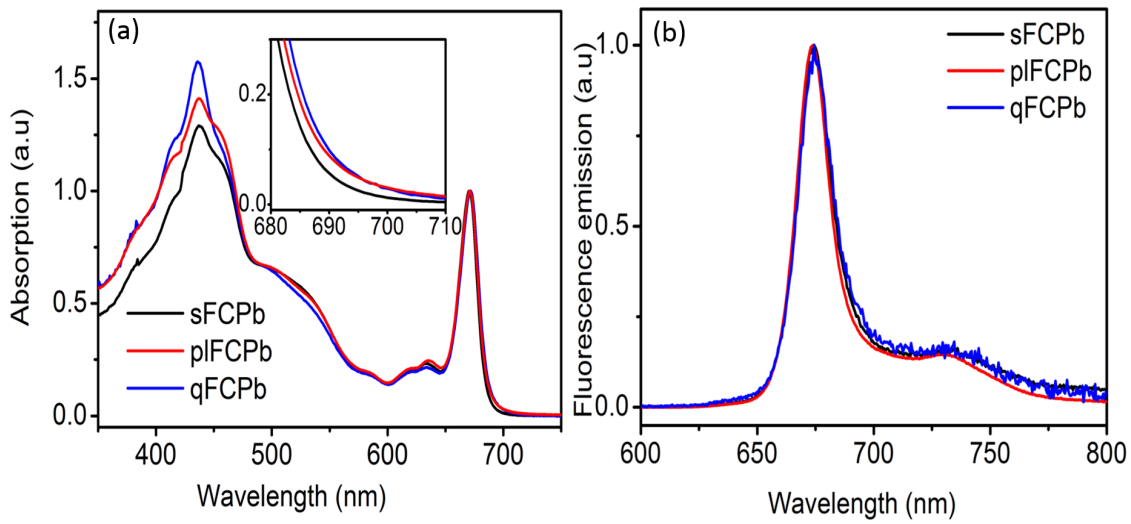

Figure 5.1: Steady-state (a) absorption and (b) fluorescence emission spectra upon excitation at 465 nm of sFCPb (black), plFCPb (red) and qFCPb (blue), normalized to the Chl-a Q_y band. Inset in (a) displays the same spectrum between 680 and 710 nm.

The fluorescence emission spectra of FCPb (Figure 5.1(b)) in all three investigated environments show a maximum at 674 nm and a vibrational band at around 735 nm. Since all pigments in the complex can be excited at 465 nm, the spectral shape is indicative of efficient excitation energy transfer to Chl-a [36]. The lack of significant differences between the spectra indicates that aggregation and incorporation into liposomes did not affect the steady-state spectroscopic properties of the pigments in FCPb, with the exception of the fluorescence lifetimes (*vide infra*). The slight broadening of the spectra of qFCPb and pIFCPb can be explained by scattering from aggregates.

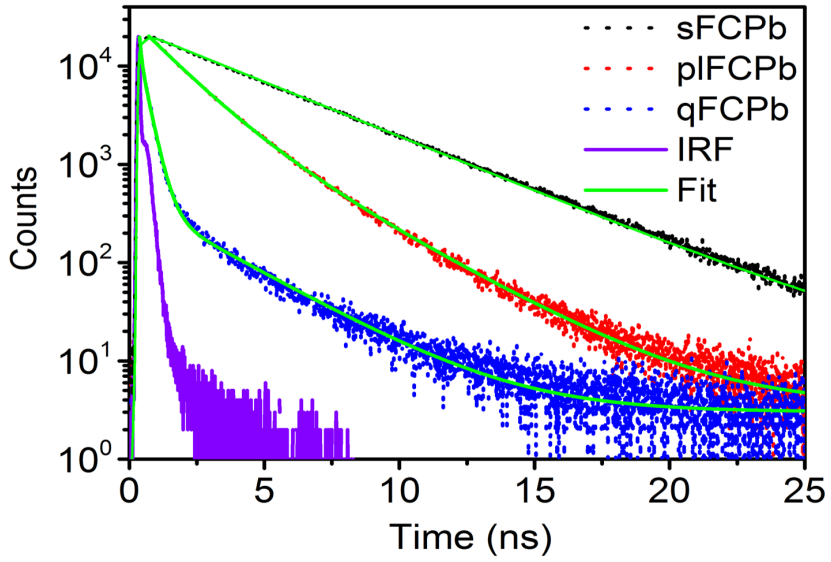

Figure 5.2: Fluorescence decay curves of sFCPb (black), plFCPb (red), qFCP (blue), Fit (green) and IRF (violet) detected at 675 nm at room temperature upon excitation at 468 nm. IRF denotes instrument response function.

5.3.2 Time-resolved fluorescence measurements

Time-correlated single-photon counting measurements revealed the fluorescence lifetimes of the FCPb complexes under the three conditions. The fluorescence decay kinetics are presented in Figure 5.2. The results are summarized in Table 5.1. sFCPb, which is more homogeneous than the other two samples, exhibited a monoexponential fluorescence decay with an average lifetime of 3.9 ns. For qFCPb and plFCPb at least two exponential components were required to obtain a satisfactory fit, which can be explained by the size heterogeneity of the samples. For qFCPb, the predominant fluorescence decay occurred within 90 ps, showing a substantial shortening of the lifetime. The average lifetime of the plFCPb complexes was only 2.6 times shorter than that of sFCPb but >11 times longer than that of qFCPb. The relatively small amount of quenching in plFCPb (as compared to qFCPb) can be explained by the milder quenching environment produced by the liposomes as opposed to detergent removal. The protein density inside

the liposome is an important factor affecting the fluorescence lifetime of the complexes. A large protein density increases the probability of protein–protein interactions [58, 64]. Since plFCPb constitutes a heterogeneous sample with varying protein densities, the fast and slow lifetime components possibly refer to average fluorescence lifetimes of FCPb complexes within more densely packed and less densely packed liposomes, respectively. The two lifetime components of qFCPb can be similarly explained as averages related to large and small aggregate sizes.

Table 5.1: Fitted decay times and relative amplitudes of the fluorescence decay curves of the FCPb nonamers (sFCPb), FCPb aggregates (qFCPb), and FCPb nonamers incorporated into liposomes (plFCPb). τ_1 and τ_2 are the fluorescence lifetime components, A_1 and A_2 the corresponding amplitudes, and τ_{ave} the weighted average of the lifetimes.

Sample	τ_1/ns	A_1	τ_2/ns	A_2	τ_{ave}/ns
sFCPb	3.88	1	-	-	3.88
plFCPb	0.82	0.50	2.21	0.50	1.51
qFCPb	0.09	0.97	1.28	0.03	0.13

5.3.3 Transient absorption spectroscopy

Global analysis

TA spectra were collected upon excitation at 680 nm. At this wavelength, Chl-a is excited selectively and the lowest-energy (i.e. red-most) Chls-a are excited with higher probability. To study the excited-state dynamics of Chl-a, we first analyzed the TA data globally using a sequential kinetic scheme. The resulting Evolution-Associated Difference Spectra (EADS) describe the dynamics of a mixture of spectroscopic species.

For the sFCPb data measured at 10 nJ/pulse pump energy, at least three components were needed to obtain a satisfactory fit. The corresponding EADS are presented in Figure 5.3(a). The initial component (1, black) appeared immediately after photoexcitation (i.e. at time zero) and evolved into the second EADS (2, red) in 5 ps. Its spectrum features an intense negative band peaking at 673 nm, which results from ground state bleach (GSB) and stimulated emission (SE) involving the Q_y transition of the red-most Chl-a pigments. The three positive signals peaking at 491nm, 600 nm and 642 nm are attributed to excited-state absorption (ESA) of Chl-a, because these signals are present immediately after photoexcitation and Chl-c and Fx are negligibly excited at 680 nm. In a transient-absorption study on LHCII where Chl-a was selectively excited at 675 nm, a broad ESA band with a peak position between 530 nm and 550 nm was resolved and similarly attributed to Chl-a [165]. The latter band is likely analogous to the broad Chl-a ESA band near 500 nm in Figure 5.3 and is red-shifted due to the different coupling strengths amongst the Chls and between Chls-a and carotenoids in LHCII as opposed

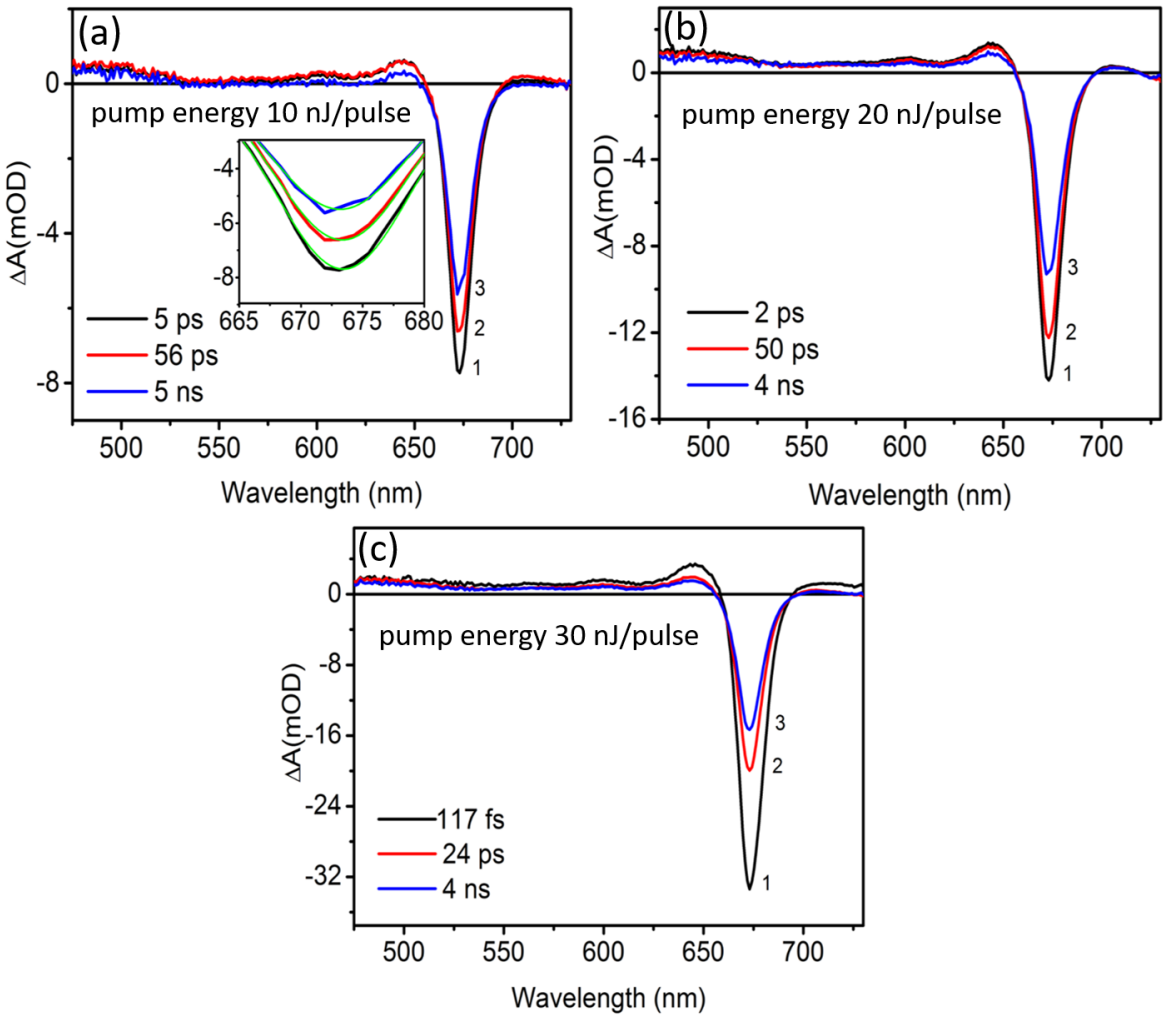

Figure 5.3: EADS and their lifetimes obtained by a sequential scheme in global analysis of the transient absorption data of the Chl-a excited state of sFCPb after pumping at (a) 10, (b) 20 and (c) 30 nJ/pulse. See text for details about the properties and possible origin of each of spectrum. Inset in (a) shows a magnification of the GSB/SE region and Gaussian fits (green) of the peaks within the displayed wavelength region.

to FCPb. The 0.8 nm blue-shifted GSB/SE peak of the second EADS as compared to that of the first EADS Figure5.3 (a), inset) is explained by uphill energy redistribution amongst the Chls-a after being pumped at 680 nm, which is about 10 nm red-shifted compared to the absorption maximum of those Chls (Figure 5.1).

This spectral shift, together with the decay time of the first EADS, indicates that the first EADS represents mainly excitation energy equilibration between Chl-a clusters with differing energies, i.e. different spectral pools. The second and third EADS exhibit similar features as the first EADS. The second spectrum takes 56 ps to decay into the third and final EADS (3, blue), which in turn relaxes into the ground state in 5 ns, a process attributed to spontaneous decay of Chl-a, mainly due to fluorescence emission and intersystem crossing. The amplitude of the GSB/SE band decreases during evolution to both the second and third EADS. This can be ex-

plained by S-S annihilation (*vide infra*) and likely also a small degree of excitation quenching that manifests as fluorescence blinking in single molecule studies [73]. The additional 1 nm blue-shift from the second to the third EADS (Figure 5.3(a), inset) indicates that uphill energy equilibration is not completed after 5 ps. We attribute this to re-equilibration after S-S annihilation that involves mostly the blue spectral pool of Chls.

The results from higher pump intensities are displayed in Figures 5.3(b) and (c). Three EADS were again required to fit the data and the spectral features are similar to those displayed in Figure 5.3(a). In Figure 5.3(b), shortening of the decay lifetime of the first EADS as compared to Figure 5.3(a) can be explained by S-S annihilation, while the substantially shortened lifetime of the same EADS in Figure 5.3(c) suggests that an additional ultrafast process was resolved, likely vibrational cooling within Chl-a excited states [74]. The second EADS in Figure 5.3(b) has a similar decay time as that of Figure 5.3(a), suggesting that S-S annihilation plays a minor role on this timescale. For all three pump energies, the lifetime of the last EADS is comparable to τ_{ave} for sFCPb in Table 5.1, suggesting only a small degree of annihilation and quenching in the complexes.

Table 5.2: Fitted decay times of the maximum TA signal of sFCPb near 673 nm, using Equation (5.2). n_0 is the initial number of excitations per pulse, τ is the lifetime of an exponential decay process, and γ is the S-S annihilation rate.

Pump energy	n_0	γ^{-1} /ps	τ/ps
10 nJ/pulse	1.22 ± 0.04	25.0 ± 0.1	4.00
20 nJ/pulse	2.31 ± 0.07	25.0 ± 0.1	1.72
30 nJ/pulse	9.41 ± 0.22	25.0 ± 0.1	0.20

To verify the timescale and significance of S-S annihilation in the isolated FCPb complexes, we calculated its lifetime and amplitude using Equation (5.2). The kinetics of the sFCPb TA data at 10, 20 and 30 nJ/pulse were monitored at 673 nm and fitted simultaneously using Equation (5.2) (Figure 5.4), with the fitting results summarized in Table 5.2. For all three pump energies, an annihilation time constant of 25 ps was obtained and an additional, shorter lifetime component was resolved, the latter of which scaled inversely with the pump energy and compared well with the lifetimes of the first EADS in Figure 5.3 for corresponding data. It is important to note that fitting of the three traces separately produced very similar results. S-S annihilation is expected to be more enhanced in plFCPb and qFCPb complexes due to their increased number of connected pigments as compared to sFCPb.

The EADS for plFCPb at a pump energy of 10 nJ/pulse were also best fitted with three kinetic components (Figure 5.5(a)). The overall structure and band positions of the three EADS are similar to those for sFCPb but the altered decay times signify important differences in the underlying kinetics. Compared to sFCPb, the first EADS (1, black) decayed somewhat faster.

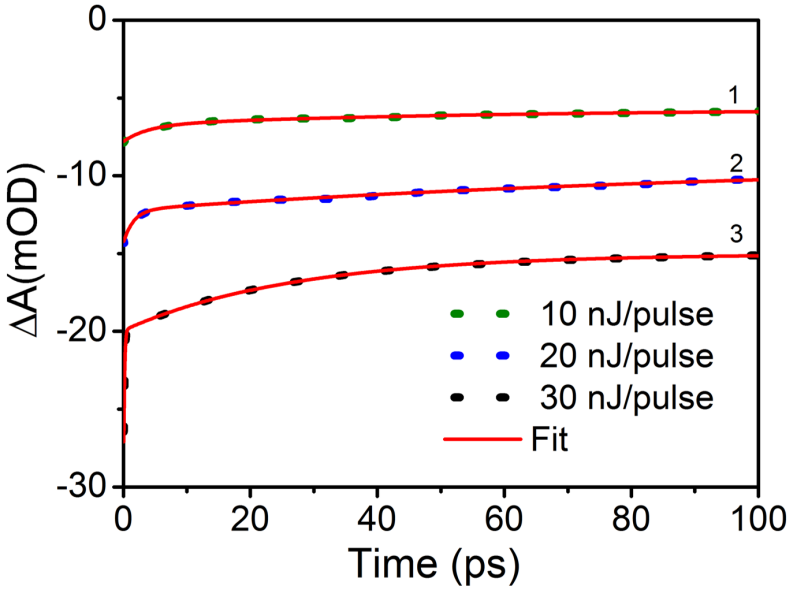

Figure 5.4: Transient kinetics monitored at maximum of the GSB/SE peak of sFCPb near 673 nm, for 10 nJ/pulse (green), 20 nJ/pulse (blue), and 30 nJ/pulse (black) excitations. The fit (red line) was obtained using Equation 5.2.

This can in part be explained by an increased amount of S-S annihilation due to an enlarged absorption cross-section in liposomes containing densely packed FCPb complexes, which constitute larger energetically connected domains than in the case of well-separated, solubilized complexes. The fluorescence lifetime results of plFCPb in Table 5.1 point to the presence of a slow and a fast quencher. Since annihilation was negligible in the lifetime study, there should be an additional quencher with decay dynamics strongly overlapping with that of annihilation and thus indiscriminable from the global analysis. The first EADS is again assigned to equilibration between the Chl-a spectral pools, as supported by the blue-shift of the second EADS (2, red). The small blue-shift of the third EADS (3, blue) suggests that the second EADS is again related to uphill re-equilibration following quenching of Chl-a with somewhat higher energies. Faster decay of the third EADS as compared to Figure 5.3(a) points to the presence of a slow quenching process. The considerably longer lifetime of the second EADS than in the case of sFCPb suggests a relatively long lifetime of the slow quenching process, in agreement with the fluorescence lifetime study (Table 5.1). Energy redistribution was also slowed down in the energetically coupled FCPb complexes inside the liposomes.

A new negative feature appeared in the third EADS of plFCPb from 680 nm to beyond 710 nm. Normalization of the spectra reveals that the second EADS also displays this feature with a small amplitude (Figure 5.9(a)). This low-energy feature does not manifest in the results of sFCPb for any of the pump energies and therefore suggests a new state induced by the lipid environment. Its prominence in the third and final EADS suggests that it is related to the slow quencher. This feature also explains the enhancement in the red tail of the Q_y band of the steady-state absorption spectrum (Figure5.1 (a) inset). The fitting residuals of the EADS

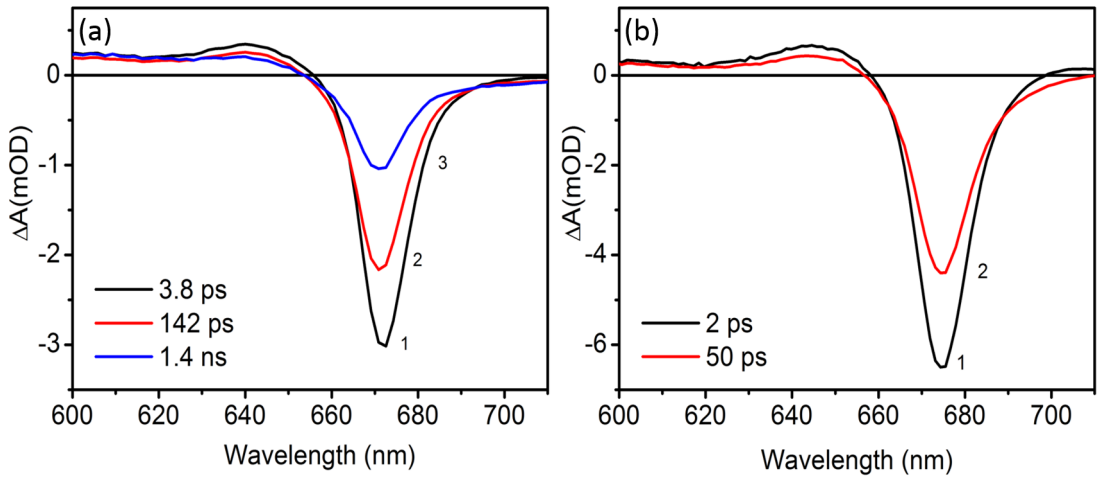

Figure 5.5: EADS and their lifetimes obtained by a sequential scheme in global analysis of the transient absorption data of (a) plFCPb and (b) qFCPb measured at 10 nJ/pulse pump energy. See text for details about the properties and possible origin of each spectrum.

shown in Figure 5.10 indicate that the red feature signifies a real signal.

For qFCPb pumped with the same energy, two kinetic components already provided a satisfactory fit of the EADS (Figure 5.5(b)). The main spectral features are similar to those for the other two samples. The faster decay of the first EADS (1, black) can be explained by annihilation and a fast quenching process like for plFCPb, considering again that the lifetime results of qFCPb suggest the presence of a slow and faster quenching process (Table 5.1), with the fast process strongly dominating. The average number of complexes forming an aggregate is expected to be significantly larger than the average number of strongly coupled complexes inside a liposome. It is also likely that the complexes are more strongly connected in an aggregate than inside a liposome. The short lifetime of the second and final EADS (2, red) indicates that the complexes are strongly quenched, in agreement with their short average fluorescence lifetime (Table 5.1). The second EADS displays a similar red feature between 680 and 710 nm as observed for plFCPb (see also the normalized spectrum in (Figure 5.9(a)), suggesting again formation of a new spectroscopic state related to the slow quencher. This red feature may similarly be connected with the slight broadening in the tail of the Q_y band in Figure 5.1. In a previous study, FCPa aggregates were observed to display a similar red feature on a timescale of several tens to hundreds of picoseconds [74].

Target analysis

Although a global analysis of the TA data of plFCPb and qFCPb failed to reveal the nature of the fast quenching process, our annihilation study clearly indicated the presence of annihilation, while the (free of S-S annihilation) fluorescence lifetime study suggested that an additional fast

quenching channel should exist. We applied target analysis to the plFCPb and qFCPb data to determine if this is indeed the case. Target analysis furthermore reveals the quantitative contributions of the fast and slow quenching processes and provides the spectra and rates of the various energy transfer and dissipation processes. We started with the simplest kinetic scheme: Model A containing two compartments, shown in Figure 5.6(a). The compartments, Chl1 and Chl2, describe the singlet excited states of red and blue absorbing Chl-a pools, with peak wavelengths at 673 and 671 nm, respectively. Their energy is quenched via two different quenching channels, q_1 and q_2, with rate constants k_1 and k_4, respectively, initially estimated from the last EADS in Figure 5.5. The distinct spectroscopic signatures of the two quenchers identified from global analysis suggest that the two quenchers are distinct and therefore independent. The initial populations of the two compartments were estimated from the global analysis results, which show that the ratio of the GSB/SE amplitude of Chl1 to that of Chl2 is ~1.5, and the energy transfer from Chl1 to Chl2 is faster than the back transfer. k_2 and k_3 are the rate constants of energy equilibration between the two compartments, the initial values of which were estimated from the lifetime of the first EADS. It is not necessary to include in the model a description of long-lived components such as triplet and unquenched singlet states due to their absence in the global analysis results.

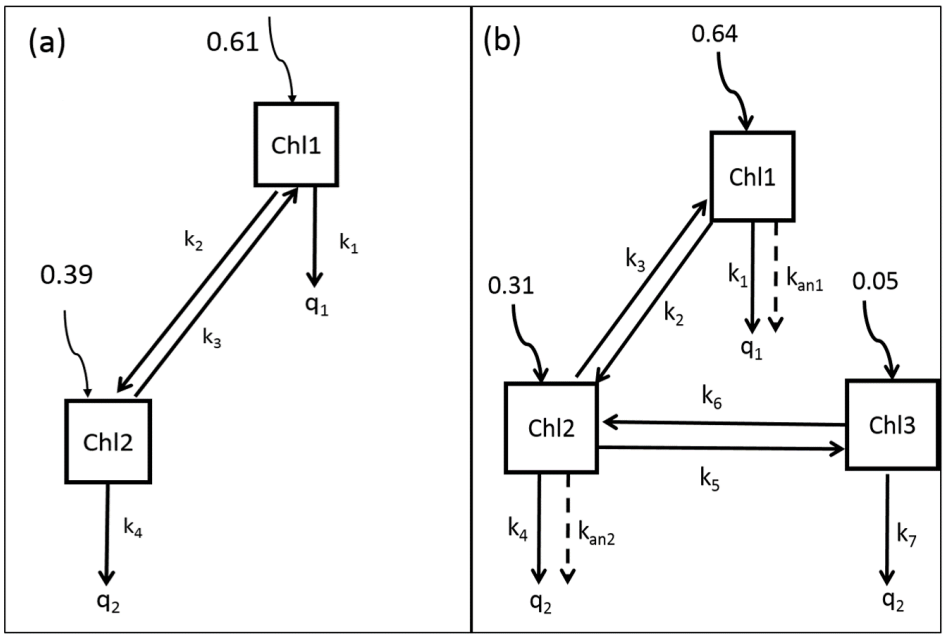

Figure 5.6: Compartment schemes used for target analysis to model the excited state dynamics of Chl-a in FCPb, using (a) two compartments (Model A) and (b) three compartments (Model B). Chl1, Chl2 and Chl3 are the compartments, k_{i} $(\mathrm{i} = 1,..,7)$ the rate constants, k_{an1} and k_{an2} the annihilation rate constants, and q_1 and q_2 represent quenchers. The excitation probability of each compartment is shown.

The Species-Associated Difference Spectra (SADS) are the spectra of the molecular species associated with the two compartments, as obtained from target analysis. The SADS of plFCPb

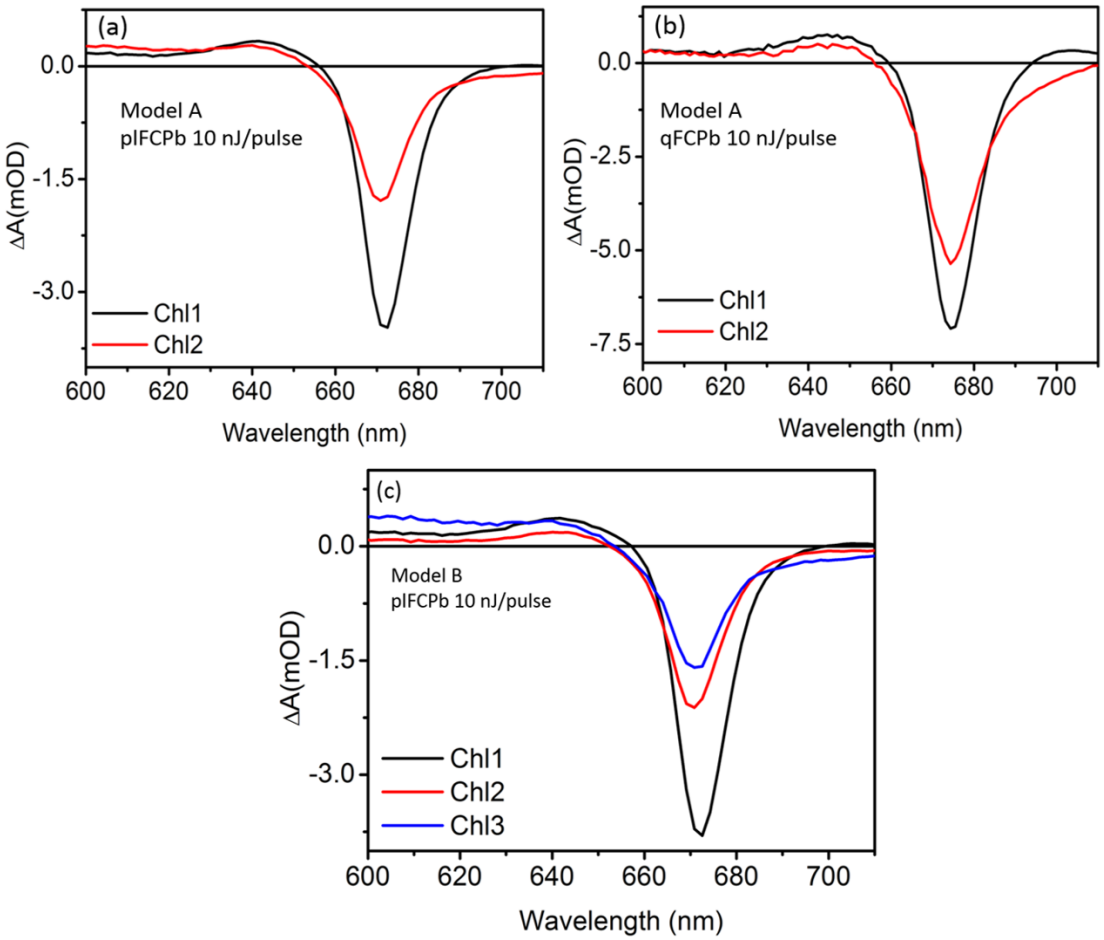

Figure 5.7: SADS of the Chl-a excited states using Model A for plFCPb (a) and qFCPb (b), and Model B for plFCPb (c).

and qFCPb for Model A are shown in Figure 5.7(a) and (b), respectively, and the rate constants of the excited-state dynamics are summarized in Table 5.3. Table 5.4 shows the changes in population amplitudes of the two compartments at the lifetimes of the two SADS with respect to the initial populations. These values provide a useful measure of the overall direction of excitation energy transfer resulting from re-equilibration at different timescales due to quenching and annihilation processes. A negative sign denotes a decrease in the initial population of the compartment (i.e. recovery of a signal), while a positive value indicates growth of the population. For plFCPb, at 5 ps after photoexcitation the loss in the Chl1 population is only a fraction greater than the gain in the Chl2 population. This stems from the rate k_1 of the fast quenching channel q_1 being significantly slower than the equilibration rates k_2 and k_3, in combination with the result that the values of k_2 and k_3 are comparable (Table 5.3). The population shift to Chl2 explains the blue-shifted SADS of this compartment. After 650 ps, the population of both compartments has decreased, where that of Chl1 is significantly smaller due to equilibration to Chl2 as well as quenching channel q_1 being significantly faster than q_2. The SADS of Chl2

displays a long red tail beyond 680 nm (Figure 5.7(a)), indicating population of redder states.

For qFCPb, equilibration between Chl1 and Chl2 occurred faster than for plFCPb. This can be explained by the stronger connectivity between individual FCPb complexes forming an aggregate than between those inside a liposome. In addition, aggregation may also induce changes inside individual FCPb complexes, such as small shifts in particular exciton energies and/or compression of the complexes. Both quenching processes occur considerably faster in the qFCPb model than for plFCPb, in agreement with the significant shortening of the associated EADS lifetimes in Figure 5.5(b). It is of note that k_1 is greater than k_2 and k_3, in contrast to the situation for plFCPb, highlighting the dominance of quenching process q_1. Moreover, the SADS of Chl2 also shows a red tail that is even stronger in qFCPb than in plFCPb.

The results from Model A suggest that the blue-absorbing Chl-a pool is associated with the strongly red-shifted state (absorbing beyond 680 nm) and confirm that the far-red feature is associated with a quenched state. The three lifetimes resolved from the EADS of plFCPb motivated the addition of a third compartment (Chl3) to our target model. This is done in Model B (Figure 5.6(b)). Simultaneous analysis of the data obtained at two different pump energies (6 nJ/pulse and 10 nJ/pulse) enabled us to decouple S-S annihilation from the two quenching processes. Annihilation was expected to affect the decay of Chl1 and Chl2. The initial values of the equilibration rates were obtained from Model A.

Since the far-red states feature on a relatively long timescale, Chl3 is expected to be strongly coupled with Chl2 and only weakly coupled with Chl1. Moreover, the energy in Chl3 is considered to be quenched through the same channel as for Chl2, involving q_2, albeit at a different rate due to the different nature of this state. This is because of the strong coupling between Chl2 and Chl3 compartments. Equilibration between Chl1 and Chl2 is established through rate constants k_2 and k_3, while equilibration between Chl2 and Chl3 is determined by k_5 and k_6. Due to the weak coupling between Chl1 and Chl3, equilibration between them is expected to be significantly slower than for the other processes and, for simplification, the associated rates were omitted from the model. The rates k_1, k_4, k_{an1} and k_{an2} were kept free, while all other rates were kept the same for the two data sets.

Table 5.3: Decay rate constants (in ns^{-1}) for plFCPb and qFCPb obtained from target analysis with Model A.

Sample	k_1	k_2	k_3	k_4
plFCPb	20	137	123	1
qFCPb	914	270	114	7

Upon photoexcitation, the Chl1 compartment is more populated than the other two compartments. Initially, the population of Chl1 is therefore expected to decrease due to equilibration, while those of Chl2 and Chl3 should increase, as observed in Table 5.6. The energy equilibra-

Table 5.4: Changes in population amplitudes of Chl1 and Chl2 compartments monitored at two times for plFCPb and qFCPb obtained with Model A. A negative sign indicates a decrease and a positive sign an increase.

Sample	plFCPb		qFCPb	
Lifetime (ps)	5	650	3	45
Chl1	-0.27	-0.79	-0.38	-0.52
Chl2	+0.23	-0.20	+0.14	-0.13

Table 5.5: Equilibration, decay and annihilation rate constants (in ns^{-1}) for plFCPb pumped with 6 nJ/pulse and 10 nJ/pulse energy, as obtained using Model B.

pump energy	k_1	k_2	k_3	k_4	k_5	k_6	k_7	k_{an1}	k_{an2}
6 nJ/pulse	6	226	127	8	33	1	1	10	13
10 nJ/pulse	7	227	127	9	33	1	1	55	18

tion is affirmed by the blue-shift of the SADS of Chl2 and Chl3, as indicated in Figure 5.7(c). The rates of quenching of plFCPb pumped with 6 nJ/pulse and 10 nJ/pulse energies according to Model B are shown in Table 5.5. An initial population of 5% of Chl3 provided the best fit. This relatively small value in accordance with the slow formation of the far-red states, as suggested by the global analysis results. After 200 ps both Chl1 and Chl2 populations have decreased as compared to their amplitudes at 5 ps, while the Chl3 population has increased further. Decay of the Chl3 population, which is visible after 750 ps, was the slowest process of all and explains the relatively small red-shift of the Chl3 spectrum as compared to the Chl2 spectrum, because of equilibration to the far-state. From the starting values of the scaling parameter of the k-matrix we calculated that approximately 51% of the excitations were quenched via q_1, 16% via annihilation, and 33% via q_2 in the plFCPb sample, confirming that q_1 is the dominant quenching process. The results indicate that the kinetics of plFCPb are well-explained in terms of S-S annihilation in addition to two independent quenching processes, similarly to FCPa aggregates [74]. The same is expected for qFPCb. From the global and target analysis results, we conclude that the two fluorescence lifetime components of plFCPb (Table 5.1) are due to the presence of two different quenching channels.

Table 5.6: Changes in population amplitudes of Chl1, Chl2 and Chl3 compartments monitored at three times for plFCPb pumped at 10 nJ/pulse. These amplitudes are obtained from target analysis with Model B. Negative and positive signs again indicate a decrease and an increase in populations, respectively.

Lifetime (ps)	5	200	750
Chl1	-0.39	-0.59	-0.61
Chl2	+0.36	+0.10	-0.20
Chl3	+0.10	+0.18	-0.07

5.4 Discussion

Our analysis of the transient absorption data of plFCPb and qFCPb complexes points to the presence of two quenching channels in FCPb, both of which involve Chl-a. The first, fast channel (q_1) operates on a timescale of several tens of picoseconds for plFCPb and is expected to operate in qFCPb on a shorter timescale. The associated difference-absorption spectra do not exhibit a noticeable difference compared to the spectrum of solubilized FCPb. In this study, the majority of excitations decayed via this channel. Since equilibration to the blue is visible in the GSB/SE band during and after energy loss via q_1, we can conclude that the Chls with the lowest energy (i.e. the terminal emitter Chls) are mostly involved and that the processes take place on multiple timescales. The second, slower quenching channel (q_2) occurs on a timescale of hundreds of picoseconds for plFCPb and down to tens of picoseconds for qFCPb. This quencher is responsible for enhanced population of states absorbing from 680 nm to beyond 710 nm and involves mainly the blue-shifted Chl-a pool.

The first quenching state has not been detected before for FCPb, likely because of the similarity of its spectral signature compared to that of the unquenched state. The characteristics of the second quencher are similar to those of a spectral state identified from a transient absorption study on FCPa aggregates [74]. Although a similar signal was absent from the Stark data of FCPb aggregates it was predicted to exist [40]. The signal of this quenched state has now been resolved in the present study and further kinetic information has been provided.

The involvement of a charge-transfer state is the best explanation for the large red-shift of the low-energy band identified from the Stark study and its strong response to an externally applied electrical field [40]. For photosystem I of plants, which exhibit similar low-energy states, it has been established that low-energy spectral states originate from a Chl dimer due to mixing between a charge-transfer state and one or more of the lowest exciton states [166, 167]. The low-energy emission states from plant LHCII aggregates as well as FCP aggregates have been proposed to originate from a similar mechanism, but involving Chls-a from adjacent complexes [59,70]. However, states with similar properties have been observed from single, isolated LHCs from plant photosystem II [168, 169] and were related to the low-energy states of photosystem I LHCs [169], suggesting that the red states in isolated and aggregated LHCs of plants involve a Chl dimer within a complex instead of between different complexes.

Blue-absorbing Fx molecules are proposed to be located close to Chl-a molecules in the FCPs complexes similar to lutein molecules in LHCII [151, 170]. Association of the slow quencher with the blue Chl-a pool therefore suggests the involvement of one or more Fx molecules. Fx is characterized by a strong intramolecular charge-transfer (ICT) state coupled to the molecule's S_1 state to form a mixed S_1/ICT state [38,39]. In FCP, the latter state couples strongly to the Q_y exciton states of neighbouring Chls-a to give rise to ultrafast energy transfer [36, 158]. Due to this strong coupling and the 'availability' of a charge-transfer state, it is natural to assume that

Fx's ICT state will mix into some of the Chl-a exciton states, thus giving rise to quenching and low-energy emission. This was also the explanation for the ~694-nm emission state of FCPb in the Stark study [40].

In a TA spectroscopy study on solubilized and aggregated FCPa [74] very similar results were obtained as in the present study. Specifically, for aggregated FCPa, two quenchers in the Chl-a pool were identified in addition to annihilation, with almost identical spectral signatures and transient dynamics as for FCPb. This leads us to conclude that the origin of the slow quencher (q_2) is the same in FCPa and FCPb and that FCPb has the same capability as FCPa to serve as a dissipater of excess excitation energy.

The NPQ-related spectral properties are therefore not unique to FCPa. This can be explained by the strong similarity of FCPa and FCPb in terms of protein sequence – and hence structural homology – as well as pigment composition [64]. *In vivo*, the two quenching channels are likely activated in FCPa upon aggregation in the membrane under NPQ conditions [64, 70, 72].

Although *in vitro* aggregation of FCPb is just as easily induced as for FCPa, it is very unlikely that FCPb aggregates are formed *in vivo*. A time-resolved fluorescence study on whole *Cyclotella meneghiniana* cells indicated that the FCPb signal shows no sign of quenching under NPQ conditions [72], and neither Dt content nor low pH values influence the fluorescence yield of FCPb, in stark contrast to FCPa [64]. Yet, FCPb seems to be an even more efficient energy dissipater than FCPa: in a similar TA study on FCPa [74], 15-times quenched FCPa aggregates were used, as opposed to 10-times quenched FCPb aggregates in the present study, but the quenching rates of those FCPa aggregates were significantly slower than for the FCPb aggregates reported here.

This prompts us to ask why FCPb is not involved with NPQ *in vivo*. To act as a useful regulator of excitation pressure, quenching of FCPs has to be highly regulated in order to avoid permanent NPQ. Use of a weaker quencher might be easier to control and thus fine-tune NPQ more easily.

Aggregation of FCPa is likely triggered by the glutamate residue on the lumenal side of the Lhcx and/or specific Lhcf polypeptides [64], which are probably sensitive to pH changes in the lumen and possibly also to binding of Dt in its vicinity. Fcp5, the sole component of FCPb, does not contain this specific glutamate [64]. The difference of such a single amino acid is probably sufficient to regulate the involvement of FCPa in qE and not FCPb, despite the fact that FCPb could equally well serve as an efficient dissipater of excess energy if a mechanism for *in vivo* FCPb aggregation existed. It has to be noted that FCPb complexes exist only in centric diatoms, whereas they are missing in pennate diatoms (like *Phaeodactylum tricornutum*) that also display a high NPQ capability. Use of FCPa is therefore sufficient for the fine regulation involved with qE.

The lipid environment produced very similar spectroscopic signatures as aggregation, suggest-

ing that common quenching mechanisms are involved. In fact, there is sufficient motivation for considering the lipid environment a more suitable model for studies of (photoprotective) energy dissipation. First, in this study, lipid interaction induced only a relatively small degree of quenching while the quenching-related spectral signatures were pronounced. Specifically, the amount of quenching in plFCPb was significantly less than in qFCPb while the far-red signal related to the slow quencher in plFCPb was somewhat more intense than for qFCPb. This observation indicates that the amplitude of the far-red spectral band is not related to the strength of quenching. Second, aggregates may introduce spectral artifacts: (i) *in vitro* aggregation using a detergent concentration below the critical micelle concentration, as frequently done [64, 155], leads to uncontrolled aggregation, typically producing large, three-dimensional structures, unlike what is expected *in vivo*, (ii) the presence of even a small fraction of non-functional or denatured complexes may introduce additional energy traps and amplify the extent of quenching when bound to large aggregates, and (iii) aggregation produced with bio-beads can lead to the loss of pigments located peripherally in the complexes due to strong hydrophobic interactions, as observed in Figure 5.1 for qFCPb.

5.5 Conclusions

In this study, we were able to resolve two quenching channels in FCPb that are created when the complexes are aggregated and when they are incorporated in liposomes. The two quenching channels are associated with different molecular mechanisms and operate at different timescales. The first, fast quenching mechanism occurs on a timescale of tens of picoseconds within the red Chl-a pool. The second, slow quenching mechanism is characterized by a far-red absorption state and likely originates from an Fx S_1/ICT state mixed with a higher energy (blue) Chl-a exciton state. In addition, we calculated a singlet-singlet annihilation rate of 25 ps^{-1} in isolated FCPb complexes subjected to high excitation pulse energies. Our results show that FCPb aggregates are stronger quenchers than FCPa aggregates and FCPb therefore has the potential to quench excess excitations more efficiently than FCPa, yet FCPb does not play a role in qE because of its lack of Lhcx subunits and missing regulatory, pH-sensing amino acid residues. Motivations were given for why the proteoliposomes provide a better model system for energy-dissipation studies than aggregation. Finally, we conclude from this study that the presence of both excitation quenching and a far-red spectral signal *in vitro* is not sufficient evidence for any light-harvesting complex's participation in qE *in vivo*, because aggregated of FCPb exhibit these signatures but are not involved with qE.

5.6 Appendix: Supplementary information

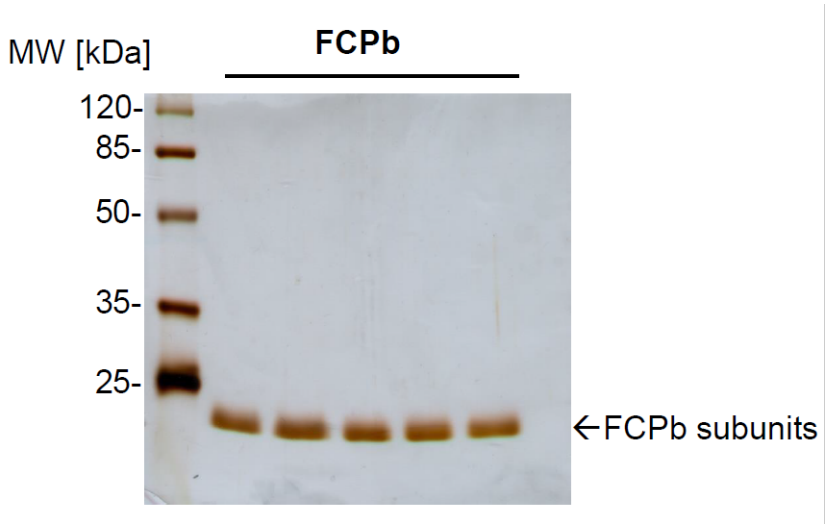

Figure 5.8: Separation of purified FCPb subunits. FCPb subunits were purified as described in the main manuscript. The image represents all batches of FCPb preparations used for the manuscript. The FCPb subunits migrate in a single band of 19 kDa [15]. FCPb corresponding to 0.5 μg Chl-a was loaded in each well. The gel electrophoresis was performed using a tris-tricine buffer system with 12% polyacrylamide according to Schägger and Jagow [171]. Silver staining procedure was based on Chevallet [172]

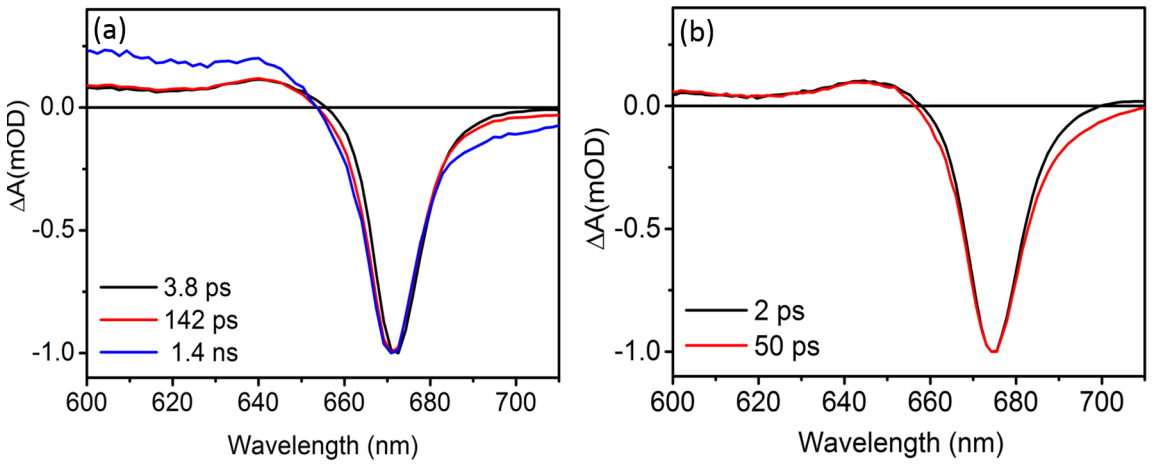

Figure 5.9: Normalized EADS spectra from the global analysis of plFCPb (a) and qFCPb (b) TA data, that correspond to EADS spectra in Figure 5.5. The normalized spectra clearly demonstrate the broadening from 680-710 nm on the last EADS spectra in Figures 5.5 (a) and (b).

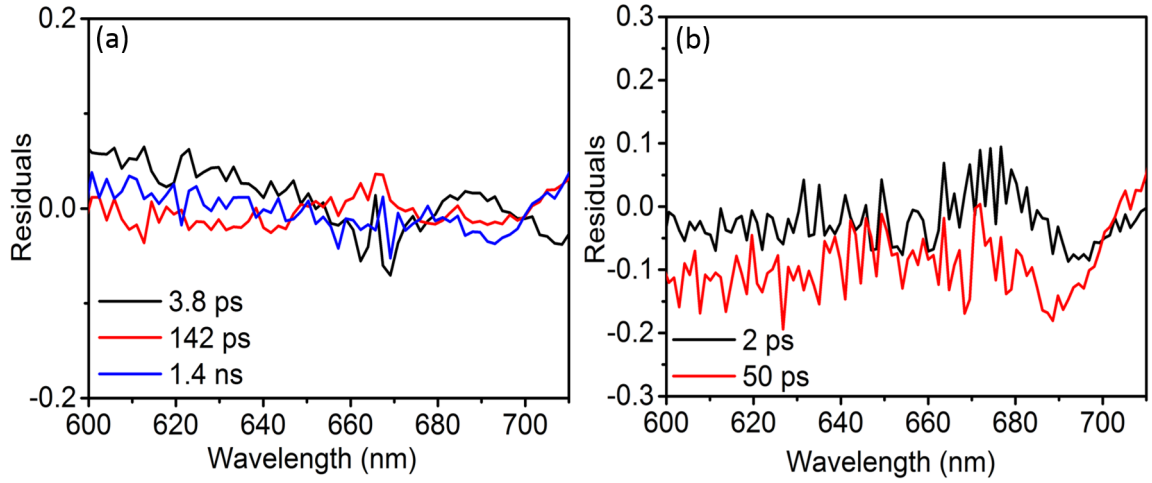

Figure 5.10: Residuals curves of the global analysis fit of the plFCPb (a) and qFCPb (b) TA data, that correspond to the plFCPb and qFCPb EADS spectra in Figure 5.5 (a) and (b), respectively. These residuals show no any particular pattern, which confirm that the broadening from 680-710 nm on the last EADS spectra in Figures 5.5 (a) and (b) are real signals.

Chapter 6

Summary

Photosynthesis is a biological process that is carried out by a number of organisms including plants, algae, and some bacteria. In this process, solar energy is used to produce organic components that are stored in molecules and later used to power cellular processes in organisms and, ultimately, serve as an energy source for virtually all forms of life. The light absorption process forms the first step in photosynthesis, and is accomplished by pigments of light-harvesting complexes. The solar energy collected in this way is used to drive photochemical processes after being transferred to the reaction center. Some of the collected solar energy can be thermally dissipated by internal conversion or photoprotection mechanism. The efficiency of photosynthetic light-harvesting is ultimately determined by the amount of absorbed energy that is transferred from the light-harvesting complex pigments to the reaction center of the photosystem. In the last few decades, several studies have been conducted to understand energy transfer processes and photoprotection mechanisms in natural photosynthetic systems. We believe that a detailed understanding of energy transfer processes and photoprotection mechanisms in living organisms, will be of utmost importance for synthesizing artificial systems that perform energy transfer and photoprotection in a similar way as the natural ones. Studying the principles of natural photosynthesis and photoprotection is therefore a vital step toward improving the performance of artificial photosynthetic devices. The research presented in this thesis was aimed at understanding the energy transfer and dissipation mechanisms in the natural light-harvesting complexes using coherent control and transient absorption spectroscopy techniques.

In Chapter 4, results of the coherent control of excitation energy flow pathways from the S_2 state of carotenoids in LHCII, show that we have successfully optimized the yield of the energy transfer channel over the internal conversion channel using a multipulse shape. The optimal pulse shape was characterized and related to the controlled mechanism. By comparing our results with some previous results of laser control experiments, we concluded that the main mechanism responsible for the optimization is the enhancement of a selected vibrational mode that facilitates the energy transfer process. The selection of this specific vibrational mode

depends on the period of the phase function modulation that was applied on the SLM to generate the optimal pulse. From the initial number of excitations per pulse, excitation energy, and the probability of having more than one excitation per complex per pulse, we concluded that optimization of incoherent processes such as singlet-singlet annihilation and saturation does not play a great role in the overall optimization process.

In Chapter 5, the energy dissipation mechanisms in the FCPb light-harvesting complex of the diatom Cyclotella meneghiniana are investigated using transient absorption spectroscopy and fluorescence lifetime calculations, in addition to annihilation experiments. FCPb complexes were investigated in their quenched and unquenched states. Two types of FCPb quenched states were induced, namely aggregation-induced quenched states (by detergent removal) and clustering via incorporation into liposomes. The two quenching channels are associated with different molecular mechanisms and operate at different timescales. The first, fast quenching mechanism occurs on a timescale of tens of picoseconds within the red Chl-a pool. The second, slow quenching mechanism is characterized by a far-red absorption state and likely originates from an Fx S_1/ICT state mixed with a higher energy (blue) Chl-a exciton state. In addition, we calculated a singlet-singlet annihilation rate of 25 ps^{-1} in isolated FCPb complexes subjected to high excitation pulse energies. This study shows that the FCPb complex is able to function as a dissipater of excess energy more efficiently than the homologous FCPa complex, which is the only complex involved in photoprotection in this organism. However, these *in vitro* investigations do not imply that the complex participates in the photoprotection mechanism *in vivo*, due to the fact that aggregation of the FCPb also exhibits these signatures, but is not involved in qE.

Bibliography

[1] R. E. Blankenship, *Molecular Mechanisms of Photosynthesis*. Wiley/Blackwell, 2014.

[2] N. Nelson and A. Ben-Shem, "The complex architecture of oxygenic photosynthesis," *Nature Reviews Molecular Cell Biology*, vol. 5, no. 12, pp. 971–982, 2004.

[3] J. Whitmarsh and Govindjee, "The photosynthetic process," in *Concepts in Photobiology* (G. Singhal, G. Renger, S. Sopory, K. Irrgang, and Govindjee, eds.), pp. 11–51, Springer Netherlands, 1999.

[4] Somepics, "Light-dependent reactions of photosynthesis in the thylakoid membrane of plant cells. I redrew and formatted it for a better quality SVG file," 2015.

[5] J. L. Tymoczko, J. M. Berg, and L. Stryer, *Biochemistry: a short course*. Macmillan, 2011.

[6] J. Standfuss, A. C. T. van Scheltinga, M. Lamborghini, and W. Kühlbrandt, "Mechanisms of photoprotection and nonphotochemical quenching in pea light-harvesting complex at 2.5 Å resolution," *The EMBO journal*, vol. 24, no. 5, pp. 919–928, 2005.

[7] R. van Grondelle and V. I. Novoderezhkin, "Energy transfer in photosynthesis: experimental insights and quantitative models," *Physical Chemistry Chemical Physics*, vol. 8, no. 7, pp. 793–807, 2006.

[8] V. Sundström, "Photosynthetic light harvesting, charge separation, and photoprotection: The primary steps," in *Photobiology*, pp. 289–319, Springer, 2008.

[9] B. R. Green, E. Pichersky, and K. Kloppstech, "Chlorophyll a/b-binding proteins: an extended family," *Trends in biochemical sciences*, vol. 16, pp. 181–186, 1991.

[10] G. F. Peter and J. P. Thornber, "Biochemical composition and organization of higher plant photosystem II light-harvesting pigment-proteins.," *Journal of Biological Chemistry*, vol. 266, no. 25, pp. 16745–16754, 1991.

[11] Z. Liu, H. Yan, K. Wang, T. Kuang, J. Zhang, L. Gui, X. An, and W. Chang, "Crystal structure of spinach major light-harvesting complex at 2.72 *Å* resolution," pp. 287–92, 2004.

[12] R. Croce, S. Weiss, and R. Bassi, "Carotenoid-binding sites of the major light-harvesting complex II of higher plants," *Journal of Biological Chemistry*, vol. 274, no. 42, pp. 29613–29623, 1999.

[13] R. Croce and H. van Amerongen, "Light-harvesting and structural organization of photosystem II: From individual complexes to thylakoid membrane," *Journal of Photochemistry and Photobiology B: Biology*, vol. 104, no. 1, pp. 142 – 153, 2011.

[14] C. Büchel, "Fucoxanthin-chlorophyll proteins in diatoms: 18 and 19 kDa subunits assemble into different oligomeric states," *Biochemistry*, vol. 42, no. 44, pp. 13027–13034, 2003.

[15] A. Beer, K. Gundermann, J. Beckmann, and C. Büchel, "Subunit composition and pigmentation of fucoxanthin-chlorophyll proteins in diatoms: evidence for a subunit involved in diadinoxanthin and diatoxanthin binding," *Biochemistry*, vol. 45, no. 43, pp. 13046–13053, 2006.

[16] A. V. Ruban, *The photosynthetic membrane: molecular mechanisms and biophysics of light harvesting*. John Wiley & Sons, 2012.

[17] H. K. Lichtenthaler and C. Buschmann, "Chlorophylls and carotenoids: Measurement and characterization by UV-VIS spectroscopy," *Current Protocols in Food Analytical Chemistry*, 2001.

[18] M. Gouterman, G. H. Wagniére, and L. C. Snyder, "Spectra of porphyrins: Part ii. four orbital model," *Journal of Molecular Spectroscopy*, vol. 11, no. 1-6, pp. 108–127, 1963.

[19] H. Y. Yamamoto and R. Bassi, *Carotenoids: Localization and Function*, pp. 539 – 563. Dordrecht: Springer Netherlands, 1996.

[20] H. A. Frank and R. J. Cogdell, "Carotenoids in photosynthesis," *Photochemistry and photobiology*, vol. 63, no. 3, pp. 257–264, 1996.

[21] D. DellaPenna, "Carotenoid synthesis and function in plants: insights from mutant studies in arabidopsis thaliana," in *The photochemistry of carotenoids*, pp. 21–37, Springer, 1999.

[22] D. Siefermann-Harms, "The light-harvesting and protective functions of carotenoids in photosynthetic membranes," *Physiologia Plantarum*, vol. 69, no. 3, pp. 561–568, 1987.

[23] E. Peterman, F. M. Dukker, R. Van Grondelle, and H. Van Amerongen, "Chlorophyll a and carotenoid triplet states in light-harvesting complex II of higher plants," *Biophysical journal*, vol. 69, no. 6, pp. 2670–2678, 1995.

[24] P. Horton, A. V. Ruban, and M. Wentworth, "Allosteric regulation of the light-harvesting system of photosystem II," *Philosophical Transactions of the Royal Society of London B: Biological Sciences*, vol. 355, no. 1402, pp. 1361–1370, 2000.

[25] B. Demmig-Adams and W. W. Adams III, "The role of xanthophyll cycle carotenoids in the protection of photosynthesis," *Trends in Plant science*, vol. 1, no. 1, pp. 21–26, 1996.

[26] T. Gillbro and R. J. Cogdell, "Carotenoid fluorescence," *Chemical Physics Letters*, vol. 158, no. 3, pp. 312 – 316, 1989.

[27] K. Yasushi, "New trends in photobiolog: Structures and functions of carotenoids in photosynthetic systems," *Journal of Photochemistry and Photobiology B: Biology*, vol. 9, no. 3, pp. 265 –280, 1991.

[28] T. Polívka and H. A. Frank, "Molecular factors controlling photosynthetic light harvesting by carotenoids," *Accounts of chemical research*, vol. 43, no. 8, pp. 1125–1134, 2010.

[29] C. C. Gradinaru, I. H. M. van Stokkum, A. A. Pascal, R. van Grondelle, and H. van Amerongen, "Identifying the pathways of energy transfer between carotenoids and chlorophylls in LHCII and CP29. a multicolor femtosecond pump-probe study," *The Journal of Physical Chemistry B*, vol. 104, no. 39, pp. 9330–9342, 2000.

[30] T. Barros and W. Kühlbrandt, "Crystallisation, structure and function of plant light-harvesting complex II," *Biochimica et Biophysica Acta (BBA)-Bioenergetics*, vol. 1787, no. 6, pp. 753–772, 2009.

[31] J. F. Allen and J. Forsberg, "Molecular recognition in thylakoid structure and function," *Trends in Plant Science*, vol. 6, no. 7, pp. 317–326, 2001.

[32] D. Kyle, L. Staehelin, and C. Arntzen, "Lateral mobility of the light-harvesting complex in chloroplast membranes controls excitation energy distribution in higher plants," *Archives of Biochemistry and Biophysics*, vol. 222, no. 2, pp. 527–541, 1983.

[33] C. Büchel, "Fucoxanthin-chlorophyll-proteins and non-photochemical fluorescence quenching of diatoms," in *Non-Photochemical Quenching and Energy Dissipation in Plants, Algae and Cyanobacteria*, pp. 259–275, Springer, 2014.

[34] C. Wilhelm, C. Büchel, J. Fisahn, R. Goss, T. Jakob, J. LaRoche, J. Lavaud, M. Lohr, U. Riebesell, K. Stehfest, K. Valentin, and P. G. Kroth, "The regulation of carbon and

nutrient assimilation in diatoms is significantly different from green algae," *Protist*, vol. 157, no. 2, pp. 91 – 124, 2006.

[35] J. Joshi-Deo, M. Schmidt, A. Gruber, W. Weisheit, M. Mittag, P. G. Kroth, and C. Büchel, "Characterization of a trimeric light-harvesting complex in the diatom phaeodactylum tricornutum built of FcpA and FcpE proteins," *Journal of Experimental Botany*, vol. 61, no. 11, pp. 3079–3087, 2010.

[36] E. Papagiannakis, I. H. van Stokkum, H. Fey, C. Büchel, and R. van Grondelle, "Spectroscopic characterization of the excitation energy transfer in the fucoxanthin-chlorophyll protein of diatoms," *Photosynthesis Research*, vol. 86, no. 1, pp. 241–250, 2005.

[37] K. Gundermann and C. Büchel, "Structure and functional heterogeneity of fucoxanthin-chlorophyll proteins in diatoms," in *The Structural Basis of Biological Energy Generation*, pp. 21–37, Springer Netherlands, 2014.

[38] D. Zigmantas, R. G. Hiller, F. P. Sharples, H. A. Frank, V. Sundstrom, and T. Polivka, "Effect of a conjugated carbonyl group on the photophysical properties of carotenoids," *Phys. Chem. Chem. Phys.*, vol. 6, pp. 3009–3016, 2004.

[39] L. Premvardhan, L. Bordes, A. Beer, C. Büchel, and B. Robert, "Carotenoid structures and environments in trimeric and oligomeric fucoxanthin chlorophyll a/c2 proteins from resonance Raman spectroscopy," *The Journal of Physical Chemistry B*, vol. 113, no. 37, pp. 12565–12574, 2009.

[40] M. Wahadoszamen, A. Ghazaryan, H. E. Cingil, A. M. Ara, C. Büchel, R. van Grondelle, and R. Berera, "Stark fluorescence spectroscopy reveals two emitting sites in the dissipative state of FCP antennas," *Biochimica et Biophysica Acta (BBA)-Bioenergetics*, vol. 1837, no. 1, pp. 193–200, 2014.

[41] A. Röding, E. Boekema, and C. Büchel, "The structure of FCPb, a light-harvesting complex in the diatom cyclotella meneghiniana," *Photosynthesis Research*, pp. 1–9, 2016.

[42] R. Van Grondelle, "Excitation energy transfer, trapping and annihilation in photosynthetic systems," *Biochimica et biophysica acta*, vol. 811, no. 2, pp. 147–195, 1985.

[43] J. Lakowicz, *Topics in Fluorescence Spectroscopy: Principles*. Topics in Fluorescence Spectroscopy, Springer US, 2006.

[44] P. Wu and L. Brand, "Resonance energy transfer: methods and applications," *Analytical biochemistry*, vol. 218, no. 1, pp. 1–13, 1994.

[45] T. Renger, "Theory of excitation energy transfer: from structure to function," *Photosynthesis research*, vol. 102, no. 2-3, pp. 471–485, 2009.

[46] V. Sundström, "Light in elementary biological reactions," *Progress in Quantum Electronics*, vol. 24, no. 5, pp. 187–238, 2000.

[47] A. Ishizaki and G. R. Fleming, "On the adequacy of the redfield equation and related approaches to the study of quantum dynamics in electronic energy transfer," *The Journal of chemical physics*, vol. 130, no. 23, p. 234110, 2009.

[48] H. van Amerongen, L. Valkunas, and R. van Grondelle, *Photosynthetic Excitons*. World Scientific, 2000.

[49] J. Larsen, B. Brüggemann, T. Polivka, V. Sundström, E. Akesson, J. Sly, and M. J. Crossley, "Energy transfer within zn–porphyrin dendrimers, study of the singlet-singlet annihilation kinetics," *The Journal of Physical Chemistry A*, vol. 109, no. 47, pp. 10654–10662, 2005.

[50] H. Visser, F. Kleima, I. van Stokkum, R. van Grondelle, and H. van Amerongen, "Probing the many energy-transfer processes in the photosynthetic light-harvesting complex II at 77 K using energy-selective sub-picosecond transient absorption spectroscopy," *Chemical Physics*, vol. 210, no. 1, pp. 297 – 312, 1996.

[51] P. Müller, X.-P. Li, and K. K. Niyogi, "Non-photochemical quenching. A response to excess light energy," *Plant Physiology*, vol. 125, no. 4, pp. 1558–1566, 2001.

[52] P. Horton, A. V. Ruban, and R. G. Walters, "Regulation of light harvesting in green plants (indication by nonphotochemical quenching of chlorophyll fluorescence).," *Plant Physiology*, vol. 106, no. 2, p. 415, 1994.

[53] P. Horton, A. Ruban, D. Rees, A. Pascal, G. Noctor, and A. Young, "Control of the light-harvesting function of chloroplast membranes by aggregation of the LHCII chlorophyll-protein complex," *FEBS letters*, vol. 292, no. 1, pp. 1–4, 1991.

[54] I. Szabó, E. Bergantino, and G. M. Giacometti, "Light and oxygenic photosynthesis: energy dissipation as a protection mechanism against photo-oxidation," *EMBO reports*, vol. 6, no. 7, pp. 629–634, 2005.

[55] G. C. Papageorgiou and Govindjee, *The Non-Photochemical Quenching of the Electronically Excited State of Chlorophyll a in Plants: Definitions, Timelines, Viewpoints, Open Questions*, pp. 1–44. Dordrecht: Springer Netherlands, 2014.

[56] B. van Oort, A. van Hoek, A. V. Ruban, and H. van Amerongen, "Aggregation of light-harvesting complex II leads to formation of efficient excitation energy traps in monomeric and trimeric complexes," *FEBS Letters*, vol. 581, no. 18, pp. 3528 – 3532, 2007.

[57] M. G. Müller, P. Lambrev, M. Reus, E. Wientjes, R. Croce, and A. R. Holzwarth, "Singlet energy dissipation in the photosystem II light-harvesting complex does not involve energy transfer to carotenoids," *ChemPhysChem*, vol. 11, no. 6, pp. 1289–1296, 2010.

[58] I. Moya, M. Silvestri, O. Vallon, G. Cinque, and R. Bassi, "Time-resolved fluorescence analysis of the photosystem II antenna proteins in detergent micelles and liposomes," *Biochemistry*, vol. 40, no. 42, pp. 12552–12561, 2001. PMID: 11601979.

[59] Y. Miloslavina, A. Wehner, P. H. Lambrev, E. Wientjes, M. Reus, G. Garab, R. Croce, and A. R. Holzwarth, "Far-red fluorescence: A direct spectroscopic marker for LHCII oligomer formation in non-photochemical quenching," *FEBS letters*, vol. 582, no. 25-26, pp. 3625–3631, 2008.

[60] A. Ruban, D. Rees, G. Noctor, A. Young, and P. Horton, "Long-wavelength chlorophyll species are associated with amplification of high-energy-state excitation quenching in higher plants," *Biochimica et Biophysica Acta (BBA)-Bioenergetics*, vol. 1059, no. 3, pp. 355–360, 1991.

[61] T. P. Krüger, C. Ilioaia, M. P. Johnson, A. V. Ruban, and R. Van Grondelle, "Disentangling the low-energy states of the major light-harvesting complex of plants and their role in photoprotection," *Biochimica et Biophysica Acta (BBA)-Bioenergetics*, vol. 1837, no. 7, pp. 1027–1038, 2014.

[62] A. Ruban, D. Rees, A. Pascal, and P. Horton, "Mechanism of δ ph-dependent dissipation of absorbed excitation energy by photosynthetic membranes. ii. the relationship between lhcii aggregation in vitro and qe in isolated thylakoids," *Biochimica et Biophysica Acta (BBA) - Bioenergetics*, vol. 1102, no. 1, pp. 39 – 44, 1992.

[63] K. K. Niyogi, X.-P. Li, V. Rosenberg, and H.-S. Jung, "Is psbs the site of non-photochemical quenching in photosynthesis?," *Journal of Experimental Botany*, vol. 56, no. 411, pp. 375–382, 2004.

[64] K. Gundermann and C. Büchel, "Factors determining the fluorescence yield of fucoxanthin-chlorophyll complexes (FCP) involved in non-photochemical quenching in diatoms," *Biochimica et Biophysica Acta (BBA)-Bioenergetics*, vol. 1817, no. 7, pp. 1044–1052, 2012.

[65] V. I. Prokhorenko, A. M. Nagy, and R. J. D. Miller, "Coherent control of the population transfer in complex solvated molecules at weak excitation. an experimental study," *Chemical Physics*, vol. 122, no. 18, p. 184502, 2005.

[66] V. I. Prokhorenko, A. M. Nagy, S. A. Waschuk, L. S. Brown, R. R. Birge, and R. J. D. Miller, "Coherent control of retinal isomerization in bacteriorhodopsin," *Science*, vol. 313, no. 5791, p. 1257, 2006.

[67] J. L. Herek, W. Wohlleben, R. J, Cogdell, D. Zeidler, and M. Motzkus, "Quantum control of energy flow in light harvesting," *Nature*, vol. 417, p. 533, 2002.

[68] J. Savolainen, T. Buckup, J. Hauer, A. Jafarpour, C. Serrat, M. Motzkus, and J. L. Herek, "Carotenoid deactivation in an artificial light-harvesting complex via a vibrationally hot ground state," *Chemical Physics*, vol. 357, no. 1, pp. 181–187, 2009.

[69] V. I. Prokhorenko, A. Halpin, P. J. M. Johnson, R. J. D. Miller, and L. S. Brown, "Coherent control of the isomerization of retinal in bacteriorhodopsin in the high intensity regime," *Chemical Physics*, vol. 134, no. 8, p. 085105, 2011.

[70] Y. Miloslavina, I. Grouneva, P. H. Lambrev, B. Lepetit, R. Goss, C. Wilhelm, and A. R. Holzwarth, "Ultrafast fluorescence study on the location and mechanism of non-photochemical quenching in diatoms," *Biochimica et Biophysica Acta (BBA)-Bioenergetics*, vol. 1787, no. 10, pp. 1189–1197, 2009.

[71] B. Lepetit, R. Goss, T. Jakob, and C. Wilhelm, "Molecular dynamics of the diatom thylakoid membrane under different light conditions," *Photosynthesis research*, vol. 111, no. 1-2, pp. 245–257, 2012.

[72] V. U. Chukhutsina, C. Büchel, and H. van Amerongen, "Disentangling two non-photochemical quenching processes in cyclotella meneghiniana by spectrally-resolved picosecond fluorescence at 77K," *Biochimica et Biophysica Acta (BBA)-Bioenergetics*, vol. 1837, no. 6, pp. 899–907, 2014.

[73] T. P. Krüger, P. Malỳ, M. T. Alexandre, T. Mančal, C. Büchel, and R. van Grondelle, "How reduced excitonic coupling enhances light harvesting in the main photosynthetic antennae of diatoms," *Proceedings of the National Academy of Sciences*, p. 201714656, 2017.

[74] C. Ramanan, R. Berera, K. Gundermann, I. van Stokkum, C. Büchel, and R. van Grondelle, "Exploring the mechanism (s) of energy dissipation in the light harvesting complex of the photosynthetic algae cyclotella meneghiniana," *Biochimica et Biophysica Acta (BBA)-Bioenergetics*, vol. 1837, no. 9, pp. 1507 – 1513, 2014.

[75] C. Rulliere, *Femtosecond Laser Pulses: Principles and Experiments*. Advanced Texts in Physics, Springer, 2005.

[76] G. D. Reid and K. Wynne, "Ultrafast laser technology and spectroscopy," *Encyclopedia of Analytical chemistry*, 2000.

[77] J.-C. Diels and W. Rudolph, *Ultrashort laser pulse phenomena*. Academic press, 2006.

[78] M. Wollenhaupt, A. Assion, and T. Baumert, "Femtosecond laser pulses: Linear properties, manipulation, generation and measurement,"

[79] R. R. Alfano, *The Supercontinuum Laser Source: Fundamentals with Updated References*. Springer, 2nd ed., 2005.

[80] A. Brodeur and S. Chin, "Ultrafast white-light continuum generation and self-focusing in transparent condensed media," *JOSA B*, vol. 16, no. 4, pp. 637–650, 1999.

[81] S. Uhlig, *Self-Organized Surface Structures with Ultrafast White-Light: First Investigation of LIPSS with Supercontinuum*. BestMasters, Springer Spektrum, 1 ed., 2015.

[82] M. Bradler, P. Baum, and E. Riedle, "Femtosecond continuum generation in bulk laser host materials with sub-μJ pump pulses," *Applied Physics B*, vol. 97, no. 3, pp. 561–574, 2009.

[83] W. Demtröder, *Laser spectroscopy: basic concepts and instrumentation*. Springer Science & Business Media, 2013.

[84] G. New, *Introduction to nonlinear optics*. Cambridge University Press, 2011.

[85] W. M. Andrew, "Femtosecond pulse shaping using spatial light modulators," *Review of scientific instruments*, vol. 71, no. 5, pp. 1929–1960, 2000.

[86] W. M. Andrew, "Ultrafast optical pulse shaping A tutorial review," *Optics Communications*, vol. 284, no. 15, pp. 3669–3692, 2011.

[87] A. Monmayrant, S. Weber, and B. Chatel, "A newcomer's guide to ultrashort pulse shaping and characterization," *Journal of Physics B: Atomic, Molecular and Optical Physics*, vol. 43, no. 10, p. 103001, 2010.

[88] A. Präkelt, M. Wollenhaupt, A. Assion, C. Horn, C. Sarpe-Tudoran, M. Winter, and T. Baumert, "Compact robust and flexible setup for femtosecond pulse shaping," *Review of scientific instruments*, vol. 74, no. 11, pp. 4950–4953, 2003.

[89] T. Oksenhendler and N. Forget, *Pulse-shaping techniques theory and experimental implementations for femtosecond pulses*. INTECH Open Access Publisher, 2010.

[90] D. Goswami, "Optical pulse shaping approaches to coherent control," *Physics Reports*, vol. 374, no. 6, pp. 385 – 481, 2003.

[91] T. Brixner, A. Oehrlein, M. Strehle, and G. Gerber, "Feedback-controlled femtosecond pulse shaping," *Applied Physics B: Lasers and Optics*, vol. 70, no. 7, pp. S119–S124, 2000.

[92] R. Trebino, K. W. DeLong, D. N. Fittinghoff, J. N. Sweetser, M. A. Krumbügel, B. A. Richman, and D. J. Kane, "Measuring ultrashort laser pulses in the time-frequency domain using frequency-resolved optical gating," *Review of Scientific Instruments*, vol. 68, no. 9, pp. 3277–3295, 1997.

[93] I. Z. Kozma, P. Baum, U. Schmidhammer, S. Lochbrunner, and E. Riedle, "Compact autocorrelator for the online measurement of tunable 10 femtosecond pulses," *Review of Scientific instruments*, vol. 75, no. 7, pp. 2323–2327, 2004.

[94] G. Cerullo, C. Manzoni, L. Luer, and D. Polli, "Time-resolved methods in biophysics. 4. broadband pump-probe spectroscopy system with sub-20 fs temporal resolution for the study of energy transfer processes in photosynthesis," *Photochem. Photobiol. Sci.*, vol. 6, pp. 135–144, 2007.

[95] A. H. Zewail, "Femtochemistry: Atomic-scale dynamics of the chemical bond," *The Journal of Physical Chemistry A*, vol. 104, no. 24, pp. 5660–5694, 2000.

[96] U.Megerle, , I. Pugliesi, C. Schriever, C. F. Sailer, and E. Riedle, "Sub-50 fs broadband absorption spectroscopy with tunable excitation: putting the analysis of ultrafast molecular dynamics on solid ground," *Applied Physics B*, vol. 96, no. 2, pp. 215–231, 2009.

[97] R. Berera, R. van Grondelle, and J. T. Kennis, "Ultrafast transient absorption spectroscopy: principles and application to photosynthetic systems," *Photosynthesis research*, vol. 101, no. 2-3, pp. 105–118, 2009.

[98] M. L. Groot, L. J. van Wilderen, and M. Di Donato, "Time-resolved methods in biophysics. 5. femtosecond time-resolved and dispersed infrared spectroscopy on proteins," *Photochemical & Photobiological Sciences*, vol. 6, no. 5, pp. 501–507, 2007.

[99] T. Brixner, J. Stenger, H. M. Vaswani, M. Cho, R. E. Blankenship, and G. R. Fleming, "Two-dimensional spectroscopy of electronic couplings in photosynthesis," *Nature*, vol. 434, no. 7033, p. 625, 2005.

[100] D. J. Tannor, R. Kosloff, and S. A. Rice, "Coherent pulse sequence induced control of selectivity of reactions: Exact quantum mechanical calculations," *The Journal of Chemical Physics*, vol. 85, no. 10, pp. 5805–5820, 1986.

[101] B. Paul and P. W. Brumer, "Control of unimolecular reactions using coherent light," *Chemical physics letters*, vol. 126, no. 6, pp. 541 –546, 1986.

[102] R. S. Judson and H. Rabitz, "Teaching lasers to control molecules," *Physical Review Letters*, vol. 68, no. 10, p. 1500, 1992.

[103] A. Florean, E. Carroll, K. Spears, R. Sension, and P. Bucksbaum, "Optical control of excited-state vibrational coherences of a molecule in solution: The influence of the excitation pulse spectrum and phase in LD690," *The Journal of Physical Chemistry B*, vol. 110, no. 40, pp. 20023–20031, 2006.

[104] F. G. Prendergast, "Time-resolved fluorescence techniques: methods and applications in biology," *Current Opinion in Structural Biology*, vol. 1, no. 6, pp. 1054–1059, 1991.

[105] E. Roduner, P. B. C. Forbes, T. Krüger, and K. C. Kress, *Optical Spectroscopy: Fundamentals and Advanced Applications*. World Scientific, 1st ed., 2019.

[106] T. M. Nordlund, "Streak camera methods in nucleic acid and protein fluorescence spectroscopy," in *Time-Resolved Laser Spectroscopy in Biochemistry*, vol. 909, pp. 35–51, International Society for Optics and Photonics, 1988.

[107] S. Ombinda-Lemboumba, A. D. Plessis, R. W. Sparrow, P. Molukanele, L. R. Botha, E. G. Rohwer, C. M. Steenkamp, and L. V. Rensburg, "Femtosecond pump probe spectroscopy for the study of energy transfer of light-harvesting complexes from extractions of spinach leaves," *South African Journal of Science*, vol. 105, no. 9-10, pp. 376–386, 2009.

[108] I. Pastirk, E. J. Brown, Q. Zhang, and M. Dantus, "Quantum control of the yield of a chemical reaction," *The Journal of chemical physics*, vol. 108, no. 11, pp. 4375–4378, 1998.

[109] M. Dantus and V. V. Lozovoy, "Experimental coherent laser control of physicochemical processes," *Chemical reviews*, vol. 104, no. 4, pp. 1813–1860, 2004.

[110] T. Brixner and G. Gerber, "Quantum control of gas-phase and liquid-phase femtochemistry," *ChemPhysChem*, vol. 4, no. 5, p. 418, 2003.

[111] M. Shapiro and P. Brumer, *Quantum Control of Molecular Processes*. John Wiley and Sons, 2012.

[112] S. M. Park, S.-P. Lu, and R. J. Gordon, "Coherent laser control of the resonance-enhanced multiphoton ionization of HCl," *The Journal of chemical physics*, vol. 94, no. 12, pp. 8622–8624, 1991.

[113] T. Baumert, M. Grosser, R. Thalweiser, and G. Gerber, "Femtosecond time-resolved molecular multiphoton ionization: The Na 2 system," *Physical review letters*, vol. 67, no. 27, p. 3753, 1991.

[114] K. Bergmann, H. Theuer, and B. Shore, "Coherent population transfer among quantum states of atoms and molecules," *Reviews of Modern Physics*, vol. 70, no. 3, p. 1003, 1998.

[115] H. Rabitz, R. de Vivie-Riedle, M. Motzkus, and K. Kompa, "Whither the future of controlling quantum phenomena?," *Science*, vol. 288, no. 5467, pp. 824–828, 2000.

[116] J. Savolainen, R. Fanciulli, N. Dijkhuizen, A. L. Moore, J. Hauer, T. Buckup, M. Motzkus, , and J. L. Herek, "Controlling the efficiency of an artificial light-harvesting complex," *PNAS*, vol. 105, no. 22, p. 7641, 2008.

[117] C. J. Bardeen, V. V. Yakovlev, J. A. Squier, and K. R. Wilson, "Quantum control of population transfer in green fluorescent protein by using chirped femtosecond pulses," *Journal of the American Chemical Society*, vol. 120, no. 50, pp. 13023–13027, 1998.

[118] Clark-MXR and Inc, *System Components, CPA-Series User Manual, Version 2.4*, 2008.

[119] E. Riedle, *NOPA Fundamentals and Instructions Manual*, 2005.

[120] S. V. Kurbasov, *Femtosecond Pump-Probe System, ExciPro User Manual, Version 2.4.3*, 2000-2007.

[121] I. H. van Stokkum, D. S. Larsen, and R. van Grondelle, "Global and target analysis of time-resolved spectra," *Biochimica et Biophysica Acta (BBA) - Bioenergetics*, vol. 1657, no. 2âĂŞ3, pp. 82 – 104, 2004.

[122] J. Snellenburg, S. Laptenok, R. Seger, K. Mullen, and I. V. Stokkum, "Glotaran: a java-based graphical user interface for the R package TIMP," *Journal of Statistical Software*, vol. 49, no. 3, 2012.

[123] A. J. Hendriks, *Control of CO_2 Vibrational Dynamics via Shaped-Pulse Coherent Anti-Stokes Raman Spectroscopy*. Phd, 2017.

[124] JENOPTIK, *SLM-S640 USB Technical Documentation*, 2015.

[125] D. E. Goldberg, *Genetic Algorithms in Search, Optimization and Machine Learning*. Boston, MA, USA: Addison-Wesley Longman Publishing Co., Inc., 1st ed., 1989.

[126] K.-S. Tang, K.-F. Man, S. Kwong, and Q. He, "Genetic algorithms and their applications," *IEEE signal processing magazine*, vol. 13, no. 6, pp. 22–37, 1996.

[127] M. Mitchell, *An introduction to genetic algorithms*. MIT press, 1998.

[128] S. Forrest, "Genetic algorithms: principles of natural selection applied to computation," *Science*, vol. 261, no. 5123, pp. 872–878, 1993.

[129] F. Dimler, S. Fechner, A. Rodenberg, T. Brixner, and D. J. Tannor, "Accurate and efficient implementation of the von neumann representation for laser pulses with discrete and finite spectra," *New Journal of Physics*, vol. 11, no. 10, p. 105052, 2009.

[130] K.-H. Hong, J.-H. Kim, Y. H. Kang, and C. H. Nam, "Time-frequency analysis of chirped femtosecond pulses using wigner distribution function," *Applied Physics B*, vol. 74, no. 1, pp. s231–s236, 2002.

[131] S. Fechner, F. Dimler, T. Brixner, G. Gerber, and D. J. Tannor, "The von neumann picture: a new representation for ultrashort laser pulses," *Optics express*, vol. 15, no. 23, pp. 15387–15401, 2007.

[132] J. P. Connelly, M. G. Müller, R. Bassi, R. Croce, and A. R. Holzwarth, "Femtosecond transient absorption study of carotenoid to chlorophyll energy transfer in the light-harvesting complex II of photosystem II," *Biochemistry*, vol. 36, no. 2, pp. 281–287, 1997.

[133] M. Mimuro, "Visualization of excitation energy transfer processes in plants and algae," *Photosynthesis research*, vol. 73, no. 1-3, pp. 133–138, 2002.

[134] D. Kuciauskas, P. A. Liddell, S. Lin, T. E. Johnson, S. J. Weghorn, J. S. Lindsey, A. L. Moore, T. A. Moore, and D. Gust, "An artificial photosynthetic antenna-reaction center complex," *Journal of the American Chemical Society*, vol. 121, no. 37, pp. 8604–8614, 1999.

[135] D. Gust, T. A. Moore, and A. L. Moore, "Molecular mimicry of photosynthetic energy and electron transfer," *Accounts of Chemical Research*, vol. 26, no. 4, pp. 198–205, 1993.

[136] D. Gust, T. A. Moore, and A. L. Moore, "Mimicking photosynthetic solar energy transduction," *Accounts of Chemical Research*, vol. 34, no. 1, pp. 40–48, 2001.

[137] Y. Koyama, M. Kuki, P. O. Andersson, and T. Gillbro, "Singlet excited states and the light-harvesting function of carotenoids in bacterial photosynthesis," *Photochemistry and photobiology*, vol. 63, no. 3, pp. 243 –256, 1996.

[138] K. Petrou, E. Belgio, and A. V. Ruban, "ph sensitivity of chlorophyll fluorescence quenching is determined by the detergent/protein ratio and the state of LHCII aggregation," *Biochimica et Biophysica Acta (BBA)-Bioenergetics*, vol. 1837, no. 9, pp. 1533–1539, 2014.

[139] E. J. Peterman, R. Monshouwer, I. H. van Stokkum, R. van Grondelle, and H. van Amerongen, "Ultrafast singlet excitation transfer from carotenoids to chlorophylls via different pathways in light-harvesting complex II of higher plants," *Chemical physics letters*, vol. 264, no. 3, pp. 279–284, 1997.

[140] W. Wohlleben, T. Buckup, J. L. Herek, and M. Motzkus, "Coherent control for spectroscopy and manipulation of biological dynamics," *ChemPhysChem*, vol. 6, no. 5, pp. 850–857, 2005.

[141] D. G. Kuroda, C. P. Singh, Z. Peng, and V. D. Kleiman, "Mapping excited-state dynamics by coherent control of a dendrimer's photoemission efficiency," *Science*, vol. 326, no. 5950, p. 263, 2009.

[142] J. Hauer, H. Skenderovic, K.-L. Kompa, and M. Motzkus, "Enhancement of raman modes by coherent control in β-carotene," *Chemical Physics Letters*, vol. 421, no. 4-6, pp. 523–528, 2006.

[143] J. Hauer, T. Buckup, and M. Motzkus, "Enhancement of molecular modes by electronically resonant multipulse excitation: Further progress towards mode selective chemistry," 2006.

[144] E. Papagiannakis, M. Vengris, L. Valkunas, R. J. Cogdell, R. van Grondelle, and D. S. Larsen, "Excited-state dynamics of carotenoids in light-harvesting complexes. 2. dissecting pulse structures from optimal control experiments," *The Journal of Physical Chemistry B*, vol. 110, no. 11, pp. 5737–5746, 2006.

[145] G. Cerullo, G. Lanzani, M. Zavelani-Rossi, and S. De Silvestri, "Early events of energy relaxation in all-trans-β-carotene following sub-10 fs optical-pulse excitation," *Physical Review B*, vol. 63, no. 24, p. 241104, 2001.

[146] A. M. Weiner, D. Leaird, G. P. Wiederrecht, and K. A. Nelson, "Femtosecond multiple-pulse impulsive stimulated raman scattering spectroscopy," *JOSA B*, vol. 8, no. 6, pp. 1264–1275, 1991.

[147] R. A. Bartels, S. Backus, M. M. Murnane, and H. Kapteyn, "Impulsive stimulated raman scattering of molecular vibrations using nonlinear pulse shaping," *Chemical Physics Letters*, vol. 374, no. 3–4, pp. 326–333, 2003.

[148] A. Weiner, D. Leaird, G. P. Wiederrecht, and K. A. Nelson, "Femtosecond pulse sequences used for optical manipulation of molecular motion," *Science*, vol. 247, no. 4948, pp. 1317–1319, 1990.

[149] D. Rutkauskas, J. Chmeliov, M. Johnson, A. Ruban, and L. Valkunas, "Exciton annihilation as a probe of the light-harvesting antenna transition into the photoprotective mode," *Chemical Physics*, vol. 404, pp. 123–128, 2012.

[150] V. Barzda, V. Gulbinas, R. Kananavicius, V. Cervinskas, H. Van Amerongen, R. Van Grondelle, and L. Valkunas, "Singlet-singlet annihilation kinetics in aggregates and trimers of LHCII," *Biophysical journal*, vol. 80, no. 5, pp. 2409–2421, 2001.

[151] L. Premvardhan, B. Robert, A. Beer, and C. Büchel, "Pigment organization in fucoxanthin chlorophyll a/c 2 proteins (FCP) based on resonance raman spectroscopy and sequence analysis," *Biochimica et Biophysica Acta (BBA)-Bioenergetics*, vol. 1797, no. 9, pp. 1647–1656, 2010.

[152] B. Bailleul, A. Rogato, A. De Martino, S. Coesel, P. Cardol, C. Bowler, A. Falciatore, and G. Finazzi, "An atypical member of the light-harvesting complex stress-related protein family modulates diatom responses to light," *Proceedings of the National Academy of Sciences*, vol. 107, no. 42, pp. 18214–18219, 2010.

[153] J. Lavaud, B. Rousseau, H. J. Van Gorkom, and A.-L. Etienne, "Influence of the diadinoxanthin pool size on photoprotection in the marine planktonic diatom phaeodactylum tricornutum," *Plant Physiology*, vol. 129, no. 3, pp. 1398–1406, 2002.

[154] M. Olaizola, J. La Roche, Z. Kolber, and P. G. Falkowski, "Non-photochemical fluorescence quenching and the diadinoxanthin cycle in a marine diatom," *Photosynthesis Research*, vol. 41, no. 2, pp. 357–370, 1994.

[155] K. Gundermann and C. Büchel, "The fluorescence yield of the trimeric fucoxanthin-chlorophyll-protein FCPa in the diatom cyclotella meneghiniana is dependent on the amount of bound diatoxanthin," *Photosynthesis Research*, vol. 95, no. 2-3, pp. 229–235, 2008.

[156] P. Horton, M. Wentworth, and A. Ruban, "Control of the light harvesting function of chloroplast membranes: The LHCII-aggregation model for non-photochemical quenching," *Febs Letters*, vol. 579, no. 20, pp. 4201–4206, 2005.

[157] A. V. Ruban, R. Berera, C. Ilioaia, I. H. Van Stokkum, J. T. Kennis, A. A. Pascal, H. Van Amerongen, B. Robert, P. Horton, and R. Van Grondelle, "Identification of a mechanism of photoprotective energy dissipation in higher plants," *Nature*, vol. 450, no. 7169, pp. 575–578, 2007.

[158] N. Gildenhoff, S. Amarie, K. Gundermann, A. Beer, C. Büchel, and J. Wachtveitl, "Oligomerization and pigmentation dependent excitation energy transfer in fucoxanthin-

chlorophyll proteins," *Biochimica et Biophysica Acta (BBA)-Bioenergetics*, vol. 1797, no. 5, pp. 543–549, 2010.

[159] G. Öquist and N. P. Huner, "Photosynthesis of overwintering evergreen plants," *Annual Review of Plant Biology*, vol. 54, no. 1, pp. 329–355, 2003.

[160] Y. Tang, X. Wen, Q. Lu, Z. Yang, Z. Cheng, and C. Lu, "Heat stress induces an aggregation of the light-harvesting complex of photosystem II in spinach plants," *Plant physiology*, vol. 143, no. 2, pp. 629–638, 2007.

[161] I. Grouneva, T. Jakob, C. Wilhelm, and R. Goss, "Influence of ascorbate and ph on the activity of the diatom xanthophyll cycle-enzyme diadinoxanthin de-epoxidase," *Physiologia Plantarum*, vol. 126, no. 2, pp. 205–211, 2006.

[162] A. Natali, J. M. Gruber, L. Dietzel, M. C. Stuart, R. van Grondelle, and R. Croce, "Light-harvesting complexes (LHCs) cluster spontaneously in membrane environment leading to shortening of their excited state lifetimes," *Journal of Biological Chemistry*, vol. 291, no. 32, pp. 16730–16739, 2016.

[163] L. Provasoli, J. McLaughlin, and M. Droop, "The development of artificial media for marine algae," *Archiv für Mikrobiologie*, vol. 25, no. 4, pp. 392–428, 1957.

[164] B. Van Oort, A. Amunts, J. W. Borst, A. Van Hoek, N. Nelson, H. Van Amerongen, and R. Croce, "Picosecond fluorescence of intact and dissolved PSI-LHCI crystals," *Biophysical journal*, vol. 95, no. 12, pp. 5851–5861, 2008.

[165] C. C. Gradinaru, R. Van Grondelle, and H. Van Amerongen, "Selective interaction between xanthophylls and chlorophylls in LHCII probed by femtosecond transient absorption spectroscopy," *The Journal of Physical Chemistry B*, vol. 107, no. 16, pp. 3938–3943, 2003.

[166] R. Croce, A. Chojnicka, T. Morosinotto, J. A. Ihalainen, F. Van Mourik, J. P. Dekker, R. Bassi, and R. Van Grondelle, "The low-energy forms of photosystem I light-harvesting complexes: spectroscopic properties and pigment-pigment interaction characteristics," *Biophysical journal*, vol. 93, no. 7, pp. 2418–2428, 2007.

[167] E. Romero, M. Mozzo, I. H. Van Stokkum, J. P. Dekker, R. Van Grondelle, and R. Croce, "The origin of the low-energy form of photosystem I light-harvesting complex Lhca4: mixing of the lowest exciton with a charge-transfer state," *Biophysical journal*, vol. 96, no. 5, pp. L35–L37, 2009.

[168] T. P. Krüger, V. I. Novoderezhkin, C. Ilioaia, and R. Van Grondelle, "Fluorescence spectral dynamics of single LHCII trimers," *Biophysical journal*, vol. 98, no. 12, pp. 3093–3101, 2010.

[169] T. P. Krüger, E. Wientjes, R. Croce, and R. van Grondelle, "Conformational switching explains the intrinsic multifunctionality of plant light-harvesting complexes," *Proceedings of the National Academy of Sciences*, vol. 108, no. 33, pp. 13516–13521, 2011.

[170] M. Di Valentin, C. Büchel, G. M. Giacometti, and D. Carbonera, "Chlorophyll triplet quenching by fucoxanthin in the fucoxanthin-chlorophyll protein from the diatom cyclotella meneghiniana," *Biochemical and biophysical research communications*, vol. 427, no. 3, pp. 637–641, 2012.

[171] H. Schägger and G. Von Jagow, "Tricine-sodium dodecyl sulfate-polyacrylamide gel electrophoresis for the separation of proteins in the range from 1 to 100 kda," *Analytical Biochemistry*, vol. 166, no. 2, pp. 368–379, 1987.

[172] M. Chevallet, S. Luche, and T. Rabilloud, "Silver staining of proteins in polyacrylamide gels," *Nature protocols*, vol. 1, no. 4, p. 1852, 2006.